Damage Studies of Tungsten Samples Using Dense Plasma Focus Devices

A Thesis Submitted to the
College of Graduate and Postdoctoral Studies
In Partial Fulfillment of the Requirements
For the Degree of Master of Science
In the Department of Physics and Engineering Physics

University of Saskatchewan
Saskatoon

By

PRIYA SHARMA

Permission to Use

In presenting this thesis in partial fulfillment of the requirements for a Postgraduate degree from the University of Saskatchewan, I agree that the Libraries of this University may make it freely available for inspection. I further agree that permission for copying of this thesis in any manner, in whole or in part, for scholarly purposes may be granted by the professor or professors who supervised my thesis work or, in their absence, by the Head of the Department or the Dean of the College in which my thesis work was done. It is understood that any copying or publication or use of this thesis or parts thereof for financial gain shall not be allowed without my written permission. It is also understood that due recognition shall be given to me and to the University of Saskatchewan in any scholarly use which may be made of any material in my thesis.

Disclaimer

Reference in this thesis to any specific commercial products, process, or service by trade name, trademark, manufacturer, or otherwise, does not constitute or imply its endorsement, recommendation, or favoring by the University of Saskatchewan. The views and opinions of the author expressed herein do not state or reflect those of the University of Saskatchewan and shall not be used for advertising or product endorsement purposes.

Requests for permission to copy or to make other uses of materials in this thesis in whole or part should be addressed to:

Department Head

Physics and Engineering Physics Department

University of Saskatchewan

116 Science Place

Saskatoon, Saskatchewan S7N 5E2

Canada

or

Dean College of Graduate and Postdoctoral Studies

University of Saskatchewan

110 Science Place

Saskatoon, Saskatchewan S7N 5C9

Canada

Abstract

Design and studies of plasma facing material for a fusion reactor is an engineering challenge. The focus of this M.Sc. thesis research project studies the interaction between the helium (He) ion beam produced in a dense plasma focus (DPF) device and the tungsten samples (poly-W and nano-W). Re-commissioning and optimization of a 1 kJ Mather-type UofS-I DPF was completed at the University of Saskatchewan. The United Nations University/ International Centre for Theoretical (UNU/ICPT) DPF device operated with helium working gas at the Nanyang Technological University (NTU), Singapore was used to study damage effects of tungsten sample with pulsed plasma irradiation under a simulated damage condition similar to that in a fusion reactor. Effect of irradiation of 2.3×10^{28} m^{-2} s^{-1} helium ion flux on the PLANSEE double forged tungsten samples of size $1 \times 10 \times 10$ mm^3 was investigated. Poly-W samples were irradiated for 5, 10, 15 and 20 shots from a distance 7 cm from the central anode of the DPF device. Surface defects due to He exposure were studied with SEM micrograph. High heat loads resulted in blisters and micro-cracks on the sample surface. With increase in the number of shots the density of the blisters increased and the crater-like He bubbles on the W surface were observed. Re-solidification of the melted and sputtered surface have been noticed as well. Nano-structuration of W was realized with UNU/ICPT DPF in argon working gas at 50 Pa pressure. Successive plasma pulses increased size of nanoparticles and led to particle agglomeration. At 10 shots, uniformly distributed highly dense nanoparticles of the size 20-50 nm have been synthesized. Nanostructured samples were then exposed to He plasma under the same conditions used for the poly-W samples. Instead of blisters and holes, micro-cracks and nanopores have been found on the synthesized Nano-W. BSE imaging of the poly-W and nano-W gives an evidence of trapped He bubbles on the poly-W sample surface and He desorption around grain boundaries in nano-W samples. EDX spectra showed the presence of Cu impurities due to sputtering from the anode in the DPF device. The XRD analysis of the exposed sample shows peak shifting toward higher diffraction angles and peak broadening of the prominent peak in the poly-W as well as nano-W samples. The comparative studies between poly-W and nano-W samples under irradiation of He ions seem to support the previous suggestions that nano-W is more favorable to be used as an alternative for plasma facing materials.

Acknowledgments

First and foremost, I would like to acknowledge my profound and sincere thanks to my supervisor Dr. Chijin Xiao of Plasma Physics Laboratory (PPL) at the University of Saskatchewan, Canada. His unconditional support and enlightenment motivated me to pursue my post-graduate studies.

I would like to acknowledge the Natural Sciences and Engineering Research Council of Canada (NSERC), SK Innovation & Opportunity Scholarship and the University of Saskatchewan for financial support during my M.Sc. studies.

I would also like to thank MITACS for accepting my project proposal and supporting my project with the MITACS Globalink Award. My heartfelt thanks to Prof. Rajdeep Singh Rawat for being my Host-Supervisor during this project. His door has always been open for academic as well as virtuous support.

I am thankful to the National Institute of Education (NIE) - Nanyang Technical University (NTU) for hosting my project and providing me lab facilities. Within the NTU, I would like to thank NIE and NTU staff for support. I am grateful to Mr. Mayank Mishra for training me and giving me technical support. I am very thankful to Dr. Joseph Vas and Dr. Rohit Mandewal for outstanding guidance, valuable advice and expert comments. I would like to extend my thanks to Prof. Paul Lee, Mrs. Cecelia Selvam and Mr. Avinash Chaursiya, for helping me during the whole project.

I wish like to thank Dr. Michael P. Bradley for his enthusiastic guidance and constant motivation during my M.Sc studies. I would like to convey my heartfelt gratitude for Dr. Amir Farahani's help through discussions. I would also like to acknowledge my committee members, Dr. Kathryn McWilliams, Dr. Lenaic Couedel and Dr. Yansun Yao for giving constructive comments on my thesis and motivating me to extend my research productively.

I am very thankful to every other member of the Department of Physics Engineering Physics for such a friendly environment. Especially, I would like to thank Debbie, Marj, and Cindy Jelinski for giving the department a supportive and energetic atmosphere.

I would also like to thank Dr. Reza Alibazi Behbahani and Mr. Seanne Chung for sharing their valuable advice. My colleagues Igor Voldiner, Heba Bsharat, Ayub Khodaee, Tahreem

Yousaf, Nathan Nelson and Wlliam Elcock for fun and meaningful discussion. I am indebted to Lovepreet, Ramesh, Biswa, Arpana and Raam for their friendship and being there for my moral support.

Last but not least, I must express my heartiest gratitude to my parents and my brothers and sisters for constant encouragement and undying support throughout my whole studies. They always motivate me not to give up and provide me the strength to keep myself physically and mentally stable. Thank you.

Dedicated to my family

Table of Contents

List of Figures

List of Tables

List of Abbreviations

JET	Joint European Torus
ITER	International Thermonuclear Experimental Reactor
PFC	Plasma-Facing Components
PWI	Plasma-Wall Interaction
WEST	Tungsten Environment in Steady State Tokamak
RT	Room Temperature
PFM	Plasma-facing Components
UNU/ICPT PFF	United Nations University/ International Centre for Theoretical Physics Plasma Focus Facility
FESEM	Field-Emission Scanning Electron Microscope
BSED	Back-Scattering Emission Detector
EDX	Energy Dispersive X-Ray
XRD	X-Ray Diffraction
IO	ITER Organization
JAEA	Japan Atomic Energy Agency
D-T	Deuterium-Tritium
TFTR	Tokamak Fusion Test Reactor
ELM	Edge-Localized Mode
OTW	Operating Temperature Window
BCC	Body-Centred Cubic
FCC	Face-Centred Cubic
DBTT	Ductile-to-Brittle Transition Temperature
SPD	Severe Plastic Deformation
TDS	Thermal Desorption Spectrometry

TFGR W	Toughened, Fine-Grained, Recrystallized Tungsten
CG	Coarse-Grained
SG	Single Grained
NG	Nano-Grained
TEM	Transmission Electron Microscope
HED	High-Energy-Density
AISI	American Iron and Steel Institute
XPS	X-ray Photoelectron Spectroscopy
IFMIF	International Fusion Materials Irradiation Facility
DMP	Dense Magnetized Plasma
MHD	Magnetohydrodynamic
HX	Hard X-rays
EMP	Electromagnetic pulse
SCR	Silicon Controlled Rectifier
SED	Scanning Electron Detector
T.O.F.	Time-of-Flight
Poly-W	Polycrystalline Tungsten
Nano-W	Nanocrystalline Tungsten
GB	Grain Boundary
BCC	Body-Centered Crystal
FWHM	Full Width Half Maximum

Chapter 1

INTRODUCTION

1.1 Background Information and Research Objectives

Industrialization and global population growth in the developing nations are expected to increase energy demands by 48% in next 20 years [1]. Conventional sources of energy, such as coal, gas, and oil, cannot meet the constantly increasing energy demand. Moreover, they are not only contributing to global warming, but also playing a key element in environmental calamities ranging from water pollution and air contamination to the entire biome. To meet the demand for regular energy supply, we need invariant and foreseeable energy sources. Nuclear fusion is a scientifically proven, potentially reliable and sustainable energy source which provides a partial solution to lower the usage of fossil fuels. Unlike nuclear fission, nuclear fusion does not directly generate long-term radioactive waste and has a virtually unlimited fuel supply. In the Sun, the strong gravitational force creates a suitable condition for fusion. On the Earth, destructive H-bomb is based on fusion reactions. To utilize fusion for peaceful energy production, controlled thermonuclear fusion reactors will be needed, based on magnetic confinement or inertial confinement. For magnetic confinement, strong magnetic field is used to confine the fuel in the hot plasma state. The magnetic device designed with toroidal and poloidal magnetic field coils makes the charged particles to gyrate around magnetic field lines. Plasma is heated up through ohmic heating, with additional radio-frequency and neutral beam power injection. The tokamak is the most plausible magnetic configuration of the future nuclear fusion reactor. The Joint European Torus (JET) is a large nuclear fusion research reactor designed to study plasma behaviour and the required fusion conditions. Currently, JET is the largest tokamak, which has presented a successful working of a significant nuclear fusion energy output with a mixture of deuterium and tritium fuel for a short period of time [2]. The functioning of the D-T fusion is based on the fusion reaction producing an alpha particle (Helium) and neutron and at the same time releasing a large amount of energy.

Under robust research collaboration of seven countries, the International Thermonuclear Experimental Reactor (ITER), with its plasma volume ten times larger than that of JET, will realize scientific demonstration of a full-scale fusion power plant for electricity production. However, engineering design and technology challenges must be overwhelmed to present a viable reactor design through the next generation tokamaks commonly referred as Demos.

Efforts to solve the challenges of magnetic-confinement will be sterile if the plasma-facing components (PFC) cannot withstand flux conditions and the extreme temperature of the plasma. Plasma-wall interaction (PWI) results in the modification of the structure and morphology of the wall material facing the plasma. This motivated the research groups to understand the design of PFCs which tolerate the extreme conditions in the reactor. It is challenging to select and produce material that can be optimized as perfect Plasma Facing Material (PFM) at once. After optimization, PFM might deliver the various properties, as shown in Fig.1.1, required for ideal PFCs.

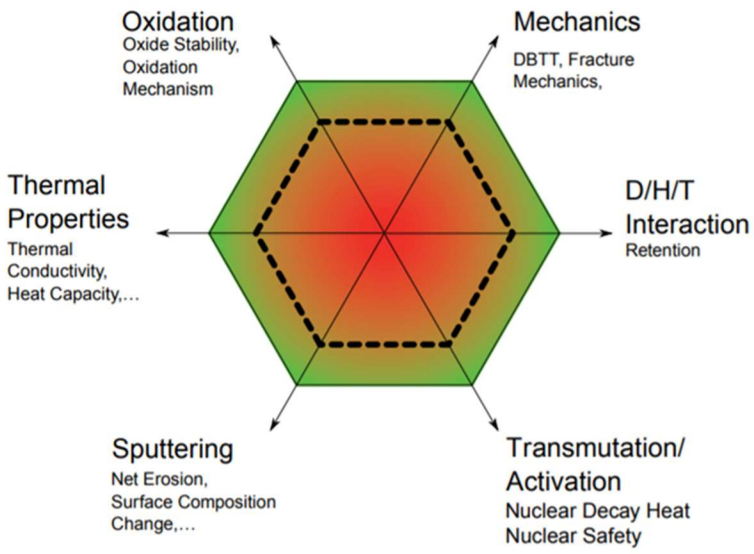

Figure 1.1: An optimized plasma facing material that fulfills all the required criteria with the interaction of other individual property. [3]

Tungsten is a favorable candidate for plasma-facing components. WEST (Tungsten Environment in Steady State Tokamak) is designed to use the ITER-like tungsten monoblocks actively cooled for long pulse operation [4]. The advantages of tungsten as plasma-facing components include low sputtering yield, high-temperature tolerance limit and low tritium retention. Apart from these promising features, the challenges arise due to its poor machinability, high brittleness to unfavorable ductile transition temperature, low fracture toughness, and catastrophic oxidation at high temperatures. The properties of tungsten as plasma-facing components are illustrated in Fig.1.2.

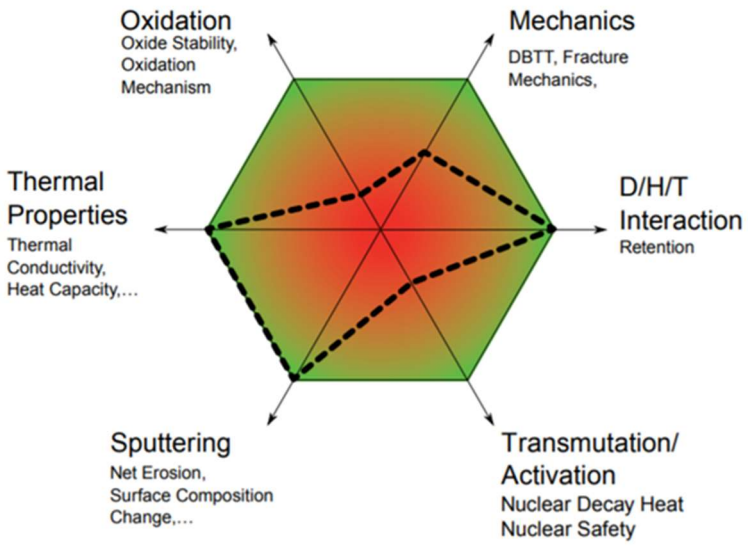

.

Figure 1.2: Tungsten properties (dashed line) as a plasma-facing material relative to the desired criteria.[3]

For a commercially viable reactor, the first-wall components must possess at least five full-power year lifetime [5]. Helium ions and neutron irradiation have the potential to limit the lifetime of the plasma-facing armour. In order to design suitable PFCs, a basic understanding of damage

mechanism and property evolution is required. The research projects for this thesis studies the defects evolved on the tungsten sample surface due to irradiation of helium ions from a dense plasma focus device. Since nano-W has been proposed as a promising candidate for PFCs, nano-W was synthesized and then irradiated by helium ions afterwards.

In order to achieve the research objective, the following tasks have be completed:

a) Studying the design and the working principle of United Nations University/ International Centre for Theoretical Physics Plasma Focus Facility (UNU/ICPT PFF) DPF at Nanyang Technological University, Singapore and UofS-I DPF at University of Saskatchewan, Canada.
b) Using Rogowski coil, voltage probe and Faraday cup to measure the heat flux and damage factor of the device.
c) investigating the effect of number of focus shots on the nano-structuration of the tungsten substrate in UNU/ICPT DPF with argon as a working gas.
d) Comparative study of Helium ion defects on the surface and subsurface region of the irradiated poly-W and nano-W samples with the help of Field Emission Scanning Electron Microscopy (FESEM), Energy Dispersive X-Ray Spectroscopy (EDX), Back-Scattering Electron Detector (BSED) , X-Ray Diffraction (XRD) and nano-indentation tests.

1.2 Thesis Outline

This chapter briefly introduces to thermonuclear nuclear fusion reactors and the need to study the plasma-facing materials. The remainder of the thesis is arranged in the following chapters:

Chapter 2 **(Background)** begins with the background physics for nuclear fusion reactors, plasma-facing components and the challenges faced while choosing plasma-facing materials. The motivation behind the selection of Nano-tungsten as PFM will also be specifically discussed.

Chapter 3 **(Dense Plasma Focus Device)** is devoted to describe the principles of the Z-pinch operation, the theory of the dynamics of focus discharge in a Dense Plasma Focus (DPF)

device, and the structure of the UofS-I DPF. The final part of this chapter summarizes the recent work devoted to the study of interaction between the plasma and PFMs using DPF devices.

Chapter 4 **(Diagnostic Techniques)** discusses the techniques specifically used for characterizing the plasma dynamics (Rogowski coil, voltage probe and Faraday cup) and to characterize various sample properties (FESEM, BSE, and EDX for Morphology, XRD for Crystallography and nano-indentation for hardness).

Chapter 5 **(Results and Discussion)** presents the correlaton between the effects of the helium ion irradiation on the poly-W and nano-W samples with the numbers of DPF shots. FESEM, BSE and EDX techniques were used to reveal the damage on the irradiated samples. of the crystallographic defects were studied based on XRD analysis. The chapter ends with the hardness analysis on the irradiated samples based on the nano-indentation method.

Chapter 6 **(Summary)** concludes the thesis. This chapter compiles the most critical insights from Chapter 5 and exhibits the significance of the nano-W as the plasma-facing material.

Chapter 2

PLASMA AND PLASMA-WALL INTERACTION

The main goal of this research project is to simulate the plasma-wall interaction in controlled thermonuclear fusion reactors using dense plasma focus plasma and tungsten samples under the controlled conditions. The total irradiation dose is controlled by number of irradiation exposures of the sample to the DPF discharges. This Chapter introduces basic plasma properties and parameters, its application for fusion energy. The main interactions between the plasma and chamber wall, relevant to the main research topics for the research project, will also be discussed.

2.1 Plasma

In the last 60 decades, plasma physics had emerged as one of the most demanding and forefront topics of the modem research. The plasma research includes understanding of the fundamental plasmas physics the related physical phenomena, and its applications. The scientific research results from different laboratories over the globe established not only a solid framework for this new branch of science, but also set a road for researchers to understand more up-to-date issues and to expand its horizon. The key to this fortunate episode depends on the unique blending of scientific contemplations and technological skills. As a result of such endeavors from scientists and engineers, the world has observed a worldwide transformation in high-tech industries. Plenty of technology advancements stemmed from the fast progress of plasma science and innovations.

Plasma is an ionized gas and its existence as the fourth state of matter was first recognized by Sir William Crookes in 1879 [6]. Later, the word “PLASMA” was first used to ionized gases in 1929 by an American chemist and physicist Dr. Irving Langmuir who had his accomplishment extended from surface chemistry to clouds [7]. Plasma in the space and in the stars around them comprises over 99.9% of the observable universe.

In solids, atoms are held in a defined regular pattern and in liquid state atoms are subjected to intermolecular attraction with definite volume and can occupy the compartment shape

effectively. While in gaseous state, atoms do not have definite shape and volume. On heating the gas, molecules gain thermal kinetic energy. Once the kinetic energy of the molecules becomes high enough, it breaks down the molecular bonds and dissociate the molecular gas into atomic gas. When the supplied thermal energy to the gas is higher than the ionization energy, atoms are ionized. This ionized gas composed of ions and free electrons is known as plasma provided it must satisfy some conditions discussed below.

Plasma is described as a quasi-neutral gas containing interacting free electrons, ionized species and macroscopically neutral substances showing collective behaviour. 'Collective behavior' defines the motions that not only rely on local conditions but on the plasma condition in far regions as well. **Quasi-neutrality** is a Latin word which means "as if". By the quasi-neutrality of the plasma we mean the overall charge neutrality of plasma, while at small scale, charged particles may give rise to some instant electric fields. Plasmas can be classified in terms of their electron density n_e and electron temperature T_e. The solar corona, Van Allen radiation belts, ionosphere, aurora, the comet tails are some examples of naturally occurring plasma. In outrageous conditions, compacted plasma (called "plasma pinch") and the controlled thermonuclear fusion plasma can be produced, where the plasma densities of $10^{26}\mathrm{m}^{-3}$ and plasma temperature over 10^8 K (150 million °C) can be attained.

2.2 Magnetically Confined Plasma

Plasmas sometimes mimic like fluids, while sometimes behave like a collection of single particles at low density. The easiest step to get to know this schizophrenic nature is to understand single particle motions with a prescribed initial velocity in the prescribed electromagnetic field. In a uniform magnetic field $\boldsymbol{B}$, a single charged particle of mass m and charge q, moving with velocity $\boldsymbol{v}$, experiences the Lorentz force, $\boldsymbol{F}$:

$$\boldsymbol{F} = q(\boldsymbol{v} \times \boldsymbol{B}) \tag{2.1}$$

The direction of the force is perpendicular to the direction of motion and the magnetic field as shown in Fig. 2.1, and thus the charged particle will always spin around the applied magnetic field line with a Larmor radius:

$$r_{L_{e.i}} = \frac{m_{e,i} v_{\perp}}{qB} \tag{2.2}$$

where $r_{L_{e.i}}$ and $m_{e,i}$ is the Larmor radius and the mass of electron or ion respectively, $v_{\perp}$ is the component of the velocity of the charged particle perpendicular to the direction of the applied magnetic field.

Since the charged particle does not experience any magnetic force in the direction parallel to the magnetic field lines, it will move at a constant speed along the magnetic field line and the trajectory is a helical spiral around a magnetic field line [8]. The magnetic field helps to confine the charge particles by limiting their motion in the direction perpendicular to the magnetic field within a Larmor radius.

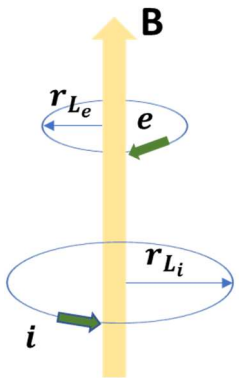

Figure 2.1: Trajectory of electron and ion in magnetic field (for the case without parallel velocity component along the magnetic field).

For designing a magnetically confined device, A favorable topology of the system is "toroidal" within a doughnut shaped vacuum chamber. Tokamak is one of such toroidal devices. However, a toroidal magnetic field does not have a spatial uniformity. The strength of the magnetic field is maximum near the inner wall of the vessel and minimum at the outer side. Because of the inhomogeneous field, there is a gradient in the inward direction of the toroidal chamber which leads to the so called Grad-B particle drift in the vertical direction. The direction of the drift depends on the charge of the particles. The Grad-B drift is written as:

$$v_{\nabla B} = -\frac{m_{e,i} v^2}{2q} \frac{\nabla B \times B}{B^3} \tag{2.3}$$

This vertical drift of ions and electrons in the opposite direction induces a vertical electric field ($E_{\perp}$), which drive the plasma toward the outer side of the chamber. This generates another type of drift is called $\boldsymbol{E \times B}$ drift, which in turn moves the charge particle perpendicular to both magnetic and electrical fields at a velocity expressed as:

$$\boldsymbol{v_{E\times B}} = \frac{\boldsymbol{E\times B}}{B^2} \tag{2.4}$$

The drift direction is independent of the sign of the charge and both electrons and ions drift in the same direction. The overall result of Grad-B and drift shown in Fig. 2.2, obviously, cause the whole plasma to move toward the outer wall of the torus, and leads to the plasma loss.

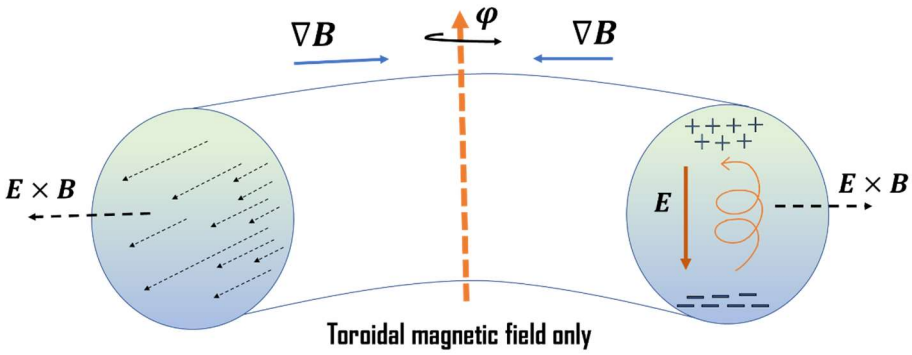

Figure 2.2: Grad-B and $\boldsymbol{E \times B}$ drifts in a toroidal magnetic field.

It is possible to avoid the drifts, by a poloidal magnetic field (B_{θ}) produced by toroidal plasma current (I_p) depicting in Fig. 2.3. The combined toroidal and poloidal field generates a helical magnetic field. The ions (electrons) initially drifted to the top (bottom) will follow the helical magnetic field to stream to the bottom(top) and thus shirt out the charge separation and vertical electric field [9]. As the result, this effect the unwanted plasma loss is avoided.

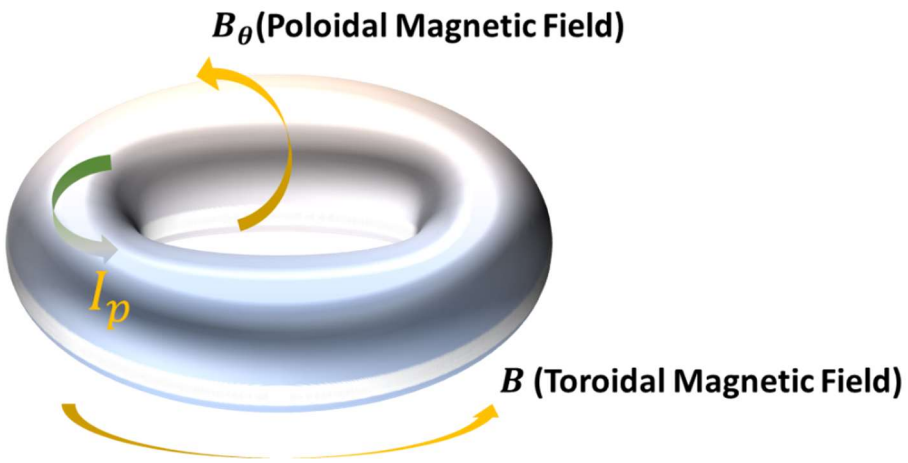

Figure 2.3: Toroidal and poloidal magnetic field direction (yellow) and poloidal current direction (green) in magnetically closed plasma.

An additional vertical magnetic field in needed to overcome the "hooping effect" of the toroidal current loop with a tendency to expand. The combination of those magnetic field components plays a significant role in establishing the equilibrium of the plasma inside the vacuum vessel.

2.3 From Kinetic Theory to MHD

There are three stages of explanation for a macroscopic system: the microscopic theory, kinetic theory, and the fluid or macroscopic description. The exact microscopic description should use Newton's equation, $\boldsymbol{F} = m\boldsymbol{a}$ for each of about 10^{22} particles in the system and solve about 10^{22} trajectory equations. The coupling between those equations comes from the collisions and the electromagnetic field generated by those moving charges. It is an impossible to solve the N-body problems even with the computing capacity in the world. By applying the statistical approach, the microscopic theory turns into kinetic theory.

To calculate the average value of any physical property of the macroscopic system, let us consider particles' motion in a 6-D phase space composed of position $\boldsymbol{r}$ and velocity $\boldsymbol{v}$. The property of the plasma is described by a distribution function $f_\alpha(r, v, t)$ denpedent of their velocities and positions. This distribution function represents the number of a particular kind (α =

i, e or n for electrons, ions and neutral particles) of species per unit volume (6-D volume $dxdydzdv_x\ dv_ydv_z$at time t near position vector $\boldsymbol{r}$ and velocity $\boldsymbol{v}$. the density $n(\boldsymbol{r},t)$ is calculated from velocity distribution function $f_\alpha(r,v,t)$ by simple integral:

$$n_\alpha(\boldsymbol{r},t) = \int_{-\infty}^{\infty} f_\alpha(\boldsymbol{r},\boldsymbol{v},t)d\boldsymbol{v} \tag{2.5}$$

where $d\boldsymbol{v}$ is a 3D volume element in the phase space.

The evolution of the distribution function $f_\alpha(r,v,t)$ on the seven independent variables (x,y,z,v_x,v_y,v_z,t) is expressed by Boltzmann equation:

$$\frac{\partial f_\alpha}{\partial t} + \boldsymbol{v}\cdot\nabla f_\alpha + \frac{\boldsymbol{F}}{m}\cdot\frac{\partial f_\alpha}{\partial \boldsymbol{v}} = \left(\frac{\partial f_\alpha}{\partial t}\right)_{\boldsymbol{c}} \tag{2.6}$$

where $\boldsymbol{F}$ is the averaged interparticle and external force acting on the particles, ∇ represents the gradient in (x,y,z) space and $\frac{\partial}{\partial \boldsymbol{v}}$ stands for the velocity gradient. The right-hand side term $\left(\frac{\partial f_\alpha}{\partial t}\right)_{\boldsymbol{c}}$ stands for the rate of change of probability distribution term due to collisions in the system.

For hot plasmas, collision terms can be neglected and thus for entirely electromagnetic force $\boldsymbol{F}$ equation (2.6) can be written as:

$$\frac{\partial f_\alpha}{\partial t} + \boldsymbol{v}\cdot\nabla f_\alpha + \frac{q}{m}(\boldsymbol{E}+\boldsymbol{v}\times\boldsymbol{B})\cdot\frac{\partial f_\alpha}{\partial \boldsymbol{v}} = 0 \tag{2.7}$$

This equation is known as Vlasov equation. However, the precise locations or trajectory of single particles are lost in kinetic theory. Thus, even after employing the statistical average, kinetic theory is still a macroscopic description.

In order to identify the macroscopic quantities like temperature, fluid velocity and density, we need to calculate the velocity moments of $f_\alpha(\boldsymbol{r},\boldsymbol{v},t)$, which will explain the time-evolution of the macroscopic plasma system. Surprisingly, most of the plasma processes can be explained by fluid model. In this approximation, plasma is considered as a fluid containing two or more interpenetrating fluids. Let's take momentum moments of Boltzmann equation:

$$m\int \boldsymbol{v}\frac{\partial f_\alpha}{\partial t}d\boldsymbol{v} + m\int \boldsymbol{v}(\boldsymbol{v}\cdot\nabla)f_\alpha d\boldsymbol{v} + q\int \boldsymbol{v}(\boldsymbol{E}+\boldsymbol{v}\times\boldsymbol{B})\cdot\frac{\partial f_\alpha}{\partial \boldsymbol{v}}d\boldsymbol{v} = \int m\boldsymbol{v}\left(\frac{\partial f_\alpha}{\partial t}\right)_{\boldsymbol{c}} d\boldsymbol{v} \qquad (2.8)$$

The first integral gives

$$m\int \boldsymbol{v}\frac{\partial f_\alpha}{\partial t}d\boldsymbol{v} = m\frac{\partial}{\partial t}(n\boldsymbol{u}) \qquad (2.9)$$

where $\boldsymbol{u}\ (=\overline{\boldsymbol{v}})$ is the average fluid velocity of the particles. Using the fact that $\boldsymbol{v}$ is an independent variable and is not related to ∇, the second moment integral can be written as:

$$m\int \boldsymbol{v}(\boldsymbol{v}\cdot\nabla)\,f_\alpha\,d\boldsymbol{v} = m\int \nabla\cdot(f_\alpha \boldsymbol{v}\boldsymbol{v})d\boldsymbol{v} = m\nabla.\int f_\alpha \boldsymbol{v}\boldsymbol{v}\,d\boldsymbol{v} = m\nabla\cdot(n\overline{\boldsymbol{v}\boldsymbol{v}}) \qquad (2.10)$$

Let $\boldsymbol{v} = \boldsymbol{u} + \boldsymbol{w}$, the sum of the average fluid velocity $\boldsymbol{u}$ and the thermal velocity $\boldsymbol{w}$. The above equation can be written as

$$m\nabla\cdot(n\overline{\boldsymbol{v}\boldsymbol{v}}) = m\nabla\cdot(n\boldsymbol{u}\boldsymbol{u}) + m\nabla\cdot(n\overline{\boldsymbol{w}\boldsymbol{w}}) + m\boldsymbol{2}\nabla\cdot(n\boldsymbol{u}\cdot\overline{\boldsymbol{w}}) \qquad (2.11)$$

The last term in equation (2.11) becomes zero as the average of the $\boldsymbol{w}$ is zero and the second term represents the stress tensor $\boldsymbol{P}$**.** The third integral in equation (2.8) can be solved as:

$$\int \boldsymbol{v}(\boldsymbol{E}+\boldsymbol{v}\times\boldsymbol{B})\cdot\frac{\partial f_\alpha}{\partial \boldsymbol{v}}d\boldsymbol{v} = -qn(\boldsymbol{E}+\boldsymbol{u}\times\boldsymbol{B}) \qquad (2.12)$$

Using equations (2.9), (2.10), (2.11) and (2.12) in equation (2.18) and be given as:

$$mn\left[\frac{\partial \boldsymbol{u}}{\partial t} + (\boldsymbol{u}.\nabla)\boldsymbol{u}\right] = qn(\boldsymbol{E}+\boldsymbol{u}\times\boldsymbol{B}) - \nabla\cdot\boldsymbol{P} + \boldsymbol{P}_{ij} \qquad (2.13)$$

where $\boldsymbol{P}_{ij}$ represents the momentum gain by *i* fluid due to collisions *j* fluid and this equation is known as fluid equation of motion.

The fluid equation keeps the track of ion and electron fluids separately. This is also known as 'two fluid' equation. With the further simplification, both the equations can be combined to

express as a ‘single fluid’ equation [10]. If the plasma motions fluctuate slowly or for non-relativistic plasma motions under magnetic and mechanical forces, then the Magnetohydrodynamics (MHD) model is the appropriate method. The main difference between the MHD model and the neutral fluid model is the inclusion of the electromagnetic fields produced and experienced by the charged plasma fluid. In chapter 3, the dynamic of the pinch in DPF devices has been presented with the help of the MHD model.

2.4 Fusion Reactions and Plasma

The process in which two lighter nuclei fuse to form a heavier nucleus with release of an enormous amount of energy is termed as "Nuclear Fusion". The resulting product must have higher binding energy per nucleon. It turns out that fusion reaction is favorable for the elements with a lower atomic number than iron, which shows the highest binding energy per nucleon among all the existing elements. The inequality between the reactant and product mass accounts for the energy released during the reaction.

Nuclear fusion reaction probability is characterized by the reaction cross-section $\boldsymbol{\sigma}$ and energy yield Q. The rate of the nuclear reaction, i.e., the number of reactions per unit time per unit volume, is proportional to $<\boldsymbol{v\sigma}>$, the average of the product of relative velocity $\boldsymbol{v}$ and cross-section $\boldsymbol{\sigma}$. For commercial nuclear power plants, the cross-section must be high, and the reaction must be exothermic (Q > 0). The cross-section for deuterium-tritium nuclear reaction is large enough to support reaction in the fusion reactor under less stringent conditions compared with other fusion reactions. Moreover, the D-T nuclear reaction shows a little variation in the reaction cross-section at the energy range 10-30 keV. As per the law of conservation of mass and energy, the net energy produced during the reaction splits into the products in inverse proportion to the product masses.

$$ {}_{1}^{2}D + {}_{1}^{3}T \longrightarrow {}_{2}^{4}He(3.5\text{MeV}) + {}_{0}^{1}n(14.05\ \text{MeV}) $$

However, this is not the only objective of fusion experiments. Despite its required outcomes, there are many limitations which make it less sustainable. Deuterium exists abundantly in the sea water (0.03% mass). As far as fuel self-sufficiency [11] concerned, tritium is a radioactive isotope of hydrogen and is not abundantly available naturally on the Earth. It is possible

to breed tritium by bombarding lithium isotopes with neutrons produced from the fusion reaction [12].

$$^{6}_{3}Li + ^{1}_{0}n \longrightarrow ^{4}_{2}He + ^{3}_{1}T \qquad (4.78\ \text{MeV})$$

$$^{7}_{3}Li + ^{1}_{0}n \longrightarrow ^{4}_{2}He + ^{3}_{1}T + ^{1}_{0}n \qquad (-2.466\ \text{MeV})$$

For this purpose, Li breeding modules can be incorporated in a protective blanket surrounding the core of a fusion reactor as shown in Fig. 2.4.

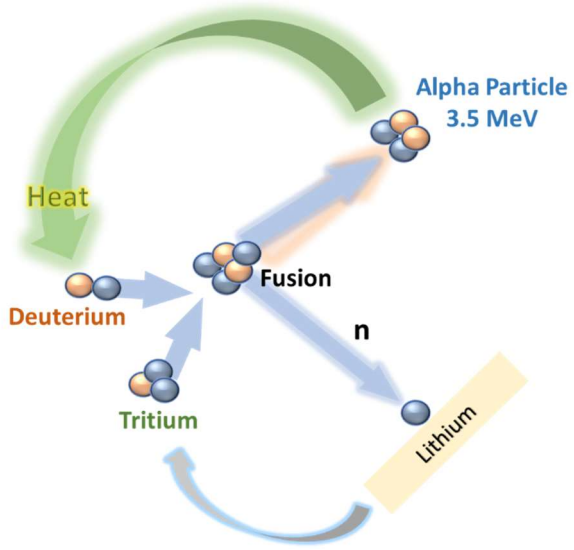

Figure 2.4: Graphic representation of self-sustained deuterium-tritium fusion and tritium breeding via lithium breeding modules.

Nuclear fusion reactions occur between two positively charged nuclei at a short distance (about 1-3 fm) within the strong nuclear interaction range. The two positively charged nuclei must overcome the repulsive long-range Coulomb potential barrier to get close enough. Only head-on collisions will avoid scattering so they get close enough. The approach is to heat up the fuels to over 100 million degrees Celsius so the random thermal motion of particles will ensure some of

the particles will experience head-on collisions at high relative velocities and result in fusion reactions. Fuels at such high temperature are all in the ionized state called plasma, the fourth state of matter in addition to the solid, liquid and gas states. Since the fusion reaction cross-section is low, large number of high energy particles in the reactor will hit the wall and the in-vessel components, depositing large amount of heat on and causing damage to the first-wall materials. The energetic particles from fusion reactions contribute to wall heating and damage as well. It is an engineering challenge on the path towards harnessing the fusion energy.

2.5 Plasma-Wall Interaction

In a magnetically confined thermonuclear fusion reactor, PWI involves all the processes that occur during energy-mass exchange between surrounding walls and plasma. Fig. 2.5 shows the main processes involved in PWI including reflection, recycling, retention, erosion, sputtering, re-deposition and co-deposition. Energetic ions and electrons from plasma, photons radiated from plasma, and neutrons as fusion reaction all directly irradiate the plasma-facing components. PWI modifies the material properties as well as affects plasma by introducing impurities from the eroded walls.

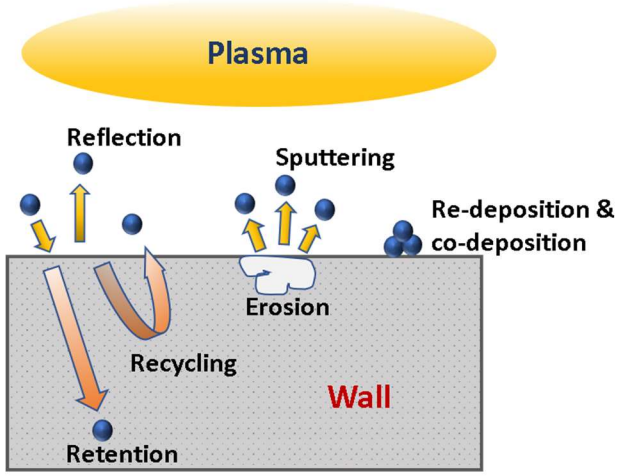

Figure 2.5: Main processes involved during the interaction of high energy particles with chamber walls.

During bombardment, some of the particles are instantly released from the wall and enter the plasma as impurities. Some remain there in the wall material for a specific time before returning to plasma (recycling). However, a small fraction of the incident particles gets trapped in the wall (Long-term retention). Interaction of highly energetic particles causes erosion of the wall material. The released particles get ionized and enter the plasma. Unless these particles are pumped out, they must get re-deposit on nearby or some different locations along with fuel material. This forms co-deposited layer with mixed-materials on the PFCs.

Surface erosion can be the result of structural changes on the material surface due to hydrogen and helium bubble trapping. These bubbles formation beneath the surface form fuzz or flakes. those effects could cause embrittlement, hardening and reduction in thermal conductivity on the W-wall. Investigation of subsurface bubble trapping is a topic of interest when it comes to the design of PFCs which can withstand extreme heat fluxes in the reactor.

In 2011, the ITER organization (IO) recommended to replace CFC with W monoblock technology within a specific timescale (before 2013). IO established a tungsten divertor task force to coordinate the activities for design development and to check the design validation [13]. Japan Atomic Energy Agency (JAEA) has taken the responsibility to review load-carrying capability tests for W monoblock. By the end of 2013, full W divertor was implemented in the ITER baseline design [14, 15].

The work done by the task force leads to extending the requirements such as a rise in heat loads to 10 MW/m^2 while operating at steady state and to 20 MW/m^2 in a slow transient state. This increase in the heat load on the W monoblock led to high thermal resistance and required an improved armor heat sink joint. However, at 20 MW/m^2, numerous macro cracks have been found due to cyclic exposure to very high temperatures. Under those conditions, W monoblock would face thermal fatigue, creep damage, structural deformation due to recrystallization. IO has launched the activity for characterization of W monoblocks to understand the relationship between mono cracks and W properties [16, 17].

2.6 Bubble Evolution Theory

Helium trapping in tungsten proceeds through distinct stages including the ion implantation, nucleation, growth and coarsening [18]. Interactions of energetic helium ion with W surface result in helium ion implantation, followed by energy loss in atomic and electronic collisions. These

collisions lead to the permanent displacement of atoms, Frankel pair generation and deposition of helium atoms in interstitial sites. After that, bubble nucleation starts, where condensation of helium clusters and vacancies are formed. Low energy helium ions do not create Frankel pairs [19]. However, clusters of helium forcibly create Frankel pairs by self-trapping process [20, 21].

The incoming helium atoms get attracted to form small helium bubbles. Once the helium dose reach to threshold limit, bubble swelling due to lateral stress induces bubbles fusion and results into blisters formation [22, 23]. This process continues and bubbles keep on growing. The creation of fresh bubbles and the growth of tiny bubbles take place simultaneously. These bubbles are subjected to external forces due to helium flux, stress and temperature gradient, as shown in Fig. 2.6. Due to these forces, bubbles move randomly or unidirectionally and result in the collapse of bubbles to form a bigger one at the cost of their density. Reduction in bubble density and motion of the bubble toward the surface continues. This stage is called coalescence [24, 25].

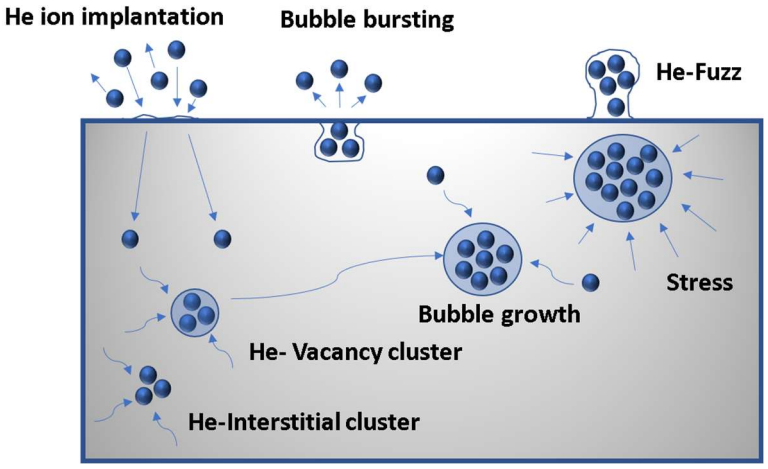

Figure 2.6: Overview of bubble formation mechanism representing four distinct stages from bubble trapping in subsurface to Nano-fuzz formation on the surface.

2.7 Plasma Facing Components (PFC)

The goal of the ITER project is to demonstrate scientifically the viability to harness more copious amounts of power produced in Deuterium-Tritium (D-T) reactions. Till now, all the research reactors consume more input energy than they generate. JET, which is one of the most successful tokamaks, has achieved Q value (ratio of the power generated by D-T reaction to the input power) of 0.64 [2]. While Tokamak Fusion Test Reactor (TFTR) has delivered Q value of 0.27 [26]. The goal of ITER is to achieve Q ~ 10-20.

The triple product related to the plasma parameters in the reactor, or the so-called Lawson Criterion, describes the required critical parameter (L_c) for fusion reactors:

$$L_c = n_e T \tau_E \tag{2.14}$$

where T is plasma temperature, n_e density and τ_E the energy confinement time.

In the past decades, the temperature and the density has improved with increasing magnetic fields in tokamaks, advanced heating techniques based on wave and neutral beam heating. The energy confinement time has been seen increased by increasing the volume of plasma vessels as well. With the increase in the vessel volume, the heat load on plasma-facing material has also been increased in proportion to R^3 where R is the major radius of the tokamak vessel. However, the surface area required for heat-dissipation increased only by R^2. Therefore, the wall heating load increases with the size of the tokamak device

Apart from the magnetic field, the design of PFC geometry can be used for plasma shaping to reduce the plasma impact on the most of surface and guide the particles to the surface of the specifically engineered surface that can withstand the high heat deposition and furious particle bombardment. This lead to lesser requirement on the most of the vessel surface and stringent requirement of the particle-intercepting divertor surface. A modern divertor configuration with both divertor and limiter regions is shown in Fig. 2.7.

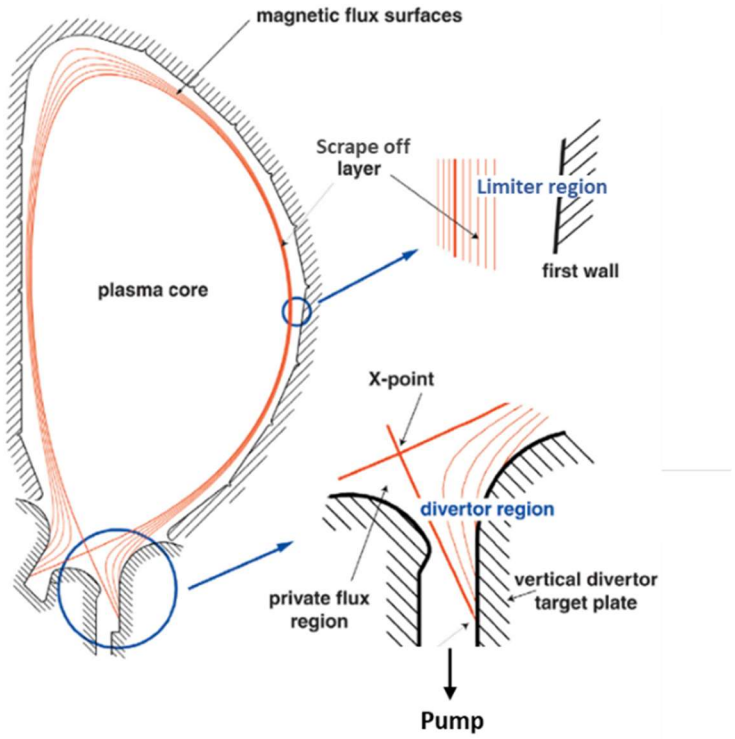

Figure 2.7: DEMO Tokamak: Vertical cross-sectional view of magnetic flux surfaces near divertor and limiter regions. [27]

In an older limiter configuration, plasma-material interactions occur at the limiters. A limiter defines the edge of the plasma and thus, limits expansion of the hot plasma to the whole vessel surface. Its basic function is to protect the first wall from damage and therefore, it should be so built that it can withstand high heat flux and exhibits good thermal conductivity and low atomic number as it will explained later. The biggest disadvantage is that it will add impurities and may increase the power loss to radiation from plasma.

Diverted configuration is used to resolve the issues noticed with limiters. About 90% of the output energy is radiative in nature and is dissipated on the vessel armour tiles. The remaining 10% of the thermal energy are carried by the particles which is guided by magnetic field lines and collected by the divertor plates inserted at the base. Divertor plates work as an exhaust system in the reactor which extract heat energy, helium and other debris from the reactor surfaces. Thus, divertor is the most stressed component in a fusion reactor.

Other in-vessel components such as the antenna for radio-frequency wave heating also require heat shield which intercepts particles as well.

2.8 Plasma-Facing Materials (PFM)

Owing to extremely harsh environmental conditions, development of suitable PFMs is still a key problem to be resolved. Selection of PFMs for the plasma facing components in fusion reactors depends upon certain requirements of the machine, but in general, the standard properties of PFMs to be considered includes (a) thermomechanical stability,(b) erosion lifetime and sputtering resistance, (c) neutron radiation resistance, (d) integrity of heat sink materials, (e) helium and hydrogen effects, (f) tritium retention, and (g) vacuum compatibility.

Interactions between plasma and PFCs are dominated by the surface events up to 10-20 nm in depth [28]. As a result, optimal conditioning of these surfaces becomes a pivotal job for getting the best plasma discharge.

As mentioned earlier, plasma-wall interaction affects plasma performance in three ways, (1) source of impurities (2) fuel recycling and (3) control of the residual gas level in the vessels. Till now, there is no single material with all the PFM properties that can be utilized for the entire plasma-facing area of the fusion reactor. However, there are some potentially suitable materials for the PFCs with different applications in the reactor device.

In the late 1970s, carbon used as PFM in limiter configurations [28]. Carbon based materials have low-activation, low sputtering yield, good machinability and good thermo-mechanical properties at plasma temperatures. They do not get easily melted during abnormal events like the so called Edge-Localized Modes (ELMs) or disruptions [29]. Since the radiative cooling is directly proportional the second order of charge of the impurity ions, Carbon is a good choice for PFC for its atomic number is relatively low compared with most metals. However, it was later found that the hydrogen retention rate increases at high temperatures. The main reason to exclude CFCs is three-fold. Firstly, it is susceptible to radiation damage and neutron irradiation reduces the thermal conductivity of carbon [30]. Secondly, CFCs have high tritium retention rates. Thirdly, it has a high erosion rate, leading to creation of organic by-products and re-deposition problems. Carbon can be easily eroded within a short time and thus requires downtime for replacement, which makes it commercially unacceptable. Doping can reduce the tritium retention

and the erosion rate at the cost of reduction in thermal conductivity [31]. Boronisation, lithium injection, siliconization can help in reducing the oxygen impurities and enhance its density control [32]. However, due to the high risk of tritium accumulation by CFCs erosion, CFCs were excluded from the list of the ITER PFMs. The success of divertor configurations diverted the PFC research community to low-activation materials such as Cr, W, Be and Ta. The choice is made by considering the operational conditions of the reactor as well as the properties of materials [33, 34]. At divertor target and first wall the heat load is anticipated to be as high as 5 MW/m^2 and 1 MW/m^2, respectively. Based on heat load power, Be is an excellent choice as the first wall material [35]. The main advantage of using beryllium as the first wall material is its high thermal conductivity, low Z element and high ability to getter O impurities [36]. The advantage of using low-Z material at high edge temperature (200-400 V) is its effectiveness of reducing the radiation loss compared to other high-Z materials. Beryllium shows an excellent out-gassing characteristics. Various studies found that water vapors and hydrogen dominate Be outgassing [37]. Be was used as a baseline material for divertor and pump-limiter design in the STAR-FIRE and FED-INTOR devices. However, melting due to disruption was enough to eliminate Be from the selection list [38]. Using the same database for disruption survivability of graphite and beryllium, graphite was used in TIBER II [39] and ITER designs [40]. The ability of Be for in-situ repair was neglected in these reactor designs. In-situ plasma gun can be used to deposit 1mm of Be on 6.8 mm^2 in 8 hours. Be has very low solubility with hydrogen and only deposits a saturated layer on the very-near surface, but after long-term exposure, it adds tritium inventory in bulk. The main disadvantage of using Be as PFMs is self-sputtering. The sputtered Be, along with tritium, creates a co-deposition layer on the more cooling zone of the reactor. Potentially kilograms of the valuable tritium fuel are removed to hard-to-reach zones of the fusion device. In addition, Be is highly reactive and even a small trace of carbon can lead to the formation of carbide layer on its surface, causing the so called ‘carbon-poisoning’ [41].

Recently, experimentalists have focused their attention towards broadening the choices for high atomic number materials such as tantalum, hafnium, molybdenum and niobium. Despite that, research is still focused on the tungsten as a single material for divertor application.

2.9 Tungsten

Tungsten is recognized as a primary candidate for divertor sidewalls, divertor dome and lower baffle area, owing to its high sputtering threshold, high melting point (3410 C°) [42], low tritium absorption inventory (2g every 1000 plasma discharges), excellent thermal conductivity (173 W/mK) [43] , low linear thermal expansion coefficient (4.6×10^{-6} K^{-1}) [44] and high resistance to neutron displacement damage [14–20]. Among all the metals, W has the lowest vapor pressure (1.3×10^{-7} Pa at melting point) [45], and thus during the transient events such as ELMs and disruptions during tokamak operation, significant evaporation of the material may not occur even though the heat load on the wall during those events is orders of magnitude higher than usual. This reduce the splashing of the melted PFM into the plasma during transient events. Injection of melted PFMs reduces the chamber temperature which affects the plasma performance.

Migration and retention of hydrogen is strongly determined by the diffusion of the material. For hydrogen, W is an endothermal material. Trapping of hydrogen in grain boundaries, gas bubbles, dislocation can be studied by modelling hydrogen transport in tungsten. This required a reliable data for solubility and diffusivity of hydrogen in tungsten. The most quoted expression for the diffusivity determined at the large range of temperatures, $D = 4.1 \times 10^{-3} e^{-9000/RT}$ cm^2 /sec, was reported by Frauenfelder [46]. There is very limited database for the solubility of H in tungsten material. Along with diffusivity, Frauenfelder also found that the solubility depends on the temperature in the similar to the dependence of the diffusivity on the temperature for 99.95% pure W material at the temperature range 1100-2400 K. Mazayev *et al.* [47] also studied the solubility of hydrogen in tungsten at higher temperatures 1900-2400 K and the findings agree with the data reported by Frauenfelder [48]. A low solubility value represents the desired low tritium absorption [49].

Despite these good properties, using tungsten as PFM is hampered by its brittleness. During the transient events, W may undergo thermal damage. This problem drastically increases during major disruptions of the tokamak operation [13]. The melting of tungsten during ELMs could be another major issue. Another critical problem with tungsten is its high atomic number, which is responsible for plasma cooling due to radiation. Eroded wall material has a relatively low temperature compared to plasma and leads to radiative cooling.

PFMs must lie within the Operating Temperature Window (OTW) of the device, which is in the range of 1073-1473 K. In Body-Centred Cubic (BCC) crystal and most of the face-centred cubic (FCC) crystals, OTW is defined by recrystallization temperature at the upper limit and Ductile-to-Brittle Transition Temperature (DBTT) at the lower limit. Hence, it is convenient to have DBTT as low as possible [50]. It should have low ductility and toughness to prevent any brittle fracture at the lower limit of OTW. DBTT for pure tungsten is in the range of 473-673 K. It can be used as structural material by decreasing its DBTT. Tungsten alloys, ultra-fine grain tungsten and its availability in wrought as well as the powder grain form can provide an alternative to brittle tungsten. In addition to neutrons, He^+ and D^+ irradiation leads to thermal, mechanical, and surface morphology changes on the W surface. As a result, plasma dynamics and the structural properties of the W are affected by changes in the surface morphology and thermal-mechanical properties, respectively. It is necessary to understand the mechanism of evolution in W-based PFC, reverberation of these changes and the methods to design new tungsten materials optimized for PFCs.

One of the efficacious ways for enhancing the ductility and mechanical strength of tungsten is by reducing the grain size to the nano-range or ultrafine. For instance, fracture toughness of ultrafine grained tungsten developed by Severe Plastic Deformation (SPD) has significantly improved as compared to micron-sized tungsten grains [51]. Radiation damage can be improved by nano structuration of the material, as the grain boundaries act as sinks for irradiation induced defects [52]. Kurishita *et al.* [53] found the similar results for the nanostructured, toughened, fine-grained, and recrystallized W (TFGR W). Thermal Desorption Spectrometry (TDS) apparatus revealed hydrogen retention on the exposed targets and found that TFGR W is quite insensitive to radiation damage. The study of irradiation damage of nanocrystalline Pd and ZrO_2 powder showed a direct relation between grain size and the defect density [54]. The surface area and porosity of fiber form nanostructure tungsten play a crucial role in tritium retention. With the increase in the helium fluence the thickness of the nanostructure layer increases as well. Despite the porous nanostructure layer, the diffusion of Tritium was slow [55]. The performance of nanocrystalline, ultrafine, and ITER grade W was investigated when they are irradiated to high fluence helium at room temperature and at 773 K. The TDS results showed the importance of grain boundaries in helium trapping [56]. Han *et al.* [57] studied the He induced damage on coarse-grained (CG), single-grained (SG) and nano-grained (NG) Cu films.

Maximum cavities were decorated along the grain boundaries in (NG) Cu and few in the grain interior. The number density of the induced holes was found to be lesser in (NG) Cu film. Therefore, it is critically very important to study the effect of the high heat flux on the nanostructured tungsten as an alternative PFM. In this Masters thesis, nano-structuration of W has been synthesized and studied as an alternative to PFMs.

2.9.1 Tungsten PFCs under fusion equivalent conditions

As stated earlier, tungsten undergoes serve modifications around the fusion plasma relevant to conditions. It exhibits structural, morphological and mechanical changes under He^+, D^+ and neutron irradiation. Over recent years, many theoretical and experimental studies have been carried out to analyze the detrimental effect of thermo-mechanical and structural modification on plasma-wall interactions. In 2006, Takamura *et al.* [58] were the first who reported the tungsten nanostructures, and detailed TEM analysis of the subsurface damage revealed trapped nano-sized gas bubbles.

The evolution and growth of the surface nanostructures found to be related to trapped bubbles. However, the growth rate is not directly related to the implanted ions and voids in the material [59]. At low temperatures < 800 K, blistering [60] and at high temperatures > 1600 K, holes and gas bubbles [61] due to hydrogen and helium irradiation have been noticed. The size of these bubbles depends highly on the irradiation temperature [62]. The thermal conductivity and optical reflectivity were found to reduce drastically due to these nanostructures [63]. The mechanisms that behind these evolving material properties are not crystal clear but diffusion of deuterium and helium accumulation in defect sites and vacancies have been acknowledged.

Previous studies showed that hydrogen plasma creates lesser damage on the tungsten surface. On the other hand, He plasma causes severe damage on the exposed surface even the energy is far below the required sputtering threshold. Therefore, it is important to analyze the behavior of tungsten under high-flux, low energy He plasma. In the following subsection, a brief literature review on the adverse impact of He^+ irradiation on tungsten will be presented.

2.9.2 Impact of high-flux He^+ irradiation

The ruinous aftermath of He^+ in tungsten is signified by its fast-thermal diffusion through the interaction with defective sites (impurity atoms, vacancies) and even with themselves. The consequential displacement damage due to He ion irradiation are confined in the sub-surface region (about 10 nm or less). The radiation induced point defects and implanted helium atoms are cumulated there by clump formation [64].

The intricate He-induced damage in W fluctuates with the fluence, the amount of helium absorbed, irradiation energy and temperature. Grain boundaries emulate as trapping sites for helium and are related to fuzz formation. Lot of experimental results have suggested that helium accumulates at grain boundaries [65]. The response of W-Ta to low energy helium irradiation at different temperatures revealed a direct relationship between the atomic spacing of the target material and the cumulated damage. A proportional increase in fluence threshold value for fuzz formation with an increase in the Ta wt% concentration was also reported [66].

Fuzz formation has been reported nearly on all known tungsten grades. The minimum ion energy required for fuzz formation is approximately 20 eV. However, upper bound is still not clearly defined (~250 eV). Much higher energies leads to sputtering of tungsten surface and eventually degrade the material quality. At low fluence, no fuzz was found within the energy range 30-250 eV [67]. At room temperature and low flux (nearly 2.3×10^{16} ions/m^2 s) the range of the diffused helium was about 440 nm and the damage near the surface was 1.59 displacement per atom (dpa). Helium retention is effectively influenced by incident ion with several keV energies [68]. It was reported that the presence of helium induced damage on W enhances the D retention by 4-5 times compared to unexposed W [69]. Transmission Electron Microscope (TEM) analysis showed a strong dependency of temperature on the microstructural defects such as nucleation on interstitial loops induced. They found that D-T burning devices experience radiation damage at the incident ion energy lower than the threshold energy required for knock-on damage [70]. The detailed mechanism of microscopic structural damage of tungsten irradiated by high-flux and low energy He^+ is still an unresolved mystery. High heat loads results in material recrystallization which affects irradiation-induced surface damage. Dual-beam ion-irradiation increased the recrystallized W hardening much higher than single-beam at 1000 °C. He irradiation will increase the growth of micro-cavities and dislocation loops and therefore increase material hardening. Another reason could be the grain-boundary effect which acts as a sink for vacancies and defects

[71,72]. The formation of He bubbles due to irradiation affects the hardness value at the sub-surface region and is drastically enhanced by the high ion fluence [73]. If the size of these induced defects is bigger than that of dislocation loops, then they are called as dislocations lines. Only immobile defects (dislocation loops, helium bubbles) can uptight the dislocation motion. Therefore, the dislocation lines hardly show any impact on the material hardness. Kong *et al.* concluded that increment in the hardness is mainly due to the helium bubbles. Helium bubble diameter plays a major role in enhancement of hardness factor rather than the density of the trapped helium bubbles [74].

At low temperatures (< 873 K), helium vacancies absorb more helium to create dense helium bubbles. At high temperatures (1073 K – 1273 K), helium bubbles and vacancies with high thermal migration evolve large size helium bubbles [22]. The evolution of internal damage and changes in thermomechanical properties in plasma-facing materials due to helium ion irradiation depend on temperature, fluence, and ion energy. Nishijima *et al.* [75] investigated the dependency of the surface temperature on the bubble formation and related that dependency to the diffusivity of the vacancy and helium atoms in tungsten. The thermal vacancy density plays a significant role as a trap site leading to bubble evolution. Dense and fine He bubbles form a thick, damaged layer in the subsurface region at low temperatures. This internal damage induced the surface hardening and reduction in the ability to conduct the heat. In the high-temperature region, the bubble density reduces with the growth in the bubble size [64]. Cui *et al.* [76] were the first to use a method based on molecular dynamics to study the lifetime of helium bubbles trapped near the tungsten surface and the rate of helium bubble bursting. They argued that the He bubble bursting is an active event. In the temperature range of 1000 K-2000 K, the average lifetime of the bubble can exist from picosecond to microsecond. Molecular Dynamic Simulation (MDS) demonstrates the mechanism and conditions for helium bubble formation, which is believed to be an initial stage of nano-fuzz formation in tungsten. These over-pressurized helium bubbles trapped in the subsurface lead to significant surface changes like carters or pinhole [77]. Even a low energy helium ion can modify the exposed material surface effectively. At 1600º C, irradiation of 10 eV helium ions result into surface pores [78]. Similar results of large bubbles (15-150 nm diameter) and semi-porous layer on incident surface with 30 keV helium ions have been reported by Sharafat *et al.* [79]. A published paper showed that surface modification and degradation of tungsten properties as PFM is strongly

related to the helium bubble formation [80]. This gives the idea of engineering the grain boundary density that could be an indispensable tool for regulating this destructive phenomenon.

2.10 Plasma Aided Nanotechnology

Nanotechnology is a branch of material science which deals with the manipulation of materials on the atomic or molecular level to design material and devices with new fundamental properties. Scaling down of materials into nanometer-scale has brought revolutionary change in a wide range of industries. The development and optimization of various nanomaterial synthesis technology is a vibrant topic of research in the era of nanotechnology. One of the most versatile tools for nanomaterials synthesis is plasma-assisted processes as it provides high deposition rate [81], facilitates phase transitions [82] and surface reconstruction, and produces dense thin films [83]. There are two basic fabrication methods to build nanoscale materials. The "bottom–up" technique processes create nanomaterials from atomic and molecular level. Those atoms or molecules self-assembles by a natural phenomenon or some external driving force to create an organized and bigger particle. The "top–down" processes involve fabrication of nanoscale materials from large counterparts and eventually uses finer tools for designing corresponding nano-structures. A lot of scientific and commercial attempts for conceptualization and optimization of new possible routes have been made for nano-synthesis. Many new novel phenomena have been discovered and new characterization techniques invented. Many methods, including chemical routes, vapor condensation methods and nature's biological method, have been used for synthesizing nanoscale materials with new characteristics. The plasma-assisted processes referred as "plasma nanotechnology", have turned into one of the most flexible tools for synthesis of nano-materials as plasmas facilitates a fast, complex and reactive chemical process [85].

There are broadly two types of plasma used in nano-industries - cold plasma (low-temperature plasma) and hot plasma (high-temperature plasma). The temperature of the cold plasma currently used by industry and material research community is in the range from small fraction to a few tens of electron-volts. The cold plasmas can be produced by ac or dc glow discharge, by inductively coupled radio-frequency discharge, or by microwave technology. The ionization degree in low-temperature plasmas is low and the working gas is mostly in the neutral state. The cold plasma can further be divided into equilibrium and non-equilibrium plasma. The

equilibrium or thermal plasma has equilibration of temperatures i.e. $T_g \sim T_i \sim T_e$ (T_g , T_i and T_e are the temperature of background gas, ions and electrons respectively and represent their mean kinetic energy) due to the frequent collisions between the electrons, ions and neutral species. The thermally nonequilibrium plasmas are produced under several conditions. Firstly, when the operating temperature is too low, there are insufficient collisions between charged species and neutrals to achieve equilibrium. Secondly, equilibration process in short-lived plasma is disturbed in pulsed discharges in spite of high collision rate at high operating temperature. Finally, high electric fields increase the electron kinetic energy and reduce at least one of its dimensions to micron size. Generally, the nonequilibrium plasmas are usually characterized by the relation $T_g = T_i << T_e$.

Hot plasmas can be categorized in the high temperature regions from several to few tens of keV with almost fully ionization state. The High-Energy-Density (HED) high temperature plasmas are heated and pinched at high energy densities ~10^0-10^{10} J/m^3 [86].

The features which make it far more efficient for material study than cold plasma are listed below:

1. High ions and electrons temperature as compared to other processes.
2. Very high plasma density.
3. Required lesser processing time compared to DC pulse generator and RF glow discharge.
4. Gas consumption is low compared to other plasma-based nano-techniques.
5. Very high flux and ionization rate.

High-power long pulsed lasers (10^{-9} sec range) and high-energy short pulse (10^{-15} sec range) laser-plasma system [87], and pulsed high current Z-pinch devices [88] are the examples of HED plasma facilities. The one device that belongs to a group of hot plasma is DPF device used in my research project. The energy density of DPF (i.e. the ratio of energy stored in high voltage capacitor bank to the volume of the cylindrical compressed plasma column) is noted to be (1.2−9.5)×10^{10} J/m^3 [89], which brings it in the group of HED plasma devices.

The DPF device is a type Z-pinch and is able to produce an abundant of energetic electrons, fast ions, soft/hard X-rays and intense neutron flux. DPF attracted attention of research community 1970s and was viewed as one of the most suitable choice for controlled thermonuclear fusion reactor [90]. This versatile and intense radiation source has wide variety of applications

such as production of short-lived radioisotope [91], highly ionized species production [92], X-ray radiography and imaging [93].

DPF as a material synthesis device is used for the treatment and modification of the bulk materials and thin films, and to lesser extent for synthesis of a particular material. For the very first time Feugeas *et al.* reported the nitriding of the American Iron and Steel Institute (AISI) 304 stainless steel with the nitrogen ions produced in DPF discharges. The mechanical analysis showed the wear reduction of 42 order compared to the untreated samples. X-ray Photoelectron Spectroscopy (XPS) analysis found the formation of the precipitation of Fe_2N precipitate formation, in a homogeneous ~0.3-μm-thick peripheral layer [94].

Later, Rawat *et al.* [95] used DPF device for crystallization of lead zirconate titanite (PZT) thin film with a single exposure to the fusion device using argon as working gas. It has been found that the operating device requires optimization of some parameters, for example operating pressure, exposure sample distance, bank voltage etc. In addition, some post-processing techniques such as rapid thermal annealing and post deposition annealing is also required. With DPF, crystallization effect is achieved by the intense heating and melting of the amorphous material. The heat extends to the entire surface from the thin film until it reaches to the film-substrate interface. Once it gets cool, material crystallizes. Unlike the traditional method, DPF can generate similar effect at room temperature in short period of time.

After the establishment of plasma focus device with their surprising outcomes, Kant *et al.* [96] successfully synthesized carbon thin film by exposure of graphite substrate with argon ions. The mechanism used in this process is very much like the RF generated plasma. However, more intense, hot and dense plasma produced in the DPF device makes it more efficient than the RF plasma generator. With 10 to 30 number of shots, 100-150 nm thick crystallized carbon thin film was synthesized on the quartz substrate.

Rawat *et al.* [97] synthesized titanium carbide (TiC) on stainless steel substrate with a mixture of argon and acetylene. With the deposition rate of 30-50 nm/shots, about 1.0μm thick TiC layer can produced. Detailed plasma-chemical mechanism was not discussed in their paper. However, the reduction in deposition rate with the number of shots discuss the competitive etching and deposition mechanism in the plasma focus devices. Several later paper have reported on irradiation of different bulk substrate materials, such as silicon [98,99], tungsten [99], titanium [100-103], zirconium [104], aluminium [105], Iron [106] etc, using different DPF devices. The

successful results from these vast range of qualitative and quantitative experiments proved the plasma focus device as an excellent tool for material synthesis for advanced future materials.

2.11 DPF- First Bench Tester for Plasma-Facing Materials

IAEA has stated that until the International Fusion Materials Irradiation Facility (IFMIF) is designed and operated, Dense magnetized plasma (DMP) devices will act as the first testing step for plasma facing materials, development of technologies and calibration of sophisticated techniques [109]. The collaborative scientific efforts are ongoing under the guidance of IAEA's research project [110] and expected to create (i) strong scientific base for mechanism behind plasma-wall interaction and material's surface modification, (ii) a sufficient data base for damage rates of chosen candidates under different particle and thermal loads. Simulation of similar edge-localized modes and instabilities of tokamaks attained the attention of plasma groups. Study of the deleterious effects of the ion irradiation on the plasma facing materials and their experimental results have been discussed.

Saw *et al.* [111] investigated the destructive effects of deuterium ions with flux of 10^{28} $m^{-2}s^{-1}$ generated by 2.2 kJ plasma focus (PF) device on tungsten samples at different exposure distances. Uniform cracks with width of 300–500 micrometers and cavities up to 5 μm were noticed on the tungsten surface. Dutta *et al.* [112] studied the damage effects of energetic helium ions produced by 2.6 kJ PF device at different axial angles to central anode, irradiated at 10 plasma shots. They reported the development of surface modification and compressive stress on tungsten material. Inestrosa-Izurieta *et al.* [113] used PF-400 J, an intense plasma source to simulate a heat load equivalent to those obtained in tokamaks. The impact of irradiation power on structural modification was identified. Along with compressive stress, some amount of energy was also released in melting events as stress values were not proportional to the radiation power. Bhuyan *et al.* [114] in similar work used low energy plasma focus device to irradiate tungsten sample and examined the proton induced damage at different angular positions with respect to central anode. They noticed the formation of cracks and blisters along with the surface melting events. A reduction in the hardness value of the exposed material was reported. Niranjan *et al.* [115] discussed surface modification of plasma facing materials (stainless steel, copper, nickel, molybdenum and tungsten) exposed in 11.5 kJ DPF device. The SEM analysis showed cracks and

blisters formation and structural phase transformation. With the increase in number of shots, the narrow cracks transformed to larger and deeper cracks. Chernyshova *et al.* [116] found the similar results with PF-1000 and PF-6 devices used for investigating the effects of deuterons on different materials. Hussnain *et al.* [117] synthesized a uniformly distributed tungsten nitride nanocomposite films using a 3.3 kJ plasma focus device. The roughness of the exposed surface became ~52.2 nm at 33 focus shots. The increase in the number of shots resulted in particle agglomeration up to ~180 nm. Improvement in surface hardness was observed under the influence of ion energy dose. Mohammadreza Seyedhabashi *et al.* [118] in another work used low energy Mather type PF device to study the destructive effect of proton and argon ions on W and Cu targets. Morphological analysis showed completely different surface destruction on the target irradiation by Ar and proton. The thermal load transferred to the target was found to be lower in the case of H as compared to Ar. Elastic Recoil Detection analysis was used to find the range of hydrogen beam in Cu and W.

Chapter 3

DENSE PLASMA FOCUS DEVICE

Dense Plasma Focus device is a type of Z-pinch utilizing the magnetic pinch effect. In the following chapter, underlying dense plasma focus dynamics, design structure and operation of the UofS-I will be discussed.

3.1 Pinch Plasma Physics

The principle of a magnetic pinch or plasma pinch is the compression of a carrying conducting fluid by a magnetic field. Usually, this conducting fluid is plasma. Rapid compression results in a plasma with high temperature and high density. Depending upon the current directions, three kinds of pinch configurations have been studied in many laboratories in the world: Zeta pinch (Z-pinch), X-pinch and θ-pinch. One of the easiest ways to generate dense plasma is the Z-pinch. A cylindrical column filled with gas will be broken down due to a high voltage applied by a pair of electrodes drives an axial current, $\boldsymbol{J_z}$, through the conducting fluid (plasma). The current induced a magnetic field B_θ in the azimuthal direction. The Lorentz force, with the direction defined by the cross product $\boldsymbol{J_z} \times \boldsymbol{B_\theta}$, is a radially inward force. The Magnetohydrodynamic (MHD) equations can be used to explain the compression physics of a simple Z-pinch and the operation of DPFs.

Let us consider a uniform line density of a quasi-neutral and isothermal plasma column in which the ions and electrons are at thermal equilibrium. The following MHD momentum equation can be applied to describe the motion of the fully ionized plasma column:

$$mn\frac{D\boldsymbol{v}}{Dt} = -\nabla p + \boldsymbol{J} \times \boldsymbol{B} - \nabla \cdot \boldsymbol{\Pi} \tag{3.1}$$

where n is the particle density, ∇p the pressure force per volume, $\boldsymbol{v}$ the velocity, m the ion mass, $\boldsymbol{\Pi}$ the off-diagonal pressure tensor, and $\boldsymbol{J}$ is the current density.

It should be noted that the plasma thermal pressure is proportional to the plasma density and temperature (T) expressed by $p = nkT$ where k is the Boltzmann constant. The terms ∇p, $\boldsymbol{J} \times \boldsymbol{B}$ and $\nabla \cdot \boldsymbol{\Pi}$ on the right-hand side represent plasma pressure, magnetic pressure and viscosity force. The last term accounts for the stress in the fluid due to inter-particle collisions. However, in this case, diffusion is not much affected by collisions. So, viscous tensor term can be neglected. When the magnetic force $\boldsymbol{J} \times \boldsymbol{B}$ exceeds the pressure force ∇p, the plasma will be accelerated and compressed to increase the density pressure gradient until the two forces cancel each other. This combined force is responsible for plasma compression, and the process is known as pinch effect. Also, the magnetic force is proportional the total current and inversely proportional to the plasma radius. The compression force in a Z-pinch operation at a high current is capable of compressing the plasma to a density of 10^{24} m^{-3} and heat the plasma to a temperature in the range of keV, a set of parameters suitable for fusion reaction.

At equilibrium with maximum compression as the pressure increases with the density and temperature, the inertial terms vanish and the equation (3.1) for equilibrium becomes,

$$\nabla p = \boldsymbol{J} \times \boldsymbol{B} \tag{3.2}$$

or

$$J_z B_\theta = -\frac{\partial p}{\partial r} \tag{3.3}$$

For an axially symmetric system such as the plasma in a long Z-pinch. Since only the radial component exist for an axial symmetric system considered here. It should be pointed out that the above equation also describes the equilibrium of a non-viscous plasma at steady state. If all the quantities are the function of r and $B_r = B_z = 0$,[119], the equation

$$\nabla \cdot \boldsymbol{B} = 0 \tag{3.4}$$

or

$$\frac{1}{r}\frac{\partial}{\partial r}(rB_r) + \frac{1}{r}\frac{\partial B_\theta}{\partial \theta} + \frac{\partial B_z}{\partial z} = 0 \tag{3.5}$$

can be simplified as

$$\frac{\partial B_\theta}{\partial \theta} = 0 \tag{3.6}$$

Due to the symmetry, this satisfies trivially. Under the same assumption, $B_r = B_z = 0$, in the cylindrical coordinate system, the Maxwell's fourth law of electromagnetism,

$$\nabla \times \boldsymbol{B} = \mu_o \boldsymbol{J} \tag{3.7}$$

with displacement current ignored in the plasma case can be written as:

$$\mu_o J_z = \frac{1}{r}\frac{\partial}{\partial r}(rB_\theta) \tag{3.8}$$

where μ_o is the vacuum permeability. From equations (3.3) and (3.7) we get

$$-\frac{\partial p}{\partial r} = \frac{B_\theta}{\mu_o r}\frac{\partial}{\partial r}(rB_\theta) = \frac{B_\theta}{\mu_o}\frac{\partial B_\theta}{\partial r} + \frac{B_\theta^2}{\mu_o r} \tag{3.9}$$

which leads to

$$\frac{\partial}{\partial r}\left(p + \frac{B_\theta^2}{\mu_o}\right) = -\frac{B_\theta^2}{\mu_o r} \tag{3.10}$$

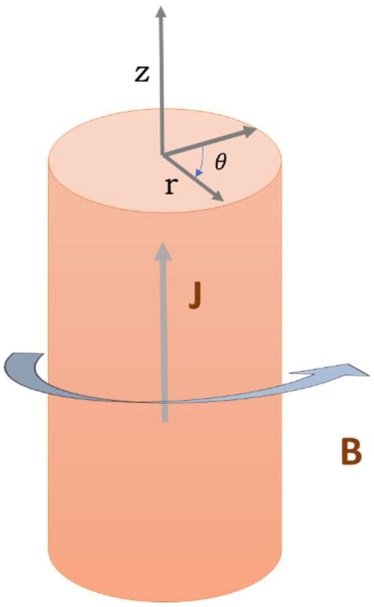

Figure 3.1: The Z-pinch in cylindrical co-ordinate: The current flows in the axial direction (Z axis) and generates a magnetic field in azimuthal direction. The Lorentz force is in the radially inward direction toward the center.

The first term in the bracket describes the particle pressure and the second term represents magnetic pressure. The last term corresponds to the induced tension force due to the curved magnetic field lines. This equation is called Z-pinch pressure balance equation.

DPF is an example of Z-pinch device used for compressing and heating the plasma within a short lifetime (50-100 ns). The pinch plasma column appears as a point at the end-on view. The electrodynamics of plasma physics can be numerically simulated with a code developed by Lee (snowplow and slug models) [120]. The snowplow model traces the axial path and slug model computes radial dynamics. It assumes a pinching plasma generated between the supersonic wave by the current and magnetic piston. This Lee model has been used to optimize the device and to predict the plasma parameters.

3.2 Dense Plasma Focus Dynamics

DPF is a coaxial gun [121,122] consisting of a central cylindrical anode surrounded by outer cathodes, usually formed by a few rods on a circle resembling a squirrel cage. These electrodes are made of highly conductive metals such as brass or copper. Central anode is sometimes kept hollow for either electron measurements or to reduce sputtering.

The anode base is isolated from the cathode by using a tube made of insulators such as ceramic or Pyrex glass. The cask and barrel of the gun are enclosed in a vacuum chamber. The central anode is connected to a high voltage capacitor bank (10-50 kV) through a high current switch. The positive terminal of the HV capacitor is connected to the switch, while the negative connector of the capacitor is connected to the grounded outer cathode. A high voltage power supply is used to charge the capacitor bank. A schematic diagram of the UNU/ICPT DPF is shown in Fig. 3.2.

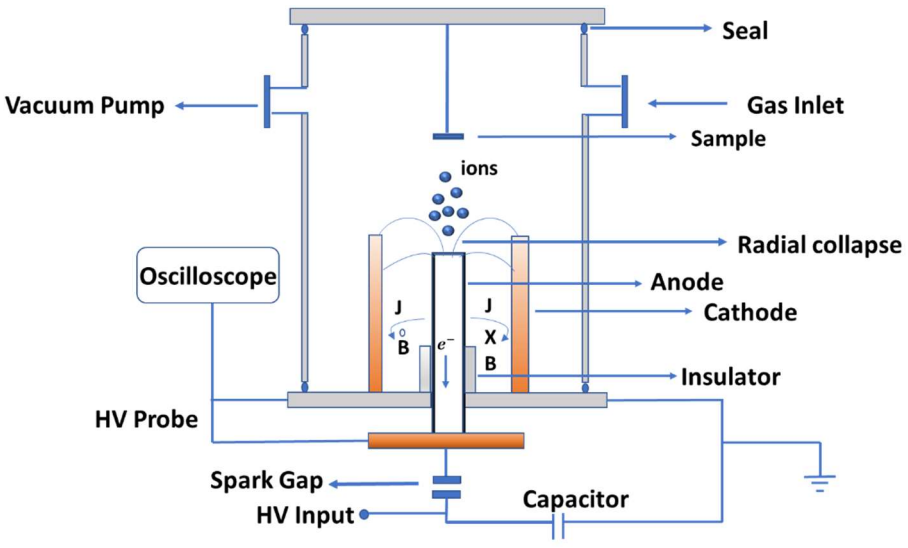

Figure 3.2: Schematic arrangement of UNU/ICPT plasma focus device used for W exposure. The umbrella-like lines represent symmetric current sheath moving in the upward direction due to Lorentz force and then compressed in the radially inward direction, pinching the plasma at center along with the emission of ions, electrons, X-rays and neutrons.

The device efficiency for energy transfer between the high voltage capacitor bank and the plasma chamber depends on the design of the transmission lines. The chamber is initially pumped to a low background pressure and then filled with a gas of choice to a desired low pressure (optimum pressure usually ranged 10-3000 Pa depending on the types of work gas). When the switch is triggered, the gas is broken down and a large discharge current is driven between the inner and outer electrodes [123].

The transfer of high current from the capacitor bank to electrodes is responsible for generation of high magnetic fields. Due to the Lorentz force, the current sheath accelerates along the barrel. Once the sheath reaches the muzzle of the gun, there is a change from the radial current to axial current, and the $\boldsymbol{J} \times \boldsymbol{B}$ force pushes the plasma in the inward direction. The compression of the plasma at the muzzle of the barrel forms a pencil-shaped dense plasma. This pinched hot and dense plasma is of the order of a few centimeters in length extended along the axis of the device. The number of electrons and ions remains unchanged, and thus a drop in the number density can be observed as the pinch elongates. An increase in the plasma inductance generates an electric field which is combined with the resistive voltage drop. The electric force accelerates electrons and ions in the opposite directions, forward for ions and backwards for electrons [124]. In addition, acceleration of electrons and ions under the influence of electric field generates an axial ionization waves which overtake the axial shock waves. Bombardment of electrons on the inner anode surface produces hard X-ray. The anode impurity material sputtered enters the plasma and produces hard X-rays (HX). If fusion occurs using Deuterium as working gas, neutrons are also emitted. It should be noted also that the sausage and kink instabilities is often developed in the pinch.

The dynamics of the DPF operation can be described by the following consecutive phases: breakdown, axial rundown and radial compression phases. Each of the phases will be described in the following Sub-sections:

3.2.1 The Breakdown Phase

When a pulse of high voltage is applied between the coaxial electrodes of the focus device. The initiation of a high current discharge depends on the configuration of the electrodes, initial gas conditions, insulating sleeve and the polarity. Under optimized conditions a gliding discharge will

initiate along the insulator sleeve. The breakdown effect can be explained based on the phenomenon of the surface capacitance. The free charges move towards the insulator and the surface of the electrode under the influence of the image forces. Free electrons on the insulator surface tends to create negative potential. Before the breakdown phase, a time delay of some tens of nanoseconds can be noticed after applying the high voltage [125]. Electrons are created due to ionization of the gas and from the metallic edges via field emission. The initial break down current is in the $-\boldsymbol{z}$ direction from the anode to the anode base. The upwards current through the inner anode induces an azimuthal magnetic field. The current sheath should be axially symmetric due to the symmetric design of the system. The radially outwards $\boldsymbol{J}_z \times \boldsymbol{B}_\theta$ force pushes the sheath to the outer cylindrical cathode, forming an umbrella-like current sheath extending from the anode to cathode. Upward force component $\boldsymbol{J}_r \times \boldsymbol{B}_\theta$ causes the plasma to travel along the upward axial direction leading to the next axial rundown phase.

3.2.2 Axial Rundown Phase

This phase represents the movement of plasma sheath along the axis parallel to the electrodes towards the open end of the electrodes. The establishment of the dense and hot plasma pinch mainly depends on the following two factors:

1. The profile and the structure of the plasma sheath.
2. The design of the DPF devise and the choice of the discharge conditions that make sure that the plasma sheath arrives at the end of the electrodes at or near the first maxima of the discharge current to maximize the radial compression described in the next Sub-section.

Low pressure of the working gas and the large discharge current accelerates the plasma sheath in the forward direction to the supersonic speed. This heat and compresses the neutral working gas in front of the sheath. Thus, the sheath attains a complicated structure which consists of a hot and compressed neutral layer followed by an ionized plasma layer. The pattern of this complex sheath determines the structure of current. If it is uniform enough, then the current will be azimuthally symmetric and uniform as well. Within the inter-electrode region, the magnetic field is inversely proportional to the radial distance. Hence, the current sheath is naturally curved due to this nonuniformity of the force in the radial direction. At the end of this phase, one end of the sheath continues to move along the outer electrode, and the inner end sweeps around the

central anode. Thus, the greater portion of the plasma accumulates in axial direction, and only a small fraction of the plasma contributes to the final focus.

3.2.3 Radial Phase

The plasma sheath will eventually arrive at the end of inner electrode and extend in the axial direction. Depending upon the characteristics of the DPF, the current sheath that sweeps around the anode finally collapses due to inward radial force. This phenomenon is like the Z-pinch; however, the compressing effect occurs more rapidly along with the great plasma heating. These three phases are represented in Fig. 3.3. In diagram, the pinch device is rotated 90^{o} to correlate the voltage waveform below it.

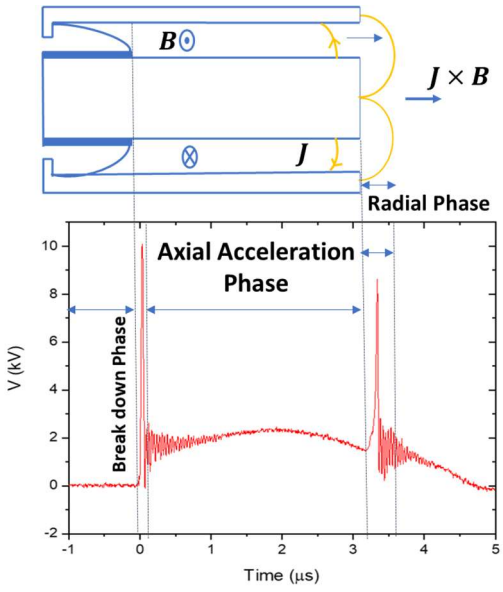

Figure 3.3: Plasma sheath dynamics in DPF and the corresponding voltage signal waveform (red) representing the breakdown, axial accelerating and radial phase of the discharge.

The radial phase can be divided into four subphases, Compression, Quiescent, Unstable and Decay phases to be discussed below.

a) Compression phase

Once the sheath sweeps around the end of the anode, it is radially collapsed with the azimuthal symmetry and attains a funnel-like profile. Shock heating is the main heating phenomenon before sheath collapse along the z-axis. When plasma sheath is transformed into a plasma column, Joule heating occurs and becomes the main heating mechanism [126]. This plasma column is adiabatically compressed to the final plasma focus. The magnetic field gets completely diffused and results in an anomalous plasma impedance [127]. While it reduces the radius, the inductance increases rapidly. The dip in the current signal and the spike in the voltage signal is due to the increase in the plasma impedance.

b) Quiescent Phase

Once the inner thermal pressures increase due to heating to balance the magnetic pressure, the DPF enters the stagnation phase. This quiescent phase marks the expansion of the pinch plasma column in both the radial and axial direction. The rate of radial expansion is hindered by the trapping magnetic field. But it can expand in axial direction due to its fountain-like geometry. Sudden change in plasma inductance induces electric field in the plasma column. Under the influence of the induced electric field, ions and electrons accelerate in opposite directions. There is an increase in relative drift velocity between ions and electrons, and later it approaches to the thermal velocity. At this phase, micro instabilities like electron cyclotron [128] start developing, and, in the end, plasma temperature rises due to ohmic heating. Due to the $m = 0$ (axial symmetric) instability plasma column gets further compressed.

c) Unstable Phase

This stage is responsible for the emission of fast ions and electrons, soft and hard X-rays, and neutrons from D-D reaction. The plasma density rises to 10^{19} cm^{-3}. The accelerated runway electrons bombard on the copper anode and thus add copious amounts of impurities into the plasma column. Disruption of the plasma column continues until the plasma density drops significantly.

d) Decay Phase

The decay phase is the last phase of interest, where hot and thin plasma cloud is developed as a result of plasma column disruption along with the emission of Bremsstrahlung radiation. The intensities of soft X- ray and neutron reach to their peak values shortly after the plasma column break-up.

3.3 UofS-I DPF – Recommissioning and Assembly

In the course of this research project, several DPF devices, including the UofS-I DPF at the University of Saskatchewan and the UNU/ICPT plasma focus device at NTU, have been used. The initial work was done on UofS-I DPF with the following task in mind: (a) to restarts the operation after sitting idle for a period of time, (b) to optimize the discharge condition, and (c) to learn the principle and operation of a DPF. The work at NTU was sponsored by the MITACS Globalink program which allowed the sample treatment using UNU/ICPT DPF plasma focus device and the material characterization tools to analyze the sample properties.

The UofS-I DPF device is a low-energy Mather-type plasma focus device powered by a single 4.9 μF fast discharging capacitor operated at 15-25 kV. Figure 3.4 shows the table-top UofS-I DPF device in the Plasma Physics Laboratory (PPL) at the University of Saskatchewan.

A two-stage rotary pump is used to achieve the base pressure of 0.1 Pa. A pressure gauge mounted at the top of the DPF is used to monitor the ultimate background and filling pressure. The low inductance (150 nH) storage capacitor is connected to the DPF anode and is switched using a pressurized spark gap switch. The spark gap is made up of Derlin plastic housing so that it can insulate cathodes and anode. It is placed symmetrically with cathodes to minimize the inductance of the coaxial transmission line. The transmission lines and the high voltage capacitor is housed inside a black grounded shielding box for the safety purpose and to shield electromagnetic interference. The discharge electrode system includes 12 copper cathode bars around a cylindrical center copper anode. The central anode is electrically isolated by cathode by a Pyrex sleeve [129].

A power supply along with the 100 ohm charging resistor is used for charging the capacitor bank. A manual or automatic trigger circuit is used to discharge the capacitor. The charging period of the capacitor bank is approximately 30 seconds, and the damping time is about 5 mins. This

charge/discharge cycles are controlled by a home-made timing sequence master controller. The total cycle time (charge, discharge, rest), from tens of seconds to a few minutes, can be programmed as desired. Figure 3.4 depicts a picture of the UofS-I DPF.

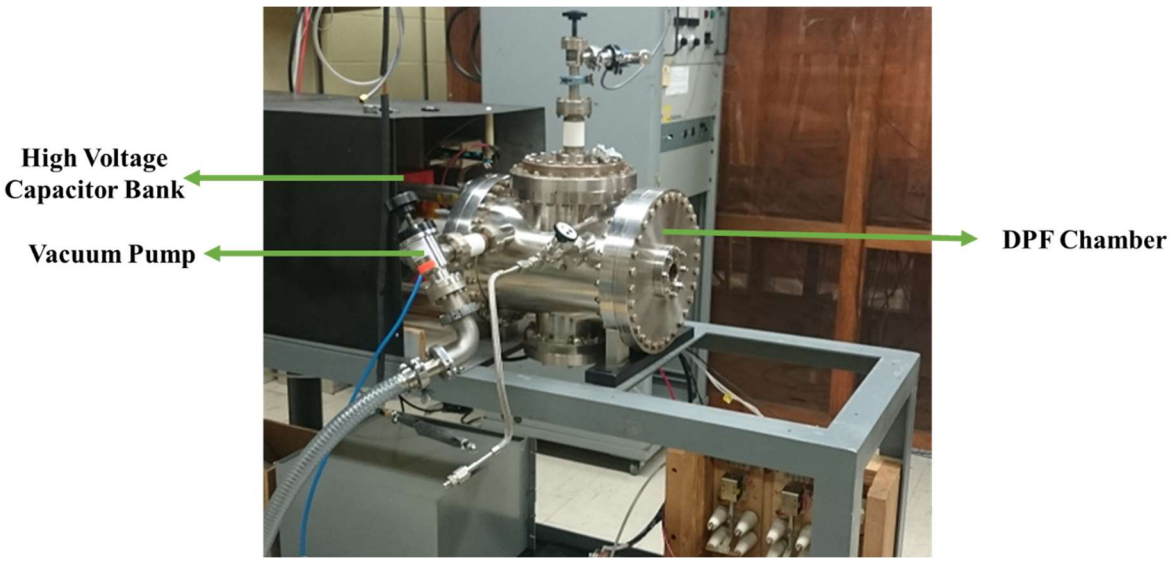

Figure 3.4: The UofS-I table-top DPF fusion device. A Faraday cage situated beside made of copper mesh to shield electrical noise when the diagnostics signals are collected.

All the diagnostics signals from the device are collected using a Tektronix oscilloscope located inside the Faraday cage made of copper mesh. It shields the Electromagnetic interference (EMI) generated due to the capacitor discharge. Copper is good conductor to shield the high frequency EMI signals and thus reduces the electronic noise.

3.3.1 Device Leakage Rate

The initial step while working with a device is 'Optimization', finding the optimal operating parameters to produce high quality focus pinch. 'Optimization' process is learnt with the UofS-I DPF device. One of the important parameters for good shot is filling pressure of the working gas in the chamber. At any operating condition, the product of the anode length and filling pressure

should be approximately the same. Considering the anode length to be constant for the device, the filling pressure for any particular operating parameter should be constant.

While working with UofS-I, it has been noted that for fixed operating parameters, existing pinch is very weak. This may be because of the unbalanced product of filling pressure and the anode length. The experiments suggested a leak in the vacuum system.

To investigate the fault, leak rate was measured. The device chamber is vacuumed with the rotary pump. Once the pressure dropped to the lowest pressure (3000 Pa), the pump was stopped, and a valve is closed to isolate the chamber from the pump. The rise in the pressure inside the chamber with respect to the time has been recorded.

The leak rate of the chamber can be defined as the fall in the chamber pressure given by,

$$L = -V\frac{dP}{dt} \tag{3.11}$$

where L is the leak rate (Pa m^3 s^{-1}), P is pressure in Pascal, V is the volume of chamber in m^3 and t is time in second [130]. Figure 3.5 represents the pressure vs time graph before and after fixing the leakage problem.

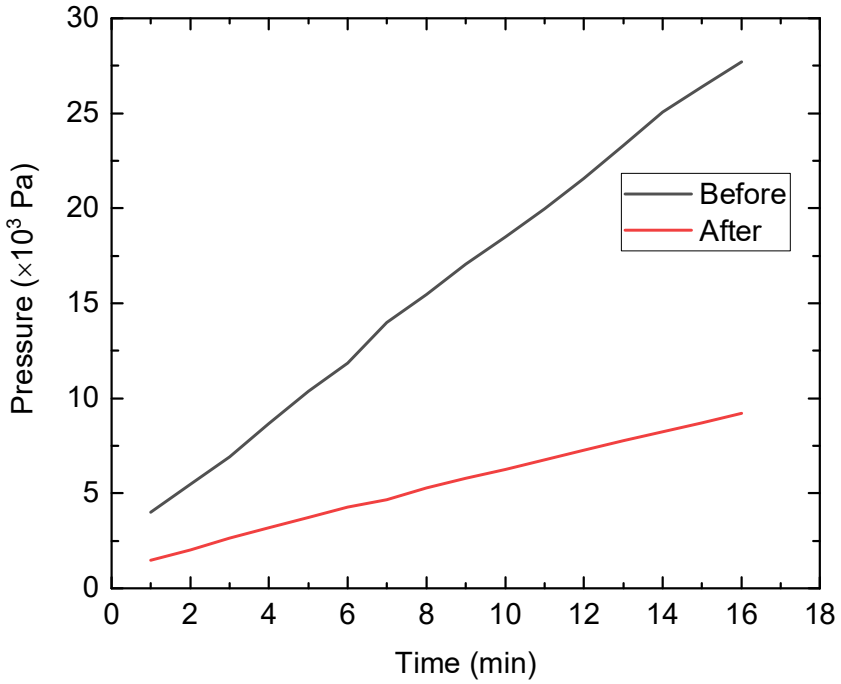

Figure 3.5: Pressure vs time graph before (black) and after (red) fixing the leakage problem in UofS-I DPF.

The leakage rate was monitored to fix the problem. While investigating the leakage reason, the O ring used as a seal around the insulating glass cylindrical was found to be faulty. The O ring was then replaced and the device was reassembled again. The leakage rate found to be reduced by 50% of its initial value (before fixation) shown in Table No. 3.1.

Table No. 3.1 Leak rate of UofS-I DPF before and after the leak O-ring replacement

Before	After
0.118 Pa m^3 s^{-1}	0.052 Pa m^3 s^{-1}

3.3.2 Spark Gap

Figure 3.6 shows the structure of the spark gap used for UofS-I DPF. It consists of a pair of electrode plates, anode and cathode, and an intermediate triggering ring between them housed in a pressurized Delrin chamber. The distance between the two electrode is 1cm. The upper part of the spark gap in the diagram is the cathode connected to the DPF discharge tube and the lower one is the anode connected to the positive terminal of the capacitor [129].

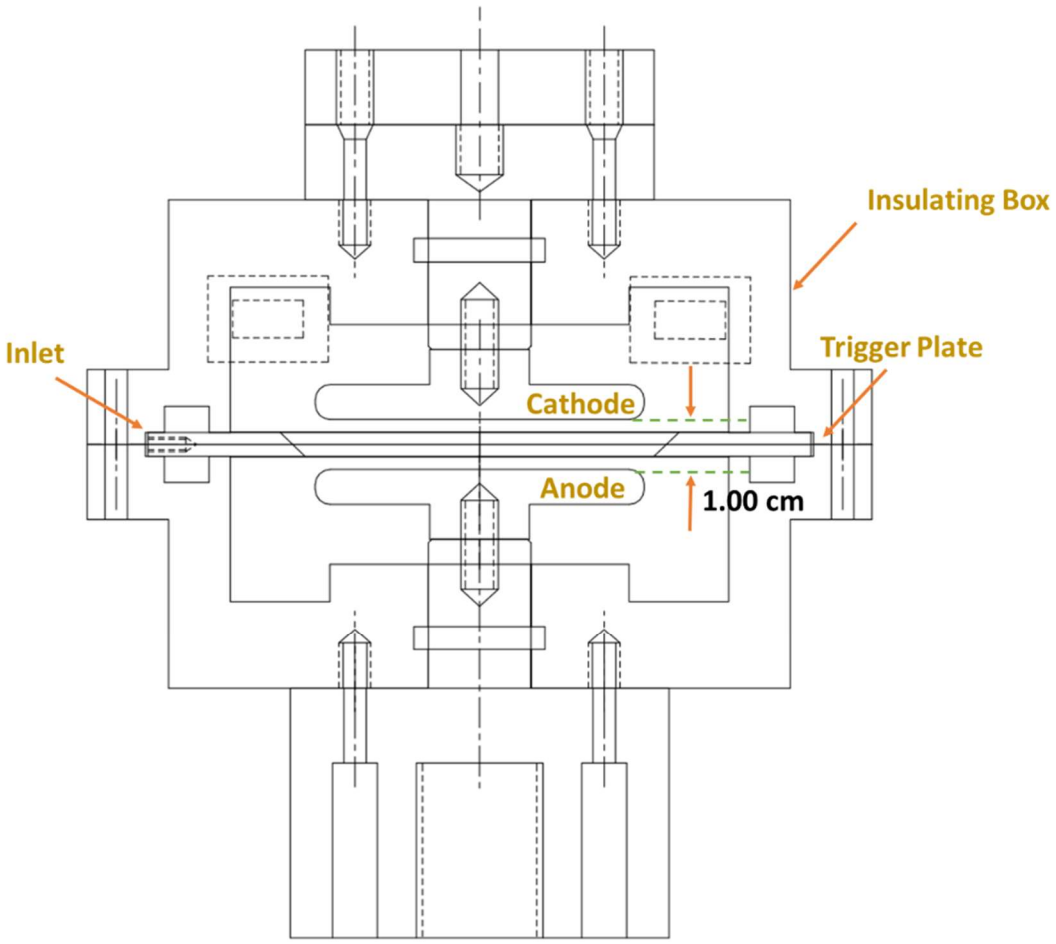

Figure 3.6 Schematic sketch of spark gap exhibiting parallel electrode arrangement and a centered trigger plate between them housed in insulating box used for UofS-I.

This transition from non-conducting to conducting state is governed by the Paschen's law. In 1889, Friedrich Paschen stated that when the ratio of the electric field strength to the gap pressure increase by its threshold value, avalanche will fill the space between the conductors with conductive fluid. The threshold voltage is the product of gap distance (d) and the pressure (p). Paschen's law can be expressed by following equation:

$$V = \frac{a(pd)}{\ln(pd)+b} \tag{3.12}$$

where a and b are the specific constants for a given gas in the chamber.

As Figure 3.7 depicted, The Paschen curve has three regions. Low and high pd regions provide the high threshold voltage. These regions referenced to the Paschen minimum can also be referred as left-hand or right-hand regions of the Paschen curve.

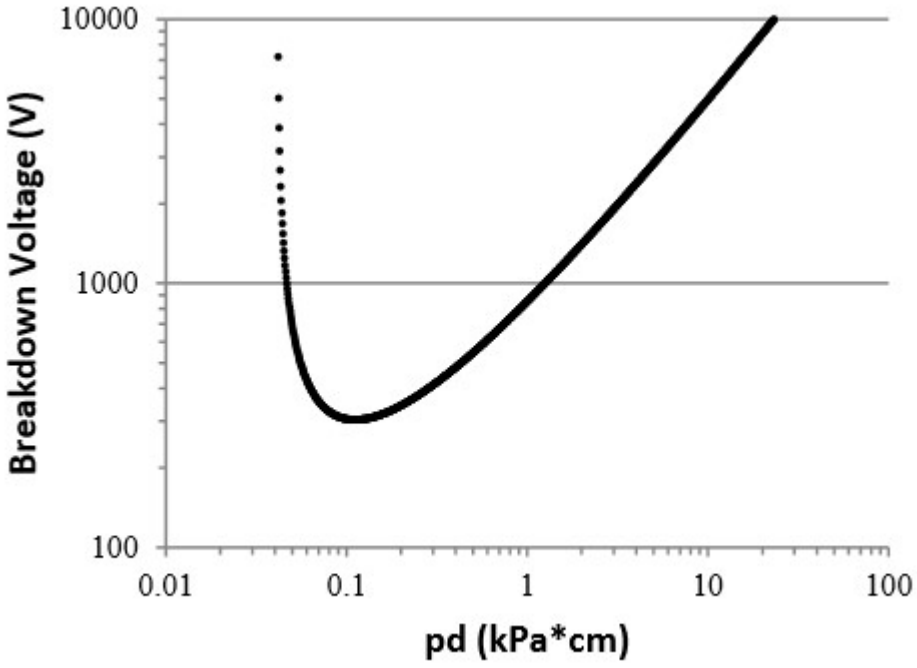

Figure 3.7 Breakdown Voltage (V) vs pd graph showing Paschen curve for air in log-log plot. [131]

In the case of triggered spark gap, the pressure is optimized to minimum value to avoid the self-trigger and to reduce the jitter. The value of the minimum pressure set by the reservoir air chamber using a pressure regulator.

Also, if the gap is too small, the time duration for the spark to travel across the conductor decreases and will not remain hot enough to ignite the plasma. Thus, the pressurized spark gaps can only be operated on the right region of the Paschen curve [131].

A spark gap acts like a switch designed to carry the current from the capacitor to DPF at certain charging voltage and to discharge the energy stored in the capacitor bank into DPF when it gets triggered by a pulse generator coupled with a fiber-optic pulse at the input and a pulse transformer at the output. The spark gap consists of two copper electrodes and a cylindrical copper plate as a trigger electrode shown in Fig. 3.6.

The spark gap is pressurized with compressed air at $(3 - 10) \times 10^4$ Pa and its pressure can be used to optimize the breakdown voltage between the electrodes of the spark gap when the trigger pulse is provided. The output of the spark gap is connected to the chamber by coaxial copper strips (transmission lines) connected in parallel. These coaxial transmission lines help to minimize the discharge noise during the device operation as well.

While working with spark gap, it was noticed that at the pressure range of $(3 - 10) \times 10^4$ Pa the spark gap was self-triggered at lower voltage (15 kV), far lower than the desired operation voltage.

To understand this problem, the spark gap of UofS-I was dissembled. The electrode was found to be tilted which decreased the gap distance and thus reduced the breakdown voltage. Moreover, the conductors were rusted due to large number of discharges as shown in Fig 3.8. Electrodes were repaired, cleaned up and re-assembled again in parallel position with the gap of 1cm.

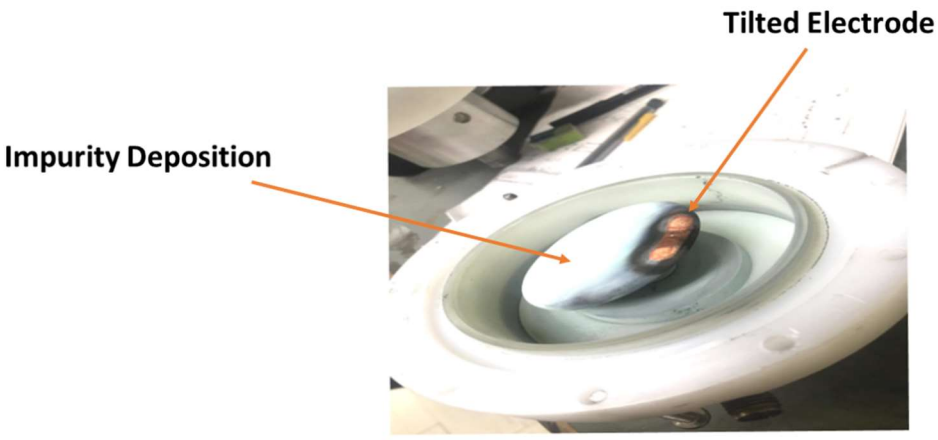

Figure 3.8 Tilted electrode with discharge depositions (impurity) in spark gap.

Chapter 4

DIAGNOSTIC TECHNIQUES

This chapter provides a short description and experimental setup of UNU/ICPT DPF. A brief explanation of the plasma and the material characterization techniques is given based on the tools used for the validation of the results.

4.1 Device Characterization

Dense plasma focus device used in this investigation is 3 kJ UNU/ICPT [111]. It is powered by a single (30 μF) fast discharging capacitor. This focus device is comprised of a 220 mm long central copper anode with a diameter of 19 mm. The anode is surrounded by six 160 mm long symmetric cathode rods. The co-axial electrode assembly is mounted in a stainless-steel chamber. 3D view of UNU/ICPT DPF is shown in Fig. 4.1.

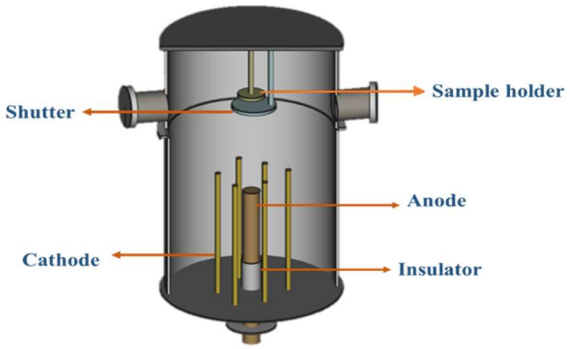

Figure: 4.1 3D view of UNU/ICPT DPF device experimental setup for irradiation of tungsten samples.

A two stage trigger circuit, composed of a low voltage Silicon Controlled Rectifier (SCR) used to trigger to a high voltage SCR, is used to trigger the swinging cascade spark gap [132]. The peak current discharge and the device inductance are 170 kA and 110 nH. The length of the insulating quartz sleeves at the breech end of the anode is 60 mm. The UNU/ICPT DPF consists of following subcomponents (See Fig 4.2)

(a) Driver - High voltage capacitor,

(b) Switch - Swinging Cascade Spark Gap,

(c) Plasma Focus Tube - Discharge chamber and coaxial electrode system,

(d) Vacuum system - Vacuum pump, manometer, working gas cylinder,

(e) Control and sync. Devices - Master pulse trigger generator, delay units and high voltage trigger unit,

(f) Diagnostic Probes - Voltage probe, Rogowski coil and Faraday cup,

(g) Digital Storage Oscilloscope (D.S.O.),

and (h) Computer Analysis system.

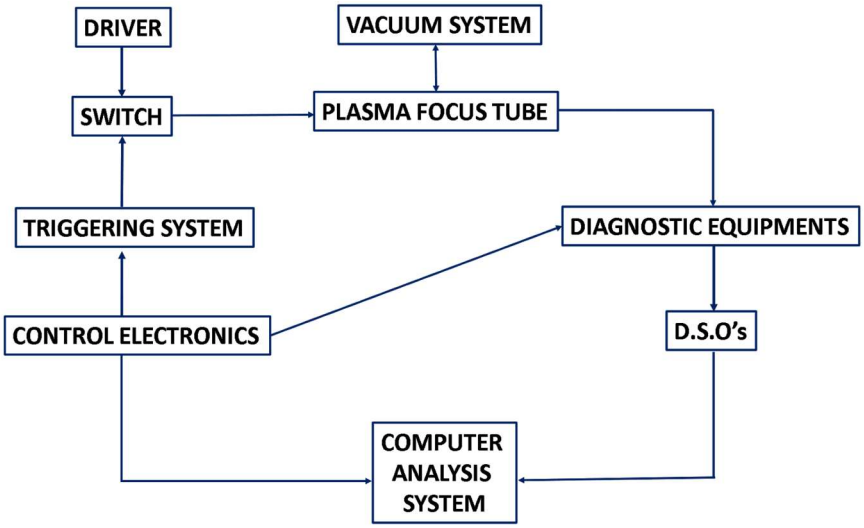

Figure 4.2: Block diagram representing UNU/ICPT plasma focus device setup.

Diagnostics of hot, short-lived and dense plasma demands a carefully designed experimental probes because the plasma behavior varies at very frequently over a large range amplitude. The

description and principles of the tools used for the investigation of the pinch parameters and ion emission are detailed in the following Subsections.

4.1.1 Voltage Probe

Voltage probe is a simple resistive voltage divider system, which is used to measure voltage across the high voltage plate of DPF and the ground of DPF. It consists of ten 510 ohms resistor and one shunt resistor of 51 ohms shown in Fig. 4.3. This attenuates voltage by a factor of 100. Resistor assembly is housed in the cylindrical hollow copper rod of 20 mm diameter. Electrical insulation between copper tube and high voltage point is done with a mylar sheet. The output signal from the voltage probe gets attenuated by 100 times. This resistive divider is further connected to the oscilloscope via an attenuation terminal [133].

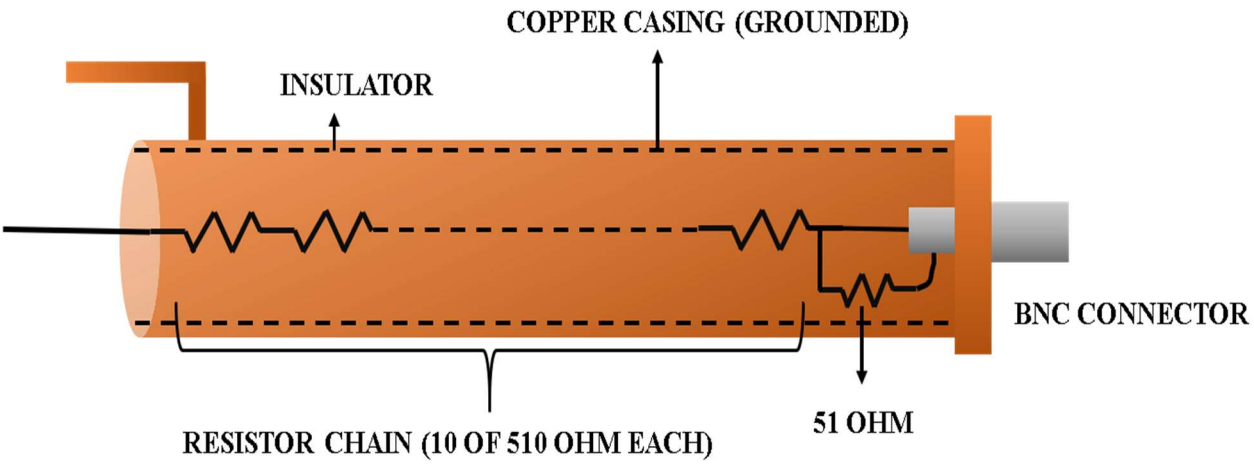

Figure 4.3: Schematic of the home-made voltage probe used to measure the voltage signals of UNU/ICPT DPF. A series of ten 510 ohms resistors and one 51 ohms resistor are enclosed in a copper tube of 50 mm diameter.

4.1.2 Rogowski Coil

It is a very well-known probe used to measure the current derivative signals. It gives information about the plasma dynamics during the axial and radial phase. Rogowski coil is a tightly wound multi-turn solenoid bent into a torus shape shown in Fig. 4.4.

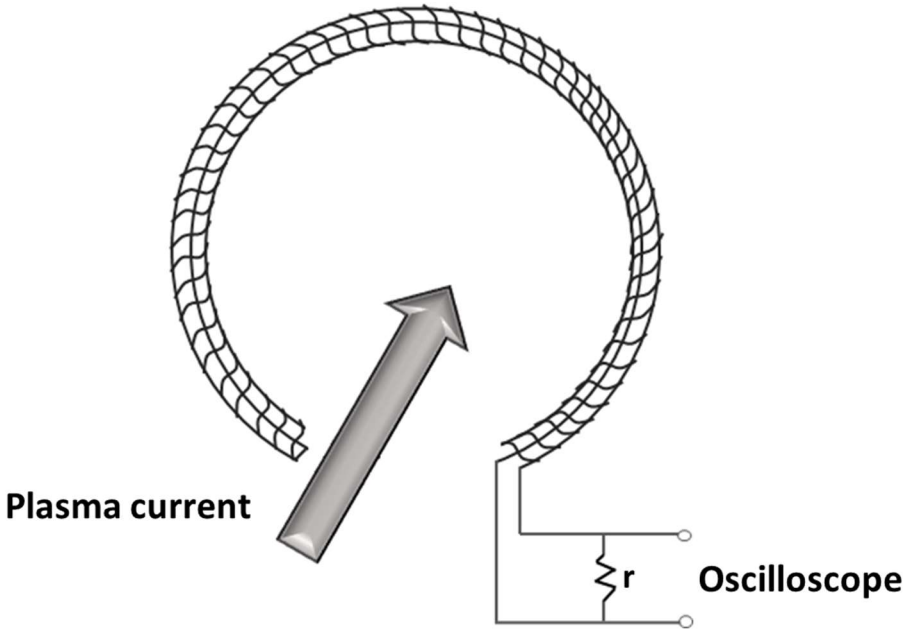

Figure 4.4: Schematic of Rogowski coil placed around the plasma current (grey arrow) used for current measurement with integrating resistor of small inductance.

The equivalent circuit of the Rogowski coil can be considered an inductor of L_c and a resistor r_c connected in series and then connected to the external termination resistor r, shown in Fig. 4.5.

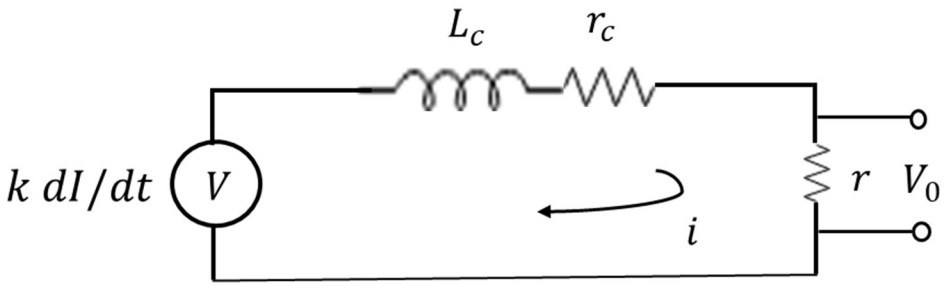

Figure 4.5: Equivalent circuit of Rogowski Coil consisting an inductor of L_c, a resistor r_c connected in series and an external termination resistor *r* added to the input signal.

If I is the discharge current to be measured and i is the current passing through the Rogowski coil then we have, based on Kirchhoff's law,

$$L_c \frac{di}{dt} + (r_c + r)i = k\frac{dI}{dt} \tag{4.1}$$

where $k\frac{dI}{dt}$ is the induced voltage by the time varying current I and the terms on the left hand side are the sum of the voltage drop through the inductor and resistors. The following two limitations are may be utilized to analyze the output voltage signal.

1. If $(r_c + r)i << L_c \frac{di}{dt}$ we get $i = \frac{k}{L_c} I$,

The output voltage becomes $V_o = r\frac{k}{L_c} I$ and the Rogowski coil works in integrating mode. The output is proportional to the I.

2. If $(r_c + r)i >> L_c \frac{di}{dt}$, we get

$$V_o = \frac{rk}{r_c + r}\frac{dI}{dt} \tag{4.2}$$

In this case, the output is proportional to dI/dt and thus, Rogowski coil works in differentiating mode. In our diagnostics, differentiating mode is used to measure the fast changes in the dynamics of device impedance [133, 134].

4.1.3 Faraday Cup

A Faraday cup is used to measure the ion beam current emitted from a plasma focus device. It consists of a small aperture of 0.25 mm radius and a 10 mm deep collector cup [46]. The structure of the Faraday cup and the external circuit are shown in Fig. 4.6.

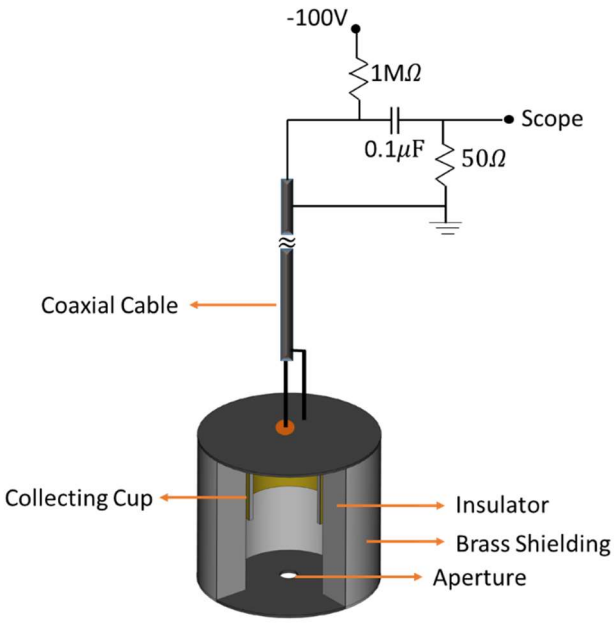

Figure 4.6: Cylindrical Ion Faraday cup schematic in reverse biased with -100 V to measure ion beam characteristics.

The physical dimensions of the Faraday cup are chosen in such a way that its impedance should match with the coaxial cable impedance (50 Ω). A simple relation is used to set the characteristic impedance to 50 Ω:

$$Z = \frac{138.2}{\sqrt{\varepsilon_r}} \log_{10}\left(\frac{D}{d}\right) \text{ ohms} \tag{4.3}$$

where, d is the outer diameter of the inner electrode (8mm), D is an inner diameter of the outer electrode (35mm) and ε_r is the dielectric constant of the isolating material (Nylon).

If the Faraday cup is to be used as an ion collector, then it should be negatively biased. In our setup, the Faraday cup collector is biased at -100 V. Negative biasing helps to remove the secondary electrons generated on the collector surface due to incoming ions. If V is the output voltage measured with Faraday cup, R is the resistance across measured signal and I is the ion beam current, the choice of the biasing voltage is chosen based on the following relation:

$$V_{bias} > V_c + V_e + V \tag{4.4}$$

where, V_e is the voltage required to repel electrons, and V_c is the voltage change on the capacitor due to the ion current source.

While working with different background gases, a thumb rule for setting the minimum negative biasing to decelerate and deflect the stray electrons is given below:

$$| V_{bias} | > \left(\frac{m_e}{m_i}\right) E_b + V \tag{4.5}$$

where E_b is the maximum ion beam energy, m_e and m_i are the electron and ion mass, respectively.

Considering this as a reference, the biasing used in this experiment is -100 V as the helium ion energy is expected up to 1MeV.

The Faraday cup is placed at 50 cm from the pinch, and thus velocity distribution can be measured with time of flight (T.O.F.) method [135]. If E is the ion energy, d is the measured distance from pinch position and $\boldsymbol{v_i}$ is the ion velocity, we get:

$$\boldsymbol{v}_i = \sqrt{\frac{2E}{m_i}} = \frac{d}{t} \tag{4.6}$$

4.2 Material Characterization

Characterization of the nanomaterials and the ion beam irradiated tungsten samples is an important aspect in my project. Material degradation and the characteristics of the nano-film will be analyzed with the characterization techniques such as (FESEM), (XRD) and hardness tests.

4.2.1 Microstructural Characterization

Compositional and microstructural characterization of the samples was done by investigating the transversal section of the samples. High resolution imaging of the microstructures on the samples was performed by FESEM equipped with X-Ray detectors (EDX) and backscattered electrons (BSE).

FESEM uses a very fine metallic tip as an electron gun to generate the electrons, drawn by series of the electromagnetic lens. The electron column is housed inside a vacuum chamber to avoid the impurities, improve the electron collection efficiency and to acquire a very high resolution. Electromagnetic lenses are simply a set of solenoids which control the path of the electrons and focus the electron beam with the help of magnetic fields. There are two types of lenses - (1) Condenser lens, used to converge the electron beam into parallel stream and (2) Objective lens, used to focus the electron beam. Electron beams are made to raster over the specimen surface with the help of scanning coils. The penetration depth of the incident electron beam depends on the atomic number of the material and the accelerating voltage. The acceleration voltage used during imaging for the W-samples in this study was 5kV that avoids the damaging of the surface structures developed after ions exposure.

A schematic diagram of the FESEM detector equipped with EDX and BSED is shown below.

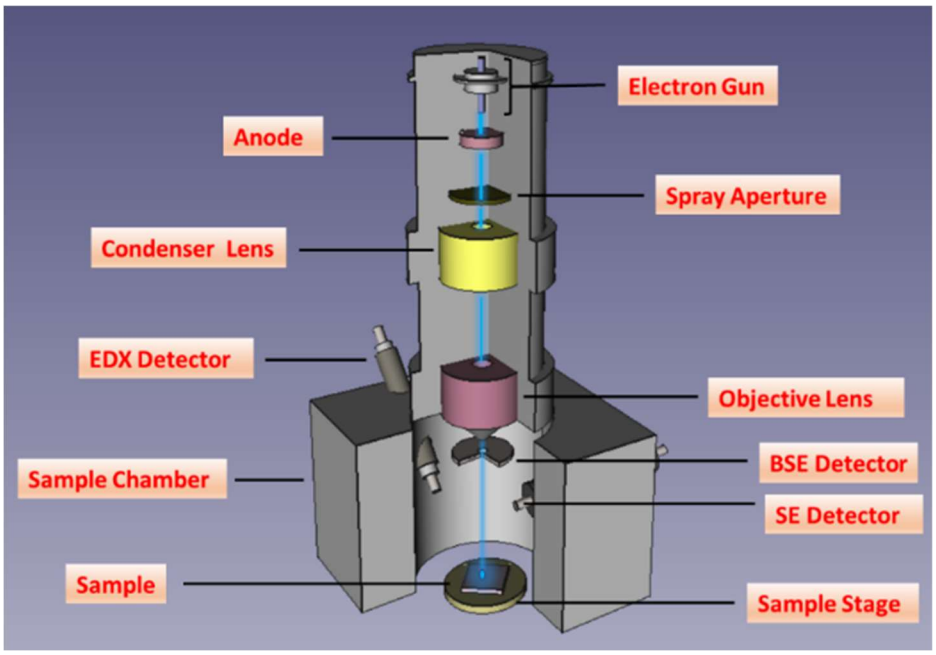

Figure 4.7: 3D representation of assembly of Scanning Electron Microscope along with Secondary Electron detector, Backscatter detector and X-ray detector used for high resolution imaging of microstructures.

Image formation depends on the signals produced during the interaction of electron beams with the specimen. These interactions are categorized into - Elastic scattering and Inelastic scattering. During elastic scattering, the electrons deflect after interacting with the sample, but its kinetic energy remains constant. The scattered electrons at the angle more than 90° are known as backscattered electrons. On the other hand, inelastic scattering may occur due to the multiple interaction between incident electrons and the atoms and the electrons of the sample. Thus, it transfers its primary energy to that atom. This excites the secondary electrons, having the energy less than 50 eV and can be used for sample imaging. Apart from these, the interaction of the

energetic electron beam with the specimen leads to the generation of some other signals like Auger electrons, cathodoluminescence, and X-rays.

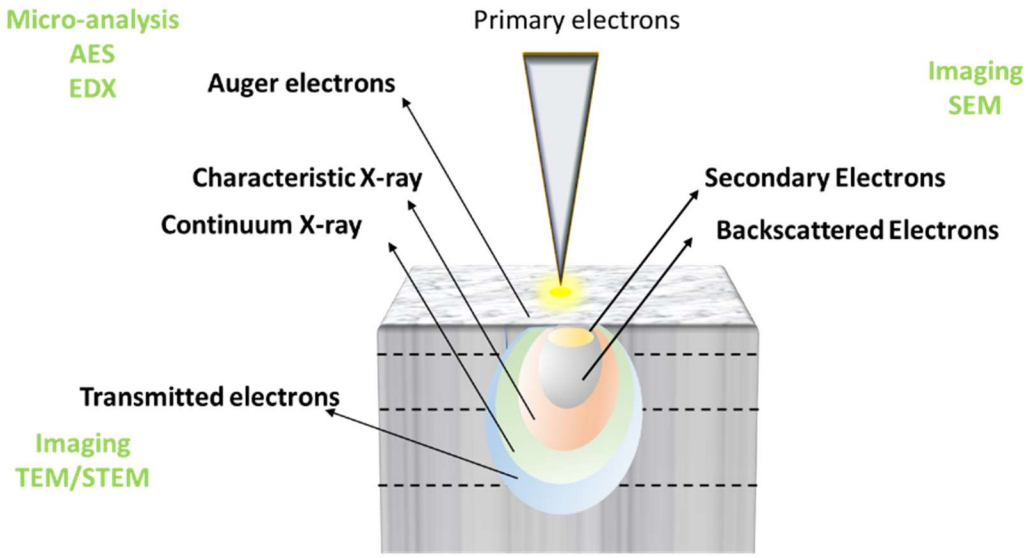

Figure 4.8: Signals generated during the interaction of high energy electron beam with the atoms within the specimen surface in a pear-shaped volume and the specimen.

a) **Scanning Electron Detector** (SED) is a useful tool for the high-resolution imaging of inelastically scattered electrons from the nearer sample surface. It consists of the scintillator layer placed inside the positively charged Faraday cage. Depending upon the number of incoming energetic electrons the scintillator gives off the photons before reaching to photocathode for signal amplification. With the increase in the working distance, the signal detection efficiency drops exponentially. SED is placed inside the electron chamber, at some angle to enhance its signal detection efficiency. SEM imaging was used as primary characterization technique to identify irradiation damage on the exposed samples. Later, the observed trends were correlated to other results obtained using other techniques to evaluate the mechanism behind the degree of irradiation-induced surface damage.

b) **Back Scattered Electron** (BSE) **detector** is a solid-state detector that collects the elastically scattered electrons after interacting with the specimen. This detector gives the compositional information based on the charge number *Z* of the elements present in the scanning area. Higher the atomic number; greater will be the positive charge and thus stronger will be the backscattered signal. Thus the "brighter" region depicts greater Z in the sample, while "darker" areas correlates to the elements with lower Z. BSEs have larger energy and thus they can give in-depth information as compared to secondary electrons. BSE images can be turned into "false color" image, which helps human eyes to differentiate between minute variation by expanding the visible hue range.

c) **Energy Dispersive X-Ray Spectroscopy** (EDXS) is a non-destructive standard technique used to identifying and quantifying elemental information on the area of interest. It is typically equipped with an FESEM device. EDXS consists of an X-ray detector mounted on the sample holder, self-cooled by liquid nitrogen dewar. The sample surface is irradiated by a highly energetic electron beam to excite the electronic structure of the atoms. Outer shell electrons replace the inner shell electron along with the emission of X-rays. X-rays emitted from exposed samples are detected by EDX detector to analyze the number of the emitted X-rays corresponding to their energies. X-ray spectra provide the fingerprints of the elemental composition. X-ray mapping provides the spatial variation of the elemental composition by sweeping the electron beam on the area.

For high-resolution imaging of microstructures on bare and exposed samples the analysis was done with a **Joel JSM 7600F High Resolution Analytical** system equipped with SED, BSE and EDX detectors. A picture of the SEM system is shown in Fig. 4.9.

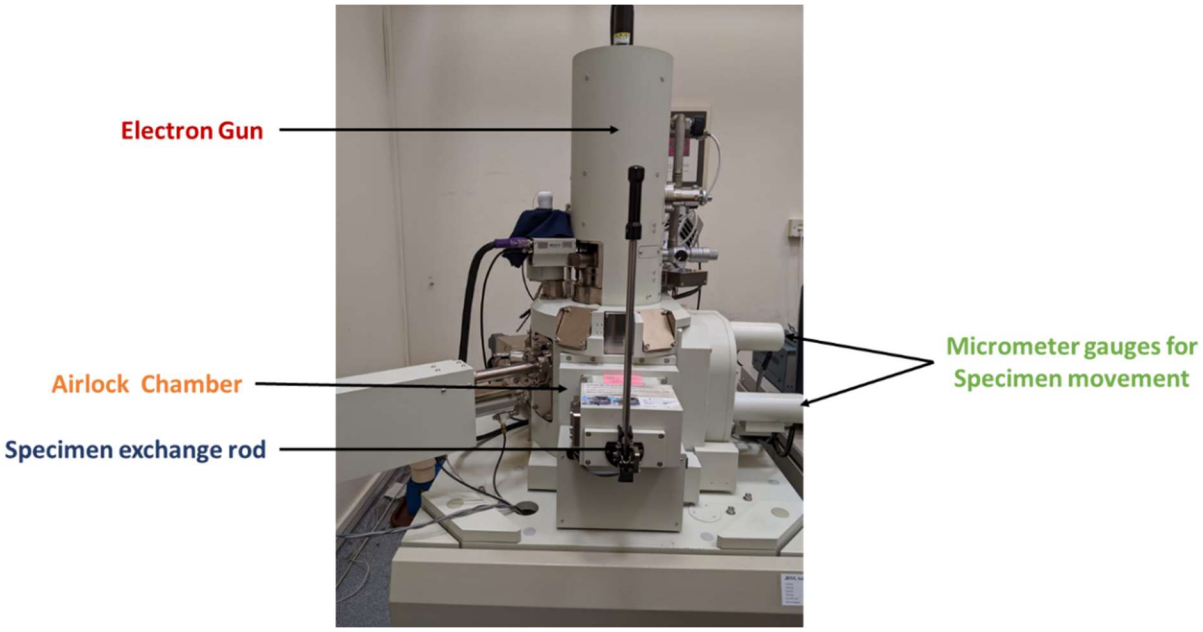

Figure 4.9: Joel JSM 7600F High Resolution Analytical SEM used for microstructural. characterization.

4.2.2 Crystal and Nano Structure Characterization

X-ray diffraction is a powerful characterization technique utilized for crystallographic and structural information of the material. Generally, Cu K-alpha source is used as a source for X-ray generation which bombard on samples. The crystallite material acts as a diffraction grating for the incident X-rays comparable to crystal plane spacing. After being interacting with electrons, X-rays get elastically scattered as shown in Fig. 4.10.

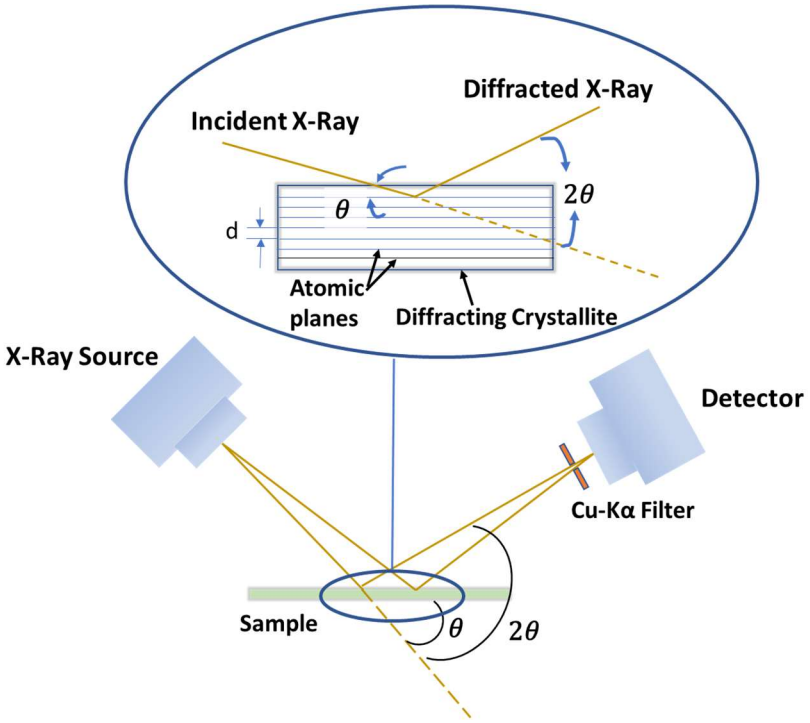

Figure 4.10: X-Ray diffractometer with sample holder in decoupled mode. The X-ray source and detector are shown with their respective angles of incidence. X-ray energy detector is also shown in the figure.

If diffracted X-rays are in phase, then they interfere constructively and gives the information of the crystal structure. The condition required for constructive diffraction is given by the Bragg law:

$$2d \sin\theta = n\lambda \tag{15}$$

where d is the interplanar spacing, θ is the diffraction angle n is the diffraction order and λ is the wavelength of the incident X-ray. XRD spectra generates the plots over the range of 2θ. The location of diffraction peak corresponding to the 2θ gives the information regarding the relative intensities of the crystallographic planes and the atomic sites within the unit cell. Figure 4.10 shows the schematic arrangement of the X-Ray diffractometer. In this thesis, the gathered XRD data was intended to analyze the strain in the lattice crystal due to He irradiation.

4.2.3 Nanomechanical Characterization

Nanoindentation tests is a ubiquitous technique used to evaluate the mechanical properties of the nanoscale material and the thin films. Unlike, micro or macro-hardness test, the nanoindentation test does not require microscopes of very high power as the area of contact is measured with the help of the indentation depth and its geometry. Moreover, it can control the depth of the indentation tip to avoid substrate effects. Although other indentation geometries like spherical, cubicle etc. can also be used for this test, the tip selected for performing nanoindentation is the standard Berkovich tip. The tip was calibrated with fused silica by performing indentations on the fused silica. The consistency of the fused silica's hardness and modulus has given confidence on the measurements taken on our samples' properties. In this study, a **KLA Tenco's Nano Indenter® G200** system was used as shown in Fig. 4.11.

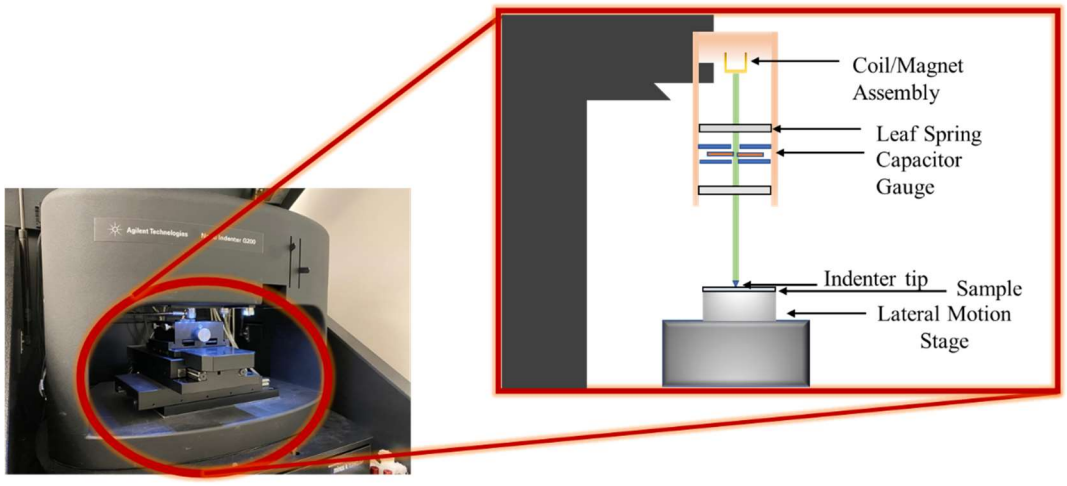

Figure 4.11: KLA Tenco's Nano Indenter® G200 system with magnified view of its three-plate capacitor schematic design. The sample is mounted on the movable stage and the signals generated by the capacitor gauge due to the conical indenter tip is recorded.

Three-sided indenter is preferred over the four-sided indenter because of the smaller area of the side faces. This reduces the friction and gives a sharp impression on the selected area of the sample. The reference and irradiated W samples were stiffly mounted onto the aluminum sample holder with adhesive wax. Before the test, all samples were placed on a sample tray for levelling and were focused under the microscope. Table 4.1 lists the key parameters used for testing W-samples under investigation in this study,

Table. 4.1: The test parameters of Nano indenter chosen for the experiments

Test Parameters	**Set Value**
Surface approach velocity	10 nm/s
Indentation depth limit	400 nm
Strain rate target	0.05/s
Harmonic displacement target	2 nm
Frequency target	2000 nm
Samples' poisson ratio	0.27

Chapter 5

RESULTS AND DISCUSSION

Double forged PLANSEE 99.7% pure tungsten samples (Poly-W and synthesized Nano-W) have been tested under the highly energetic helium ions from the DPF plasma. This Chapter begins with viability of repetitive plasma focus device as a tool for plasma-facing material testing and nano structuration of materials. The study of the anonymous surface features on the helium irradiated samples is the main goal of this thesis. A short discussion is provided on the crystallographic and mechanical properties of the exposed samples.

5.1 Poly-Tungsten Specimens

In order to understand the behaviour of the He ion irradiation, multiple specimens with the dimensions of $10 \times 10 \times 1$ mm^3, 99.97% pure tungsten were used. These double forged W tiles were provided by PLANSEE. The rest of elemental composition in the pure W specimen is given below:

Table. 5.1: The elemental specification of the sample used in this work

Element	[μg/g]
Al	1
Cr	3
Cu	1
Fe	8
K	1
Mo	12
Ni	2

Si	1
C	6
H	0
N	1
O	2
Cd	1
Pb	1

*rest is tungsten

5.2 UNU/ICPT Plasma Dynamics

The plasma dynamics of DPF can be studied using discharge current and anode voltage signals from the device. It provides the information regarding the energy delivered during the pinch phase.

Ion emission with respect to pinch gives an estimation of the damage rate of operating gases during pinch phenomenon. Figure 5.1 represents the voltage, current derivative and ion beam signal (from bottom to top) of He gas at optimum pressure of 200 Pa and 13.9 kV capacitor bank voltage. The sharp peak in the voltage signal suggests efficient focusing condition in PF device. There is a significant dip in the discharge current signal corresponding to the voltage spike. During radial pinch, there is a sharp change in the plasma inductance, which induces a strong electric field in the pinch column. Induced electric fields increase impedance anomalously, and as a result, there is a significant increase in the plasma current. There is a time delay between the emitted ion beam signal and pinch time (290 ns). Once the breakdown phase ends, a symmetric current sheath forms, marking the initiation of the axial phase. The axial rundown phase stops when the voltage signal starts rising. In UNU/ICPT DPF, the axial rundown phase continues for 1.88 μs and after that, the radial acceleration phase starts. Due to the sausage instability ($m = 0$), the plasma column disrupts, and the coupling of electric and magnetic field forces ions and electrons to travel in opposite directions.

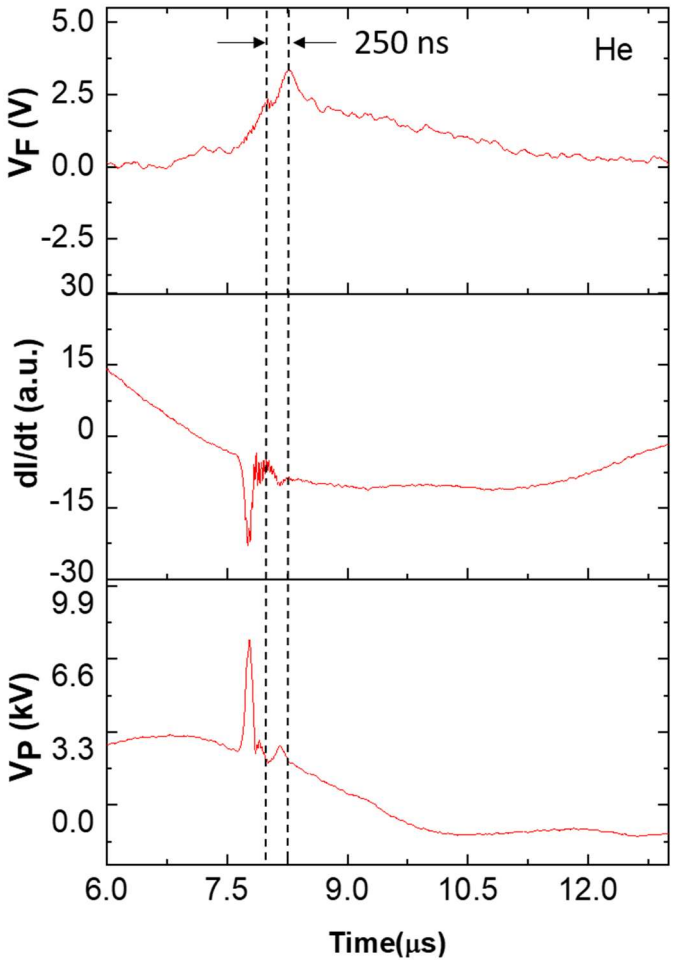

Figure 5.1: UNU/ICPT dense plasma focus device signals (bottom to top) of Helium gas plasma: Voltage signals measured with voltage probe, current derivative signal from Rogowski coil and ion beam signal from Faraday cup. The T.O.F of ion beam signal are marked with dashed vertical lines.

Similarly, Fig. 5.2 shows the voltage, current derivative and ion beam signal (from bottom to top) of Ar gas at an optimum pressure of 50 Pa (0.5). In the case of Ar gas, the time delay

between the obtained ion beam signal and pinch time is found to be 272.4 ns. This longer delay may be attributed to the higher atomic mass of the argon ions as compared to helium ions.

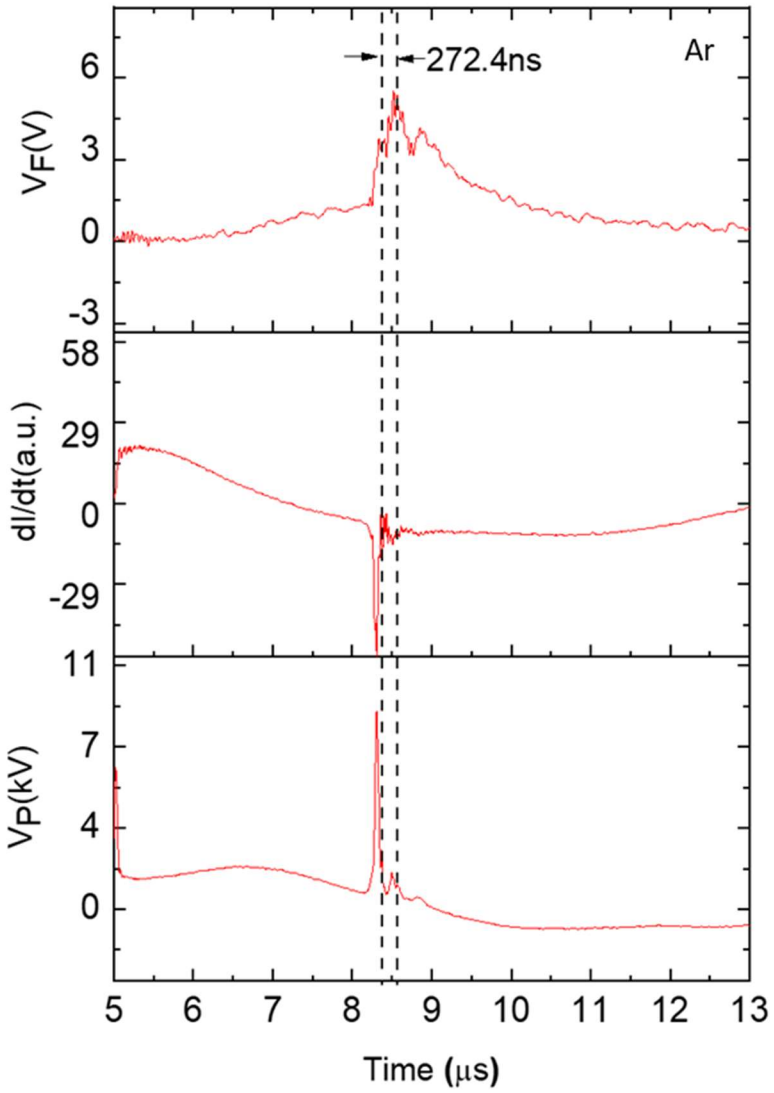

Figure 5.2: UNU/ICPT dense plasma focus device signals (bottom to top) of Argon gas plasma: Voltage signals measured with voltage probe, current derivative signal from Rogowski coil and ion beam signal from Faraday cup. The T.O.F of ion beam signal are marked with dashed vertical lines.

Faraday cup mounted at the top of the anode cup is biased at -100 V to attract the ion beam signal. Faraday cup signal shows two spikes: one with higher intensity and one of lower intensity. The first peak corresponds to X-ray or UV rays rather than ion beam signal. The energy, velocity and density of the ions can be estimated by T.O.F. method. The time of flight for ions intensity peak to reach at faraday cup is estimated with respect to X-ray spike, i.e., 250 ns as shown in Fig. 5.1 for He plasma [136].

The ion velocity v_i is the ratio of the distance travelled by ion to Time-of-Flight (T.O.F.) to Faraday cup detector. Thus, the calculated ion velocity can be used to calculate energy E (= $0.5v_i^2$) associated with incoming ions at different instant of time.

The number of ions with velocity v_i and charge e is given by

$$n_i = \frac{V}{ReAv_i} \tag{5.1}$$

where V is the Faraday cup voltage corresponding to a specific time, A is the area of the aperture and R (50 Ω) is the resistance across output signal.

The energy distribution, dN/dE vs Eshown in Fig.5.3, can be calculated based on the Faraday cup current waveform and the T.O.F. energy analyses. The following empirical law is often used:

$$\frac{dN}{dE} = \alpha E^{-x} \tag{5.2}$$

where α is a proportionality constant. The value of x should lie between 2-5 [137, 138].

The unknown parameters α and x were obtained with the help of the curve fitting tool in the Origin 2018 software. By defining the equation $\frac{dN}{dE} = C + \alpha E^{-x}$, where independent variable is E and dependent function is dN/dE, the best curve fitting was obtained $\alpha = 2.76 \times 10^{13}$ and $x = 1.75$. $C = 201.007$ corresponds to the drift of the baseline of the Faraday cup signal, either due to electronics or the background dark current. With the help of ion spectral law, ion flux J can be calculated [139, 140].

$$J = Ne\boldsymbol{v}_i \tag{5.3}$$

Experimental ion flux and ion fluence are 2.3 $\times$ 10^{28} m^{-2} s^{-1} and 4.577 $\times 10^{20}$ m^{-2} respectively.

The damage Factor (D.F.) due to ion beam bombardment can be defined is given by the following relation,

$$\text{D.F.} = Ion\ flux \times Z_{eff} \times U_{max}\tau^{0.5} \tag{5.3}$$

where, τ is the pulse duration (1.99×10^{-8} s), Z_{eff} is effective mass (2 for He) and U_{max} (13.9 kV) is the peak beam energy.

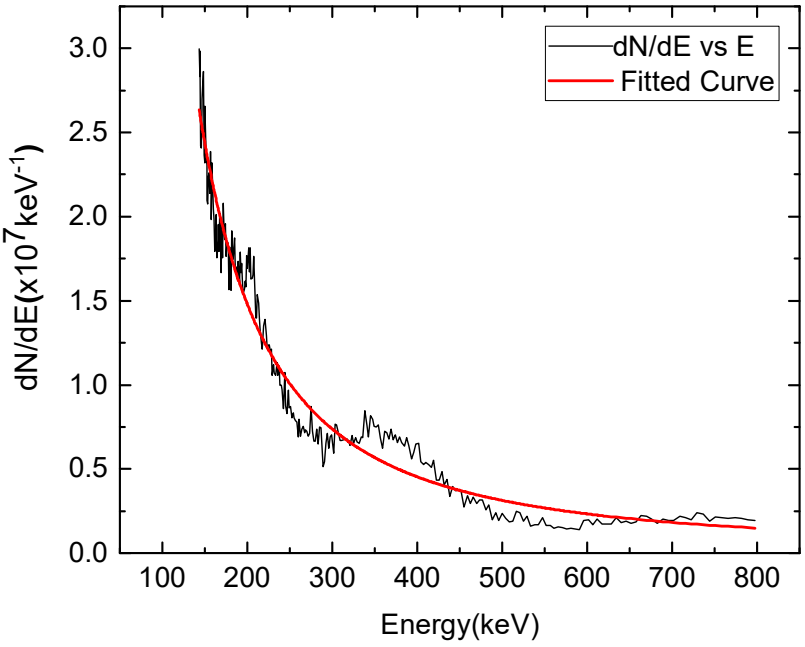

Figure 5.3: Calculated dN/dE vs E signal (Black) and the fitted curve (red) are shown in the graph. Ion energy spectra (dN/dE vs E) following power spectral law with exponent x =1.75

For He gas, calculated damage factor is 1.4×10^{10} $Wm^{-2}s^{0.5}$. In magnetically confined nuclear fusion reactors, edge localized mode (ELM) produces heat loads on the divertor. In one of the tokamak, expected power flux density Q, is 1 $MW \cdot cm^{-2}$ for a time duration of 0.1-0.5 ms [113, 141]. Thus, the damage factor is ~ Q pulse×duration (10^{10} $Wm^{-2}s^{0.5}$) is expected in ITER. The DPF devices produce ion bursts having a power flux density of higher order for a short pulse duration (ns), but also provides nearly the same D.F. as that expected in ITER. Therefore, these devices can be used to test and design plasma-facing materials that can withstand heat loads expected from ELMs in ITER.

Ion intensity as a function of pressure was investigated by operating the device at five different pressures (100-500 Pa). Figures 5.4 and 5.5 show the variation of ion beam intensity with pressure. With an increase in pressure, ion intensity increases and reaches maximum at 200 Pa and 50 Pa for He and Ar gas, respectively. After that, it subsequently decreases. Therefore, 200 Pa and 50 Pa are chosen as an optimum working pressure for He and Ar gas, respectively.

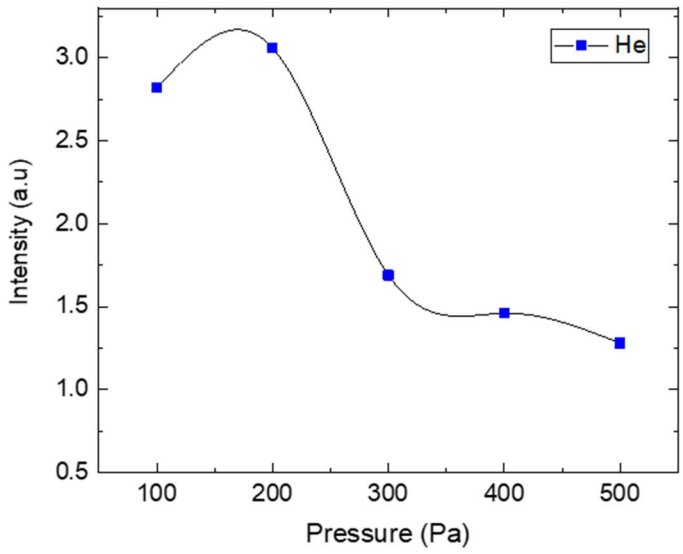

Figure 5.4 Variation of ion beam signal intensity as a function of the He gas pressure inside the DPF chamber. Ion intensity is maximum at 200 Pa He gas pressure.

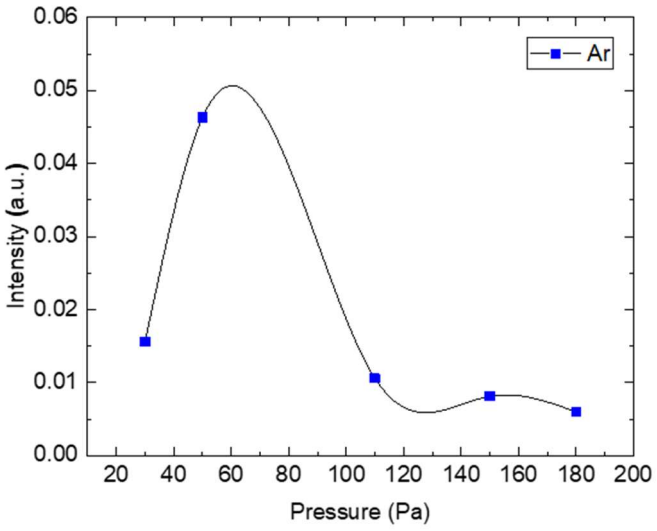

Figure 5.5: Variation of ion beam signal intensity as a function of the Ar gas pressure inside the DPF chamber. Ion intensity reaches to maximum at 50 Pa Ar gas pressure and then subsequently decreases.

5.3 Morphological Analysis Using a Scanning Electron Microscope (SEM)

5.3.1 Poly-W Exposed to Helium and Deuterium Plasma

Four samples were exposed in UNU/ICPT DPF at 7cm anode distance under the same PF working parameters at 13.9 kV and 200Pa Helium [142]. DPF was fired at 5, 10, 15 and 20 shots at the same anode distance. Reference and irradiated samples were characterized by SEM to analyze the changes in their surface morphology due to different numbers of shots.

Highly energetic He ions from the device impinged on the samples and changed the structural morphology of the exposed samples. The shiny, smooth and bright polished sample turned into a dull and uneven surface. In order to study the detailed changes in surface morphology, both reference and irradiated samples were analyzed under SEM. As evident from the micrograph

shown in Fig 5.6a, the reference W sample is quite smooth with some scratches from the mechanical polishing of the samples without any significant surface damage (cracks or blisters).

Figures 5.6 b-e show surface changes on the exposed samples at 5, 10, 15 and 20 shots, respectively. The SEM image (Fig. 5.6b) of the W sample irradiated at 5 shots shows the initiation of micro-cracks and low-density blisters on the surface. Tails, along with the blisters, represent the initiation of the bursting stage of trapped He-bubbles [143]. Few craters like structure due to bursted bubbles were noticed.

Figure 5.6c shows crack-elongation and nano-fuzz on the W sample irradiated at 10 shots. When W is exposed to He ions with impact energy lower than sputtering threshold energy, nanostructured, fluffy layer of one-micron thickness is formed. The density of nano-fuzz depends on the energy of helium ions rather than ion flux. These nanostructures affect material properties such as embrittlement, heat transfer, deuterium/tritium retention. With an increase in the number of high energy helium ions trapped beneath the surface, displacement damage increases. It has been reported that displacement damage becomes more pronounced above 10^{20} $m^{-2}s^{-1}$ion flux [144].

In Fig. 5.6d, W sample reflects various crystalline defects such, as high-density blisters, pinholes, microcracks and voids, arise due to the exposure of W by cumulative heat loads from 15 shots. Vacancies are left behind after the relocation of interstitial sites. These vacancies fuse to form voids [145, 146]. High energy He ions are trapped inside the voids to create bubbles. Bubbles get pressurized due to internal stress. The bubbles fused together and thus the number of bubbles per unit volume increased. When the surface above these highly dense bubbles is uplifted, blisters appear.

At 20 shots, there is a rearrangement of the surface topography due to excessive heat loads. Figure 5.6e confirms etching of the tungsten sample along with melted areas. Hence, damage to these materials may be controlled by the heat flux.

In nuclear fusion reactors, deuterium and tritium fuse together to give neutrons and highly energetic alpha particles. Thus, apart from the helium ions impact of neutrons and deuterium ions are also a topic of interest. Exposure of W sample was also carried out in deuterium plasma (at 400 Pa) under the otherwise the same operational parameters. Figure 5.6f shows agglomeration of nanoparticles on W surface exposed at 15 shots. At higher resolution, micro-cracks can be observed on the surface [147-149]. Thus, damage due to deuterium plasma is less pronounced

compared to the helium ions under the same working parameters of the device. Therefore, the rest of the study was carried out with helium plasma in an attempt to improve tungsten quality that can withstand high energy loads.

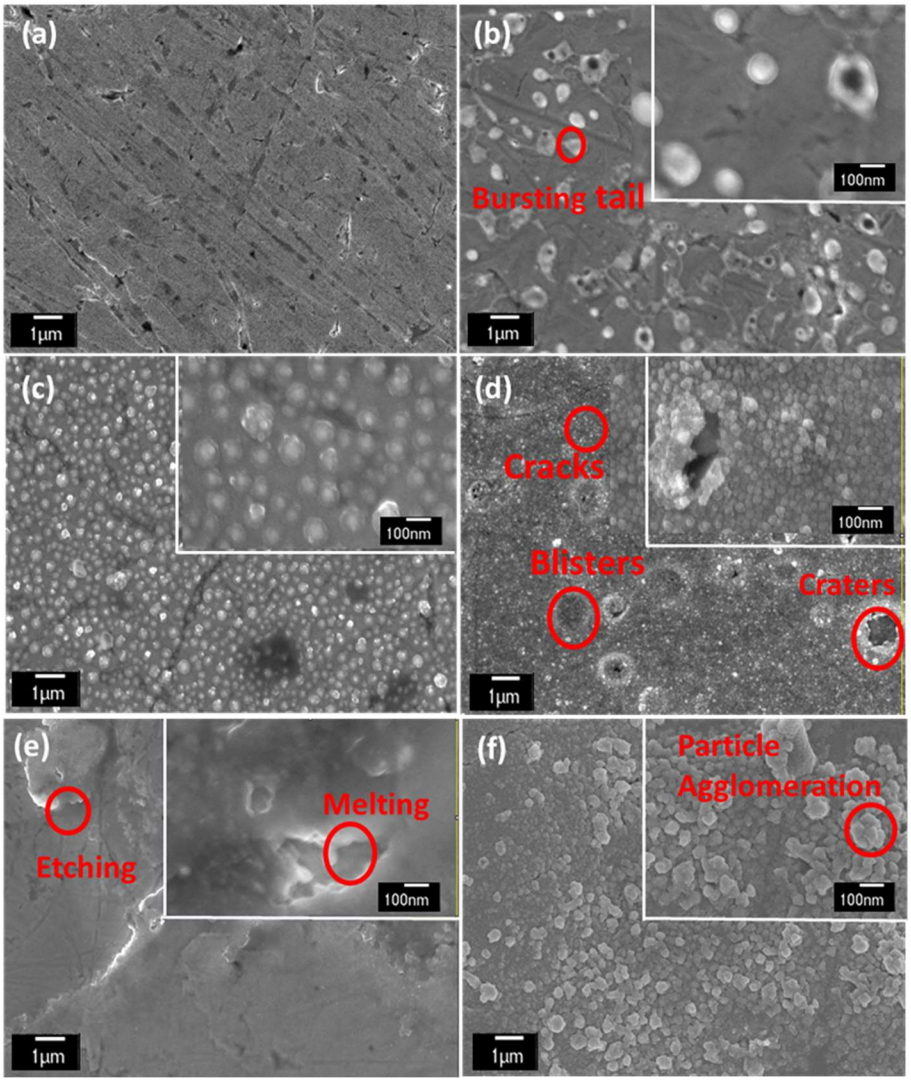

Figure 5.6: SEM micrographs of (a) unexposed W showing some scratches from the mechanical polishing, (b-c) Poly-W exposed at 5-10 shots of Helium respectively, exhibiting few blisters, fuzz and cracks, compared with sample irradiated at 15 shots (d), followed by extensive melting and surface etching sample exposed at 20 shots and (f) particle agglomeration on Poly-W exposed at 15 shots of Deuterium gas.

5.3.2 Nano-structuration of Tungsten with Argon DPF Plasma

Nano-structuration of PLANSEE double forged tungsten was done with UNU/ICPT device. The chamber was filled with Ar gas. Argon gas was chosen to avoid composite formation with tungsten [150, 151]. W samples were placed at 7 cm from the central anode. Once the base pressure of 0.1 Pa was achieved, Ar gas was introduced to obtain a working pressure of 50 Pa. Samples exposed to Ar gas were analyzed using SEM.

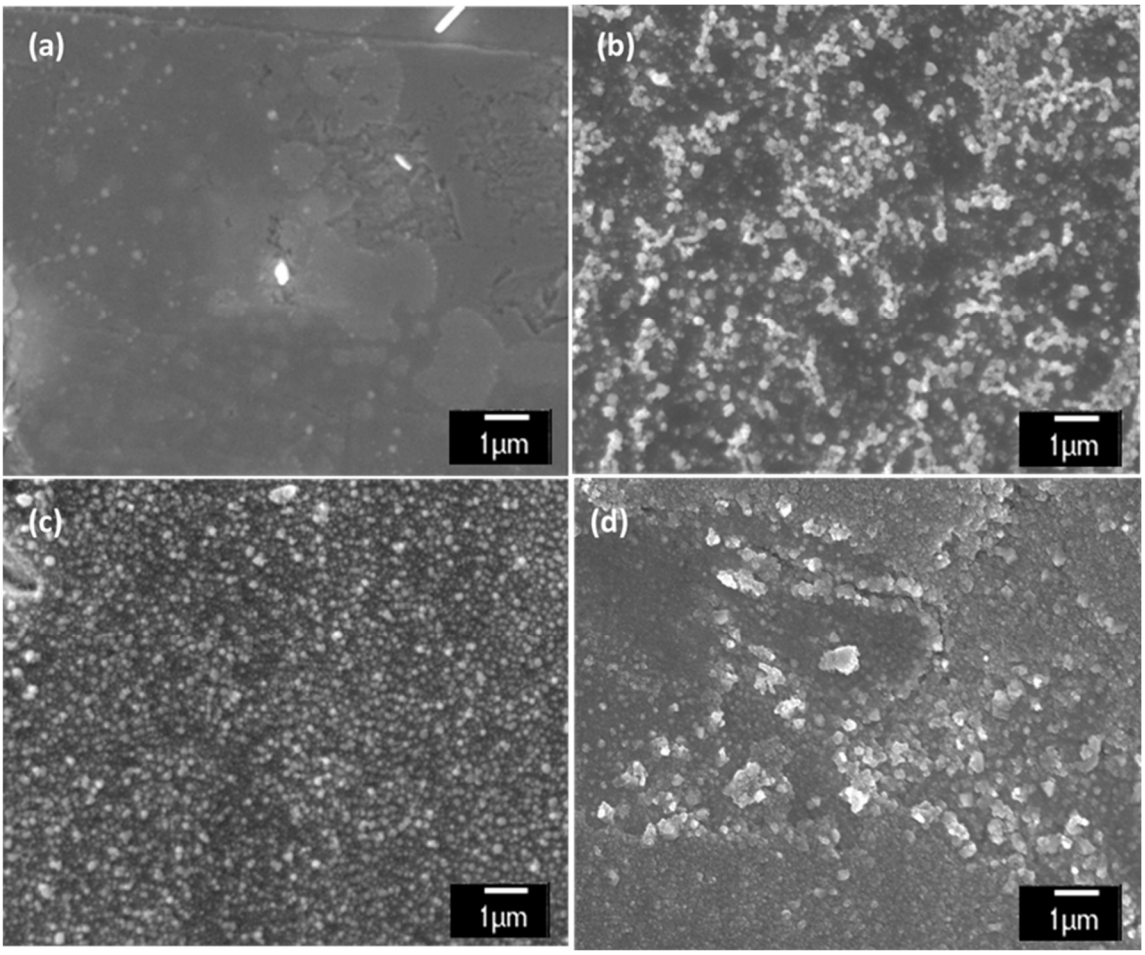

Figure 5.7: SEM micrographs of Ar irradiated W samples at different shots showing: (a) surface irregularities similar to bare W sample (5 shots), (b) bright elongated chips (8shots), (c) uniform and denser particle distribution (10 shots) and (d) particle agglomeration and cracks (15 shots)

SEM image of the irradiated sample at 5 shots (Fig. 5.7a) shows a non-uniform surface with small nanoparticles, the same as those found on the bare W samples. With an increase in the number of shots (8 shots) the nanoparticle size increased (35-60 nm). Figure 5.7b shows bright elongated chips on the exposed surface due to the low energy ion flux which is not able to fuse to form a bigger nanoparticle.

After 10 successive shots, particle size is found to be 20-55 nm. However, particle distribution became more uniform and denser, as shown in Fig. 5.7c. The nanoparticles can be seen clearly without any remarkable coalescence of the particles. After 15 shots, nanoparticles aggregate that consist of a cluster of small nanoparticles of the same or different sizes. At some part of the surface, evenly distributed nanocrystals can be seen. Figure 5.7d indicates some cracks around the grain boundaries. The agglomeration of the particles is due to the increase in the thermal effects on the irradiated sample [152, 153].

Figure 5.8 shows the particle size distribution of the Poly-W samples exposed to Ar. With an increase in number of plasma shots from 5 to 10, the density of the nanoparticles is found to be increased. After 15 shots, the particle density decreased due to the high heat loads. Thus, 10 shots are chosen to be the best-optimized condition for nano structuration of tungsten.

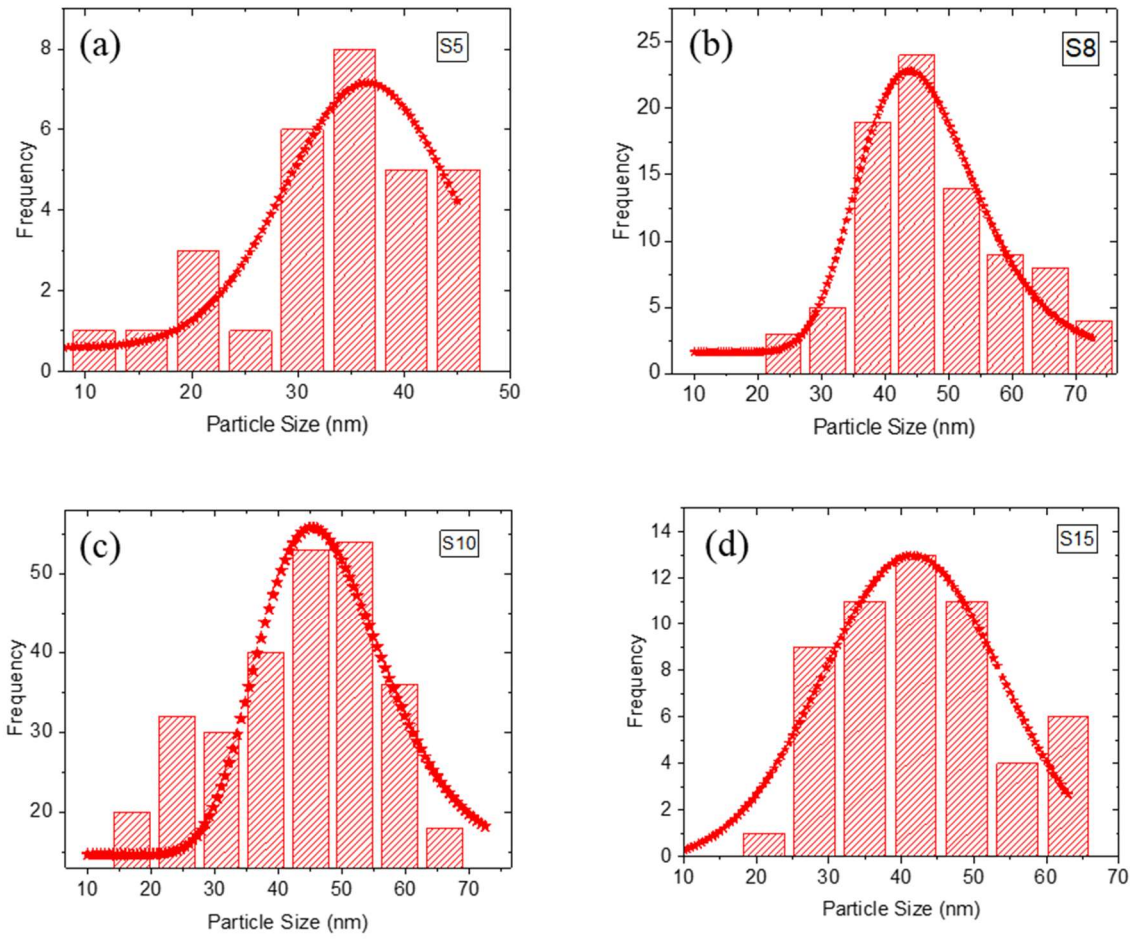

Figure 5.8: The particle size distribution of structured nanoparticles (a-d) at 5, 8, 10 and 15 focus shots of argon gas. The average particle size remained approximately constant (45-55 nm) for (a-d) and the particle density is maximum in (c).

5.3.3 Nano-W Exposed to Helium Plasma

Nano-W samples were exposed to He plasma with similar working parameters, and surface changes were studied with SEM imaging. The size of nano particles found to increased after 5 shots. No significant defect on the surface morphology of Nano-W can be found in Fig. 5.9a. However, after 10 shots, the particle size significantly increases, and small nanopores along with the grains and grain boundaries were observed [56,154]. These formation of nanopores is likely due He desorption (i.e. Helium bubble bursting).

Topological SEM images (Fig. 5.9c) of Nano-W after 15 continuous shots show nanostructure similar to cauliflower consisting of smaller nanoparticles. Grain boundaries can be clearly seen along with many nanoparticles in aggregates.

As illustrated in Figs. 5.9d-e, micro-cracks, along with some nano-globules, have been observed. The formation of these nano-globules is likely the result of the reduction of the surface heat deposition, coming from the ion beams, around the cracks. Further increase in the number of shots (20 shots) results in large size cauliflower-like structure along with the re-solidification of the surface [155].

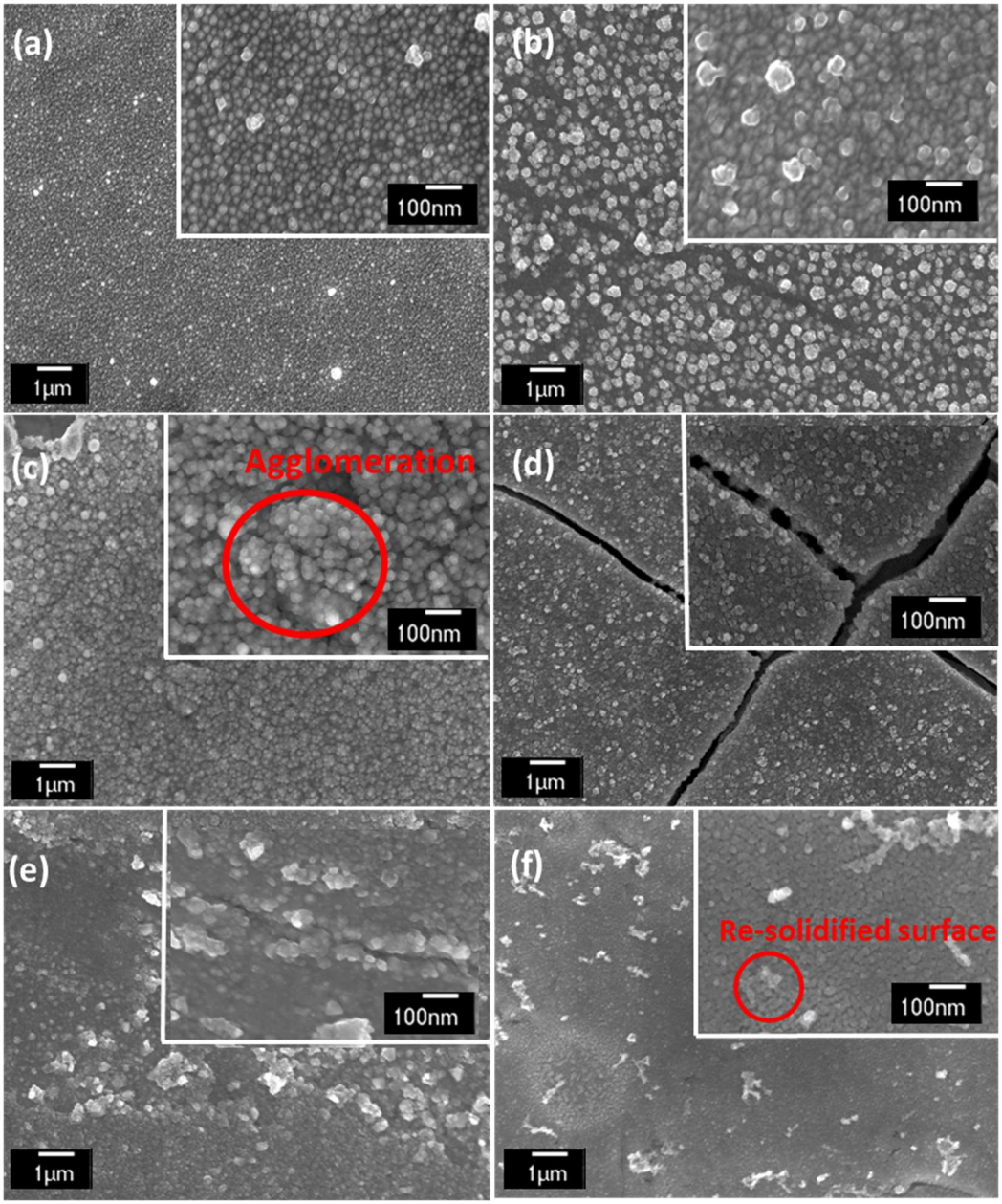

Figure 5.9: SEM micrographs of He exposed Nano-W reflecting: (a-b) dense nano particle distribution at 5 and 10 shots respectively, (c-e) surface damage features like agglomeration, cracks, sputtering at 15 shots and (f) re-solidification of the surface after 20 consecutive shots.

5.4 Compositional Analysis Using EDX

Elemental analysis of the unexposed, exposed Poly-W and Nano-W at 15 shots were carried out using dispersive energy X-ray (EDX) spectroscopy. Figure 5.10 reveals the presence of impurities (Fe, Cu, C, O). C and O were present on the bare-W as surface impurities.

Figures 5.11-12 show the content of C and O impurities increased on the exposed Poly-W and Nano-W samples. Cu impurity is visible due to sputtering of the central electrode. A higher percentage of Cu in the exposed Nano-W was expected as a PF device with the same anode arrangement was used for nano-structuration [111,118,156]. However, EDX does not detect the lighter elements (Helium).

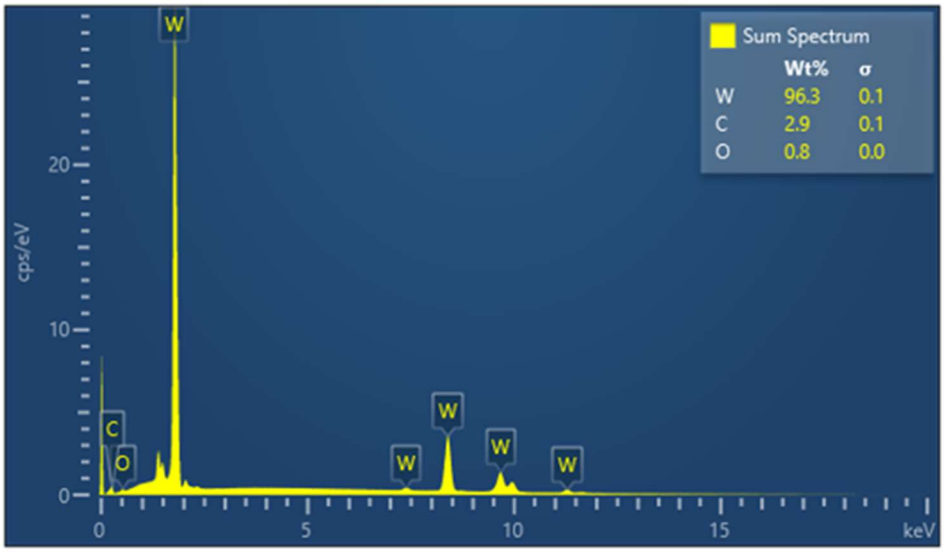

Figure 5.10: EDX spectra of Bare-W showing composition of minor impurities (O, C) on the sample.

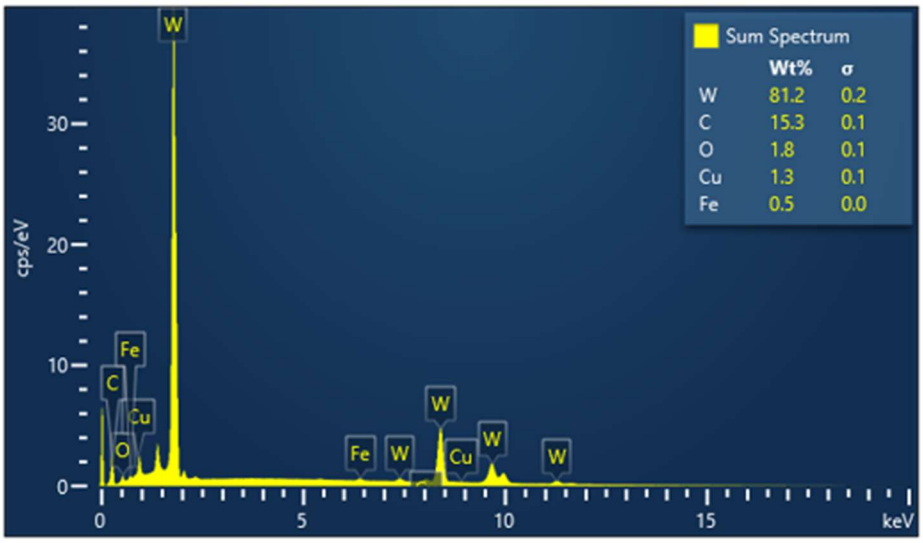

Figure 5.11: EDX spectra of Poly-W acknowledging the presence Cu (1.3%) deposition from anode sputtering.

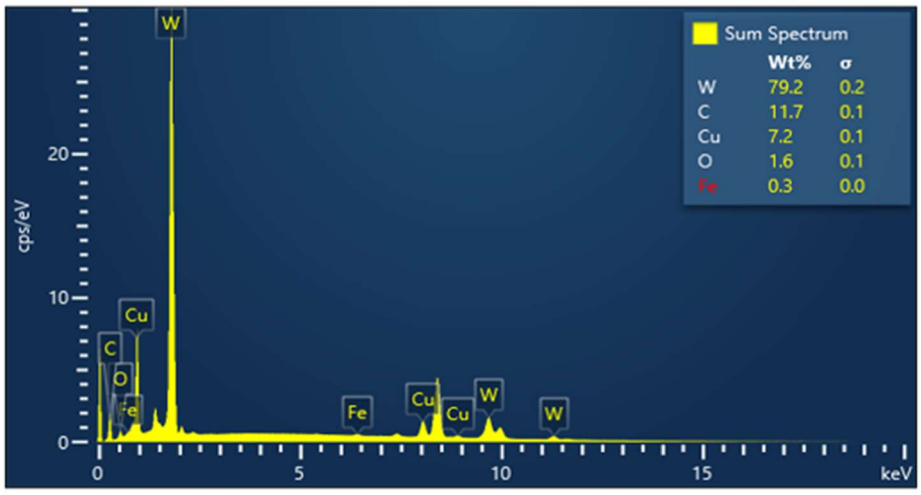

Figure 5.12: EDX spectra of Nano-W reflecting the presence of Cu (7.2%) deposition from anode sputtering.

5.5 Topography Analysis Using Back-Scattering Electrons (BSE) Spectroscopy

BSE imaging gives the information based on Z contrast. High Z elements scatter more electrons and thus seems to be brighter. Figures 5.13-14 show the BSE image of Poly-W and Nano-W exposed to 15 shots. Green and red portion reflects high Z and low Z elements, respectively. Figure 5.13 shows some circular red patches on the Poly-W. These patches correspond to the nano-fuzz observed in SEM image.

This gives evidence of trapped low Z element (He) and blisters corresponding to bubbles in the subsurface region. Similar red patches were observed in Nano-W as well. However, the density of the circular patches is comparatively smaller and gives evidence of He trapping in nanocrystals and grain boundaries instead of bubbles in subsurface.

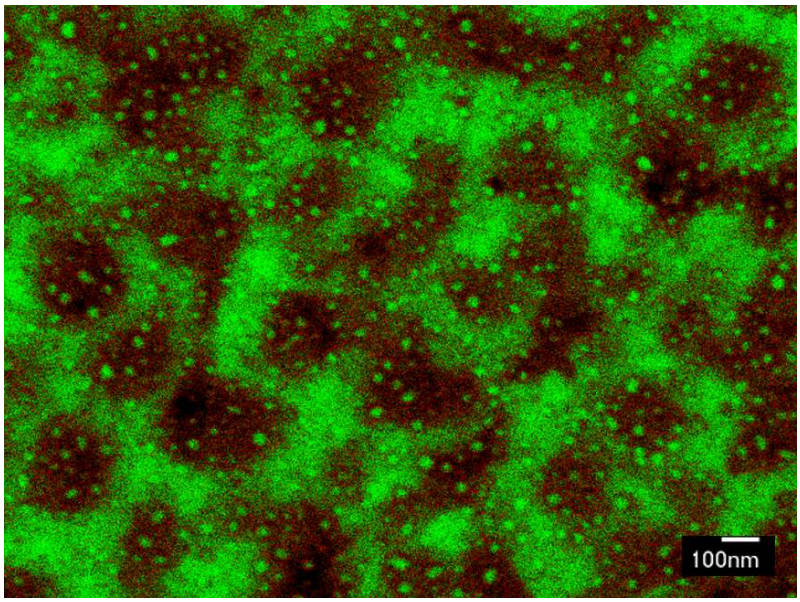

Figure 5.13: BSE image of Poly-W irradiated at 15 shots in He plasma showing mapping of high Z (green) and low Z element (red).

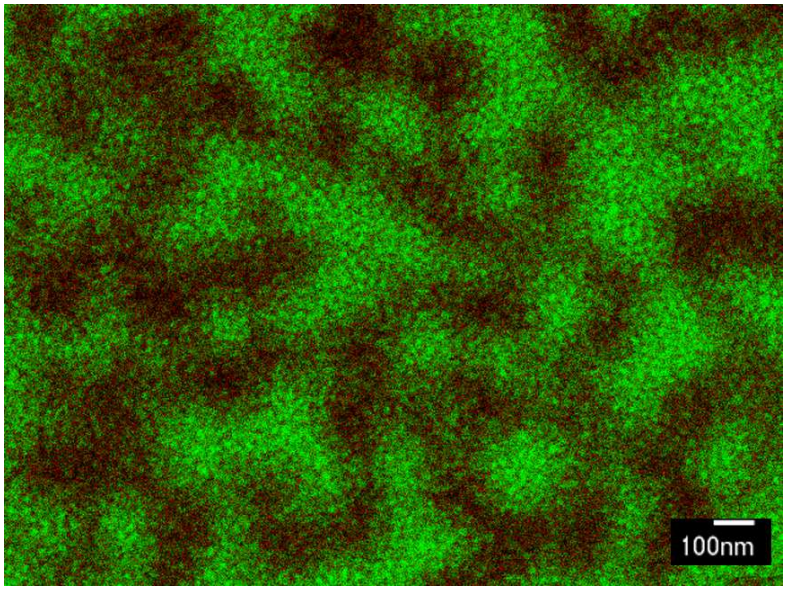

Figure 5.14: BSE image of Nano-W irradiated at 15 shots in He plasma showing mapping of high Z (green) and low Z element (red).

The processes causing the phenomena observed on the Poly-W and Nano-W samples after being irradiated by ion beam from the DPF device can be summarized in a cartoon shown in Fig. 5.15. Understanding those processes is very important in the path of finding suitable PFMs for nuclear fusion reactors.

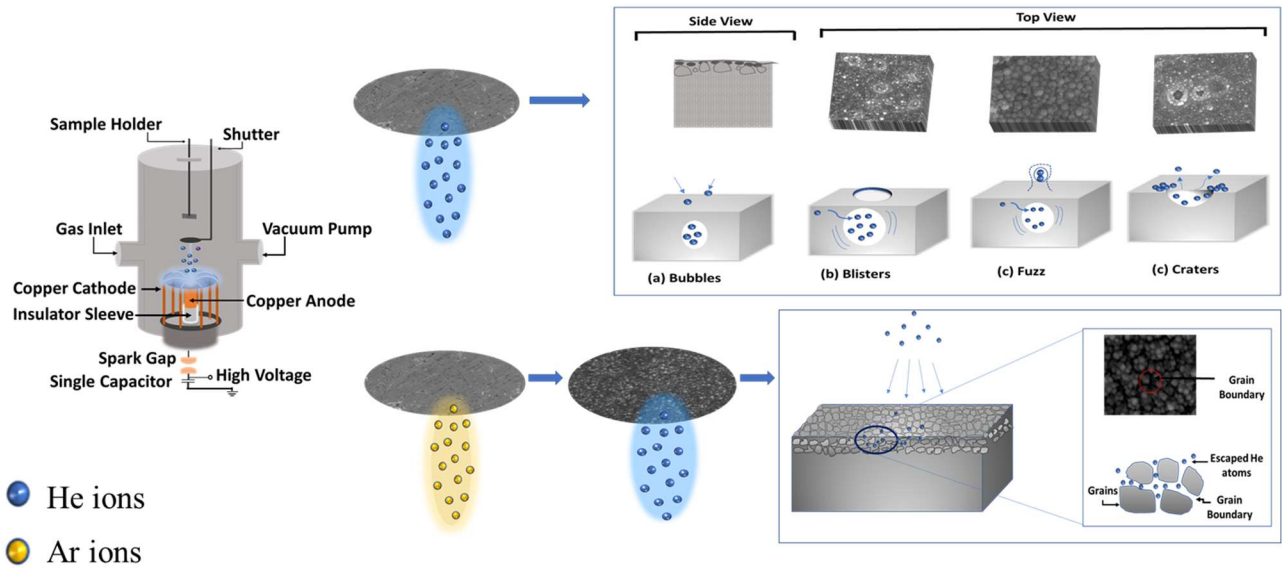

Figure 5.15: Summary of applied technique used for damage study of Poly-W and Nano-W with UNU/ICPT DPF device and corresponding SEM micrographs representing surface changes.

5.6Crystallography Analyses Using XRD

To study the changes in the crystal structure, reference sample, Poly-W and Nano-W exposed at 5, 10,15 and 20 shots (S5, S10, S15 and S20 respectively) were analyzed using X-ray diffraction (XRD) technique.

XRD patterns were analyzed in the 2θ angle range 20°- 80° at a scan rate of 0.01° shown in Fig. 5.16 and 5.17. The results in Fig. 5.17 shows (110), (200) and (211) diffraction peaks corresponding to 40.15°, 58.14° and 73.01°.

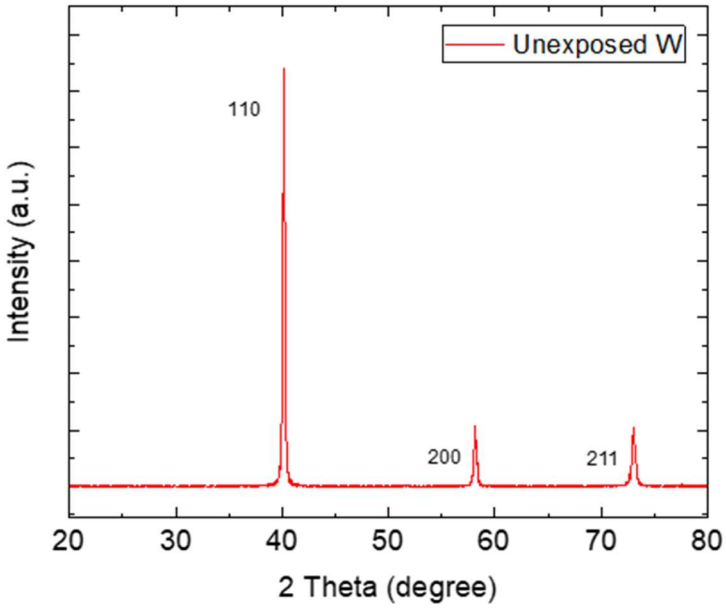

.

Figure 5.16: XRD spectra of unexposed W showing BCC crystal structure having (101), (200) and (211) planes at 40.15°, 58.14° and 73.01°.

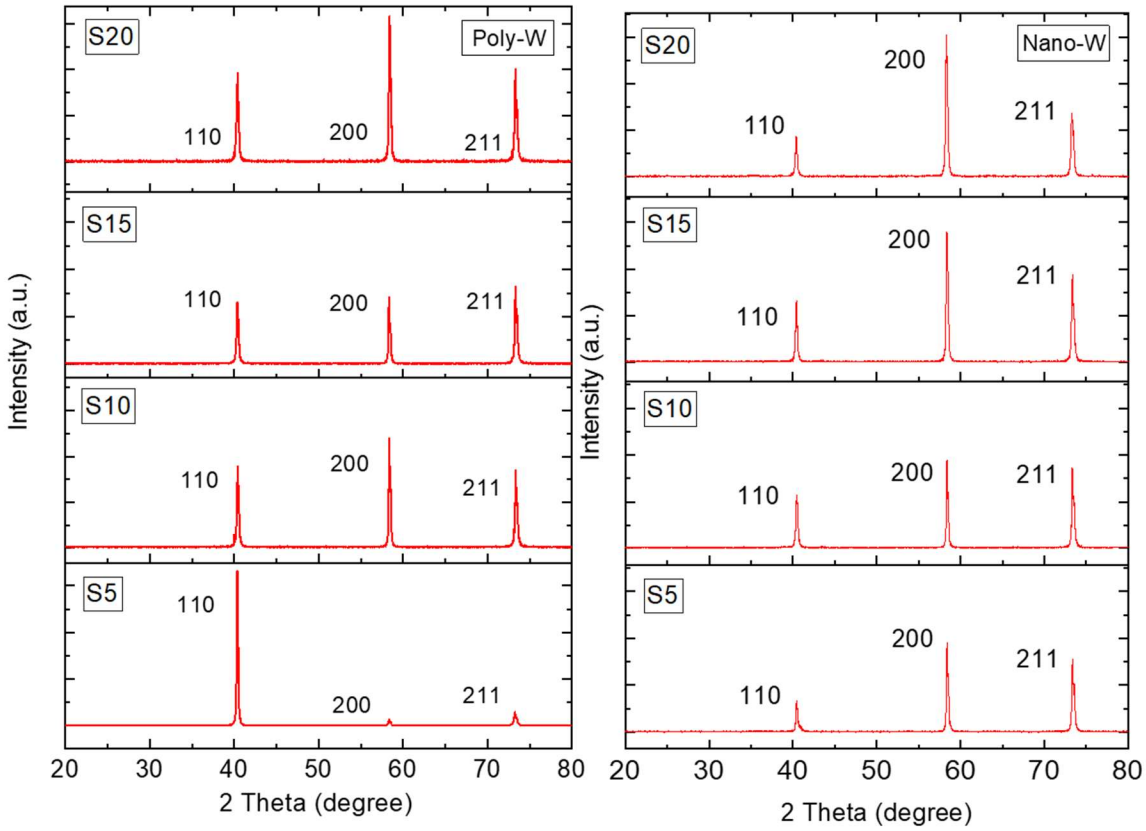

Figure 5.17: XRD spectra for Poly-W (left) and Nano-W (right) irradiated at 5, 10, 15 and 20 focus shots (bottom to top) showing BCC crystal structure having (101), (200) and (211) planes same like unexposed W sample.

These diffraction peaks correspond to BCC crystal structure of tungsten [157]. These peaks are also found on Poly-W and Nano-W samples irradiated by He beams. However, there is a peak shift toward the higher angle due to the decrease in lattice spacing. Intense transient heat load creates vacancies and compressive stress on the irradiated samples.

Figure 5.18 shows (110) peak of exposed Poly-W and Nano-W shifted by 0.30° with respect to the reference samples. However, the peak position of (110) plane is almost the same for Poly-W and Nano-W irradiated at 20 shots [118].

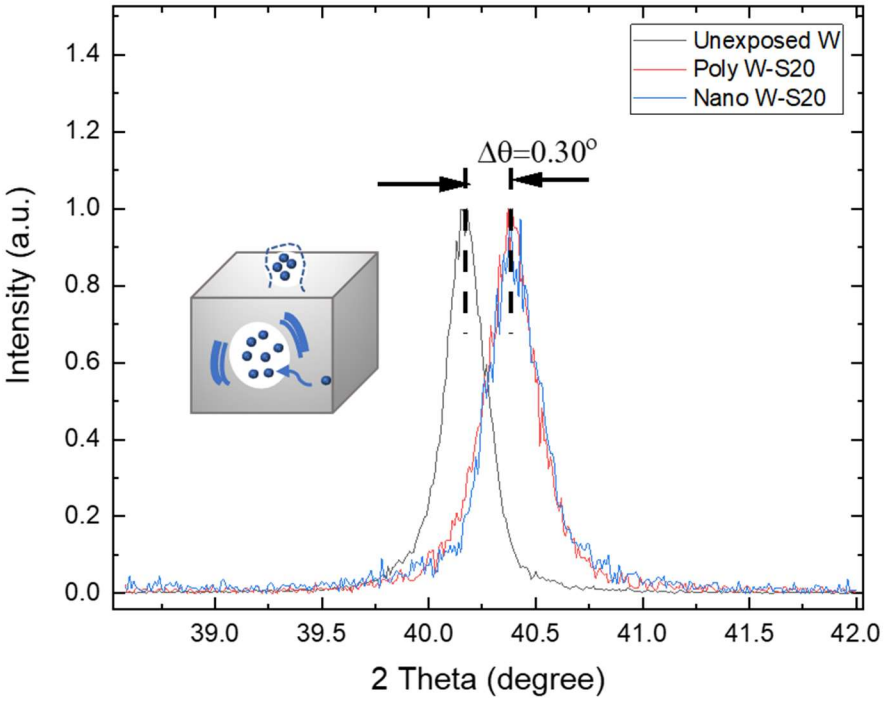

Figure 5.18: Peak shift (θ = 0.30°) in the (101) plane of the Poly-W (red) and Nano-W (blue) samples irradiated at 15 shots towards higher angle compared to the unexposed W (black) confirms the compression stress in the crystal lattice. Pictorial representation of blister and fuzz formation due to the compression stress around the trapped helium bubbles is shown in the graph.

Table 5.2. The peak position, Full Width Half Maximum (FWHM) and crystalline size on the Poly-W and Nano-W samples exposed at 5, 10, 15 and 20 He focus shots.

SAMPLE		2θ(degree)			FWHM (2θ)			Crystallite Size (nm)		
		1 1 0	2 0 0	2 0 1	1 1 0	2 0 0	201	1 1 0	2 0 0	2 0 1
Reference Sample		40.12	58.11	72.99	0.14	0.22	0.20	2.2476	1.5876	1.2962
S5	Poly-W	40.35	58.33	73.24	0.14	0.12	0.22	2.2353	1.5820	1.2925
	Nano-W	40.42	58.38	73.36	0.10	0.12	0.18	2.2316	1.5807	1.2906
S10	Poly-W	40.60	58.36	73.37	0.16	0.14	0.22	2.2353	1.5753	1.2891
	Nano-W	40.28	58.22	73.15	0.24	0.16	0.14	2.2391	1.5848	1.2902
S15	Poly-W	40.39	58.53	73.53	0.16	0.14	0.22	2.2331	1.5811	1.2917
	Nano-W	40.38	58.33	73.31	0.18	0.20	0.14	2.2337	1.582	1.2914
S20	Poly-W	40.36	58.35	73.49	0.24	0.16	0.22	2.2435	1.5815	1.2923
	Nano-W	40.12	58.02	73.01	0.22	0.14	0.16	2.2460	1.5842	1.2946

With an increase in the number of shots from 5 to 20, the crystallize size on the Poly-W and Nano-W samples reduced from 30.41 nm to 28.08 nm and 28.12 nm to 26.63 nm, respectively, as shown in table 5.2. Fig. 5.19 concludes that peak intensity for (200) plane increased relatively due to the ease of the He ion accumulation along this plane [118].

Inter-planar spacing and atomic distances represents compressive stress given by:

$$\frac{\Delta d}{d} = \frac{d(final) - d(initial)}{d(initial)} \tag{5.4}$$

Table 5.3 provides information about strain and compressive stress due to exposure of the samples to10 and 20 helium plasma shots. Elastic constant (κ) of the exposed sample is 4.05×10^{11} N/m^2. Compressive stress can be calculated by multiplying strain and elastic constant of the sample material. It was found to be a maximum stress for d_{110} was found on the samples exposed to 10 successive plasma shots. Due to less helium ion trapping, compressive stress is noted to be lesser in Nano-W as compared to Poly-W samples.

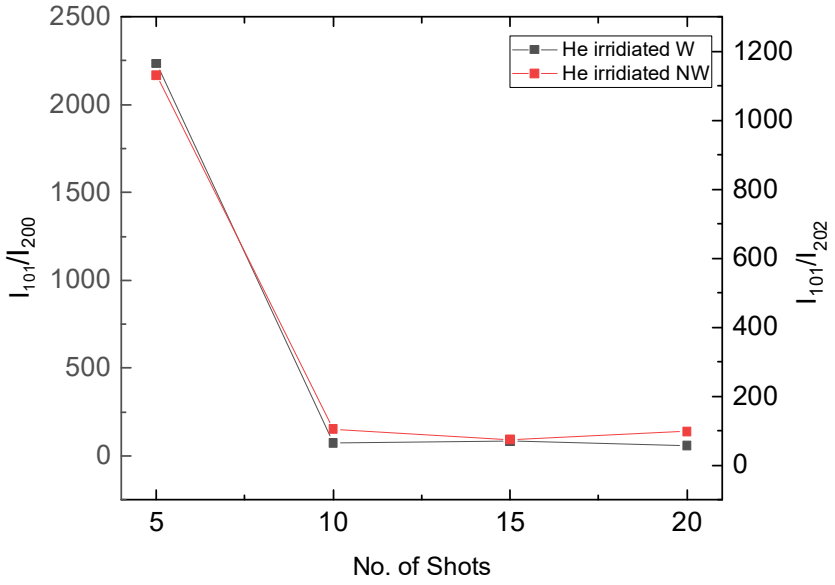

Figure 5.19: Graph shows a fractional variation of the XRD intensities of the three planes for both Poly-W (black) and Nano-W (red) at 5, 10, 15 and 20 shots.

Table 5.3 The Strain and the compressive stress for Poly-W and Nano-W samples exposed to 10 and 20 He focus shots.

For most intense peak (110)	Strain $\left(\frac{\Delta d}{d}\right)$	Compressive stress (N/m^2)
Poly-W (10 shots)	-0.01135	4.497×10^9
Poly-W (20 shots)	-0.00569	2.304×10^9
Nano-W (10 shots)	-0.00378	1.5309×10^9
Nano-W (20 shots)	-0.00071	0.2876×10^9

5.7 Surface Hardness Modification Revealed by Nano-Indentation Test

Plasma facing materials experience high heat loads, which leads to the surface defects seen in SEM images (Fig. 5.6 and Fig. 5.9). There is a possibility of trapping of ion particles due to high ion fluence, which may increase the hardness of the exposed surface. Pre-existing mechanical defects (grain boundaries, dislocation loops, impurity clusters) on the surfaces of unirradiated tungsten samples act as pinning sites against the motion of dislocations. He ions are highly mobile in nature and get easily trapped by voids, vacancies and bubbles. He atom has a high binding energy (1 eV) and thus shows a self-trapping effect [158]. Successive ion pulses enhance the implantation of plasma particles (He ions) and create nanocavities (He bubbles) in the subsurface region. These immobile defects suppress the dislocation motion, which results in hardness of the material [159, 160]. This limits the flow of thermo-mechanical stresses in the material and may lead to mechanical failure. Fig. 5.20 shows the variation of hardness with number of shots. There is a reduction in the hardness value of Poly-W from 9.89 GPa to 0.82 GPa for exposure of 5 shots.

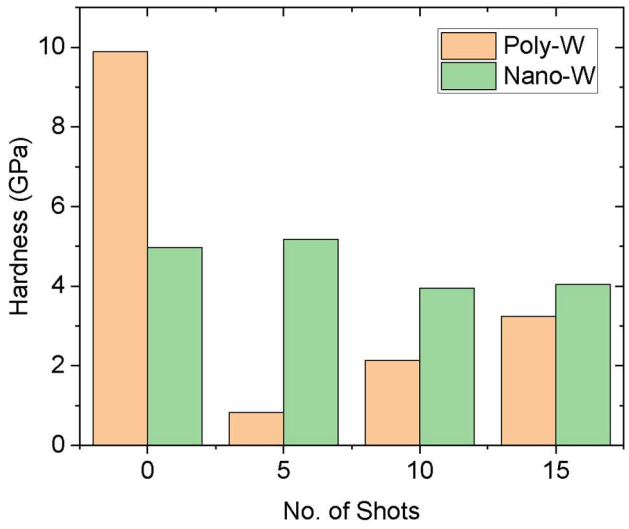

Figure 5.20: Graph shows variation of hardness (GPa) value with respect to the number of shots for both Poly-W (yellow) and Nano-W (green) at 0, 5, 10 and 15 shots.

The result mainly represents the increase in the roughness of the surface. While in the case of nano-W it remained almost the same. With the rise in number of shots, the hardness of Poly-W is found to be increased (3.24 GPa) due to the trapping of helium bubbles. However, the increment in hardness is comparatively lesser in nano-W than Poly-W, as shown in Fig. 5.20. Thus, NI results show lower He bubble density in nano-W. Similar results have been found in SEM and BSE imaging.

SUMMARY

The oldest and most prominent source of energy in Sun is powered by nuclear fusion reaction. Fusion reactor is a design that will scale down the Sun on Earth. Magnetic confinement provides a virtual cage to hold highly dense and hot (hundreds of millions of degrees Celsius) fusion fuel in a so-called plasma state. However, this method involves the interaction of the hot plasma with the wall of the reactor chamber. Selection of the plasma-facing material is one of the most important issues in designing nuclear fusion reactors.

Dense Plasma Focus (DPF) is a co-axial gun in which plasma is subjected to the magnetic driving force and creates plasma in the similar harsh conditions as that in the fusion reactor. It may also be considered as the table-top fusion reactor. The UofS-I DPF at University of Saskatchewan has been used for learning the device operation in this research project. The problems related to device leakage and spark gap were fixed and the system was brought back to operation after sitting in idle for some time. The UNU/ ICPT DPF at the Nanyang Technological University in Singapore is a 3 kJ fusion device powered by 30 μF fast discharging capacitor bank with 13.9kV charging voltage.

Tungsten is one of the suggested plasma-facing materials because of its intrinsic properties such as high resistance to sputtering, high melting point, low activation by neutron exposure and low tritium retention. However, surface or subsurface defects due to high heat loads in nuclear fusion reactors degrades its quality. In this work, surface morphological and crystallographic changes in tungsten and nanostructured tungsten due to irradiation of Helium from the DPF plasma have been studied.

Discharge waveforms of the UNU/ ICPT DPF devices have been recorded with diagnostics probes: Discharge current signals with a Rogowski coil, voltage signals with a resistance voltage divider circuit and ion emission measurements with a negatively biased Faraday cup. Axial rundown time is found to be 1.88 μs and the T.O.F. for the peak ion beam signal with respect to the X-ray peak is 250 ns. The ion intensity signal peak vs. pressure plot indicate that the 200 Pa is the optimal working pressure to generate the highest peak ion beam intensity. Fitting of the dN/dE vs E plot to an empirical energy spectral power law give a exponent of -1.75. The ion flux and ion fluence are calculated and found to be 2.3×10^{28} $m^{-2}s^{-1}$ and 4.577×10^{20} m^{-2}, respectively. The

damage factor due to He ions from the UNU/ICPT DPF is nearly equal to the expected damage factor in ITER during the ELMs events which gives rise to the highest instantaneous heat load on the divertor plates. Thus, UNU/ICPT DPF is a good device to be used to study PFMs as it stimulates the similar harsh environment in fusion reactors.

Effects of ion irradiation on the surface morphology and crystallography have been studied with SEM, EDX, BSE imaging and XRD. Poly-W samples were exposed to 5, 10, 15 and 20 DPF shots at a distance 7 cm from the anode tip. At 5 shots, minor surface defects (bursting tails, low-density bubbles) have been found. With an increase in number of shots, the nano-fuzz structure has been found. Due to continual exposure of ion flux, displacement damage increases, leading to bubble formation. The density of the subsurface bubbles, blisters and micro-cracks increased. At 20 shots, complete re-crystallization of surface due to surface melting and etching has been observed.

Nano structuration has been proposed as a mean to improve surface quality against high heat load. For nano-structuration, UNU/ ICPT DPF operated with Ar as a working gas has been used. Poly-W samples were exposed to 5, 8, 10 and 15 DPF shots at the same distance from the anode (7 cm). With an increase in number of shots, the density of nanoparticles increases. At 10 shots the nanoparticle density is found to be maximum, and the particle size ranges 20-50 nm. However, at 15 shots, nanocrystals aggregated, and micro-cracks around grain boundaries have been found. This is due to the thermal treatment of exposed tungsten samples. Nano-W has been synthesized at 10 optimized shots for further investigation.

Surface damage of Nano-W samples because of He irradiation at 5, 10, 15 and 20 shots has been studied. The growth of nanostructures on the surface increased with an increase in the number of shots. The number of micro-cracks increased and trapping of the helium bubbles around grain boundaries resulted in nanopores. At 15 shots, the cauliflower-like structure composed of a bunch of nanoparticles, has been found. Irradiation with 20 shots resulted in re-solidification of the sample surface and the cluster of the nanoparticles disappeared.

Surface impurities and the compound formation due to continuous irradiation of the sample in Helium plasma have been observed with EDX techniques. C, O, Cu and Fe elements have been found as surface impurities. C and O contents were already present on the sample surface; however, Cu impurity has been introduced due to sputtering of the copper anode surface. EDX technique is unable to detect the presence of the light elements like He on the sample surface.

BSE imaging can be effectively used to analyze the surface up to 100 nm depth. It gives the image based on Z contrast. Therefore, it was used as a technique to detect the trapped He bubbles in subsurface, and nano fuzz on the surface. Colored photos have been used to get a better distinction between low-Z and high-Z elements. Circular red patches give the evidence presence of low-Z (He) bubbles or blisters on the Poly-W sample. However, in the case of nano-W red texture found to be little distributed, which gives an indication of trapped He in nano fuzz and along the grain boundaries. BSE results are consistent with SEM observations.

XRD spectra of unexposed W shows (110), (200) and (211) diffraction peaks at 40.15°, 58.14° and 73.01° and confirms that it has a BCC crystal structure. XRD pattern of exposed Poly-W and nano-W shows the same diffraction peaks with some peak shift, peak broadening and intensity variation of the respective peaks. Peak broadening depicts an increase in amorphization due to increased thermal loads. The (101) diffraction peak is found to be shifted by 0.30° towards higher 2θ diffraction angle. Shifting in the peak position to higher angle is mainly due to the increase in the compression stress around the trapped helium bubbles. There is an increase in the intensity of (200) planes, which indicates that more crystals are aligned along this plane.

Nano indentation test revealed that due to self-trapping effect of the helium atoms, the implanted ions are more easily trapped in the voids, vacancies and bubbles. These immobile defects suppress the dislocation motion, and thus increase the hardness of the material. The increment in the hardness value for the poly-W found to be higher than that for nano-W. This result is expected due to the lesser helium ion trapping in nano-W.

Present work proves that nano structuration could be one of the solutions to improve the material properties against high energy loads.

The current work could be expanded. TEM imaging of the cross-section may be used to further analyze the helium bubble trapping. Inert gases puffing has been proposed as a source of radiation to defuse the heat load on the divertor plates in fusion reactors. DPF may be used to study the impact of inert gases on the material surface and helium ion desorption. It has also been proposed by I. Mazul *et al.* [161] to use heavy metal alloy (Ni/Fe) with W as one of the prominent plasmas facing candidates. It improves ductility and fracture toughness of the material. Possible future work involves nano structuration of W alloy with heavy metals (with Fe or Ni) and study of surface morphology and crystallography.

REFERENCES

1 J. Conti, P. Holtberg, J. Diefenderfer, J. Conti, P. Holtberg, J. Diefenderfer, A. LaRose, J. T. Turnure and L. Westfall. "International energy outlook 2016 with projections to 2040." USDOE Energy Information Administration (EIA), Washington, DC (United States). Office of Energy Analysis, **2016.**

2 M. Keilhacker, A. Gibson, C. Gormezano, P. J. Lomas, P. R. Thomas, M. L. Watkins, P. Andrew, B. Balet, D. Borba, C. D. Challis, I. Coffey. "High fusion performance from deuterium-tritium plasmas in JET." *Nuclear Fusion*, vol. 39, no. 2, pp. 209, **1999.**

3 M. R. Gilbert, J. C. Sublet. "Neutron-induced transmutation effects in W and W-alloys in a fusion environment." *Nuclear Fusion*, vol. 51, no. 4, pp. 043005, **2011.**

4 C. Bourdelle, J. F. Artaud, V. Basiuk, M. Bécoulet, S. Brémond, J. Bucalossi, H. Bufferand, G. Ciraolo, L. Colas, Y. Corre and X. Courtois. "WEST physics basis." *Nuclear Fusion*, vol. 55, no .6, pp.063017, **2015.**

5 M. Abdou, E. Vold, C. Gung, M. Youssef, and K. Shin. "Deuterium–Tritium fuel self-sufficiency in fusion reactors." *Fusion Technology*, vol. 9, pp. 250–285, **1986.**

6 W. Crookes. "I. On a fourth state of matter, in a letter to the Secretary. By W. Crookes, FR S." *Proceedings of the Royal Society of London*, vol. 30, no. 200-205, pp. 469-472, **1880.**

7 I. Langmuir. "Oscillations in ionized gases." *Proceedings of the National Academy of Sciences of the United States of America*, vol. 14, no.8, pp. 627, **1928**.

8 K. M. Hthu. "Edge Ion Temperature Measurement in the STOR-M Tokamak." *M.Sc. Thesis, University of Saskatchewan*, **2012.**

9 J. Adegun. "Effect of lithium coating on the impurities and shielding effect of plasma on the resonant magnetic perturbations field in the STORM-M tokamak plasma*." M. Sc. Thesis, Univ*ersity of Saskatchewan, **2017.**

10 F. F. Chen. "Introduction to Plasma Physics and Controlled Fusion." Springer Science and Business Media, LLC, 2006

11 M. A. Abdou, E. L. Vold, C. Y. Gung, M. Z. Youssef and K. Shin. "Deuterium-tritium fuel self-sufficiency in fusion reactors." *Fusion Technology*, vol. 9, no. 2, pp.250-285, **1986.**

12 M. Rieth, S. L. Dudarev, S. G. De Vicente, J. Aktaa, T. Ahlgren, S. Antusch, D. E. J. Armstrong, M. Balden, N. Baluc, M. F. Barthe and W. W. Basuki. "Recent progress in research on tungsten materials for nuclear fusion applications in Europe," *Journal of Nuclear Materials*, vol. 432, no. 1, pp. 482–500, **2013.**

13 J. N. Brooks, J. P. Allain, R. P. Doerner, A. Hassanein, R. Nygren, T. D. Rognlien, and D. G. Whyte. "Plasma-surface interaction issues of an all-metal iter." *Nuclear Fusion*, vol. 49, No. 3, pp. 035007, **2009.**

14 T. Hirai, F. Escourbiac, S. Carpentier-Chouchana, A. Fedosov, L. Ferrand, T. Jokinen, V. Komarov, A. Kukushkin, M. Merola, R. Mitteau, and R. A. Pitts. "ITER tungsten divertor design development and qualification program." *Fusion Engineering and Design*, vol. 88, no. 9-10, pp. 1798-1801, **2013.**

15 K. Ezato, S. Suzuki, Y. Seki, K. Mohri, K. Yokoyama, F. Escourbiac, T. Hirai, and V. Kuznetcov. "Progress of iter full tungsten divertor technology qualification in japan." *Fusion Engineering and Design*, vol. 98, pp. 1281-284, **2015.**

16 T. Hirai, S. Panayotis, V. Barabash, C. Amzallag, F. Escourbiac, A. Durocher, M. Merola, J. Linke, Th. Loewenho, G. Pintsuk, and M. Wirtz. "Use of tungsten material for the iter divertor." *Nuclear Materials and Energy*, vol. 9, pp. 616-622**, 2016.**

17 T. Hirai, S. Carpentier-Chouchana, F. Escourbiac, S. Panayotis, A. Durocher, L. Ferrand, M. Garcia-Martinez, JP. Gunn, V. Komarov, M. Merola, and R. A. Pitts. "Design optimization of the iter tungsten divertor vertical targets. Fusion Engineering and Design." vol. 127, pp. 66-72, **2018.**

18 H. Trinkaus, B. N. Singh. "Helium accumulation in metals during irradiation–where do we stand?." *Journal of Nuclear Materials*, vol. 323 no. 2-3, pp. 229-42, **2003**

19 J. Boisse, C. Domain and C. S. Becquart. "Modelling self trapping and trap mutation in tungsten using DFT and Molecular Dynamics with an empirical potential based on DFT." *Journal of Nuclear Materials*. vol. 455, no.1-3, pp. 10-5, **2014.**

20 W. D. Wilson, C. L. Bisson and M. I. Baskes. "Self-trapping of helium in metals" *Physics Review B*, vol. 24, no. 10, pp. 5616-5624, **1981.**

21 M. I. Baskes and W. D. Wilson. "Kinetics of helium self-trapping in metals." *Physical Review B*, vol. 27 no. 4, pp. 2210, **1983.**

22 J. H. Evans. “An interbubble fracture mechanism of blister formation on helium-irradiated metals,” *Journal of Nuclear Materials*, vol. 68, no. 2, pp. 129–140, **1977.**

23 E. Gao and N. M. Ghoniem. “A coupled rate theory-Monte Carlo model of helium bubble evolution in plasma-facing micro-engineered tungsten.” *Journal of Nuclear Materials*, vol. 509, pp. 577-590, **2018.**

24 K. O. Henriksson, K. Nordlund, A. Krasheninnikov and J. Keinonen. “The depths of hydrogen and helium bubbles in tungsten: a comparison.” *Fusion science and technology*, vol. 50, no. 1, pp. 43-57, **2006.**

25 R. S. Barnes and D. J. Mazey. “The migration and coalescence of inert gas bubbles in metals.” *Proceedings of the Royal Society of London. Series A. Mathematical and Physical Sciences*, vol. 275, no. 1360, pp. 47-57, **1963.**

26 R. J. Hawryluk. “Results from D—T experiments on TFTR and implications for achieving an ignited plasma.” *Philosophical Transactions of the Royal Society of London. Series A: Mathematical, Physical and Engineering Sciences*, vol. 357, no. 1752, pp. 443-469, **1999.**

27 G. Federici, C. H. Skinner, J. N. Brooks, J. P. Coad, C. Grisolia, A. A. Haasz, A. Hassanein, V. Philipps, C. S. Pitcher, J. Roth, W. R. Wampler. “Plasma-material interactions in current tokamaks and their implications for next step fusion reactors.” *Nuclear Fusion*, vol. 41, no. 12, pp. 1967- 2137, **2001.**

28 M. Ulrickson, V. Barabash, S. Chiocchio, G. Federici, G. Janeschitz, R. Matera, M. Akiba, G. Vieider, C. Wu and I. Mazul. “Selection of plasma facing materials for ITER.” *IEEE In Proceedings of 16th International Symposium on Fusion Engineering,* vol. 1, pp. 394-398, **1995.**

29 R. Dux, R. Neu, V. Bobkov, H. Greuner, O. Gruber, C. Hopf, A. Kallenbach, T Pütterich, V. Rohde, and ASDEX Upgrade Team. “Tungsten as first wall material in Asdex upgrade.” *In 21st IAEA Fusion Energy Conference. International Atomic Energy Agency*, **2007.**

30 L. L. Snead and T. D. Burchell. “Reduction in Thermal Conductivity Due to Neutron Irradiation." *In 22nd Biennial Conference on Carbon, Extended Abstracts*, pp. 774-775, **1995.**

31 V. Barabash, M. Akiba, I. Mazul, M. Ulrickson and G. Vieider. “Selection, development and characterisation of plasma facing materials for ITER.” *Journal of Nuclear Materials*, vol. *233*, pp. 718-723, **1996.**

32 A. Kirschner, V. Philipps, J. Winter, and U. Kögler. “Simulation of the plasma-wall interaction in a tokamak with the Monte Carlo code ERO-TEXTOR.” *Nuclear Fusion*, vol. 40, no. 5, pp.989, **2000.**

33 V. Kh. Alimov and J. Roth. “Hydrogen isotope retention in plasma-facing materials: review of recent experimental results.” *Physica Scripta*, vol. 6, no. T128, pp. 6, **2007.**

34 J. W. Davis, V. R. Barabash, A. Makhankov, L. Plöchl, and K. T. Slattery. “Assessment of tungsten for use in the iter plasma facing components1.” *Journal of nuclear materials*, vol. 258, pp. 308-312, **1998.**

35 K. L. Wilson, R. A. Causey, W. L. Hsu, B. E. Mills, M. F. Smith and J. B. Whitley. “Beryllium—a better tokamak plasma-facing material?.” *Journal of Vacuum Science & Technology A: Vacuum, Surfaces, and Films*, vol. 8, no. 3, pp. 1750-1759, **1990.**

36 R. A. Causey, W. L. Hsu, B. E. Mills, B, J. Ehrenberg and V. Phillips. “Tritium retention and migration in beryllium.” *Journal of nuclear materials*, vol. 176, pp.654-660, **1990.**

37 L. A. Izhvanov, V. V. Khromonozhkin, B. G. Drozdov and V. G. Vil'chinskij. “Degassing from powders and compact beryllium.” *Poroshkovaya Metallurgiya (Kiev)*, pp. 56-61. **1985.**

38 R. A. Langley, J. Bohdansky, W. Eckstein, P. Mioduszewski, J. Roth, E. Taglauer, E. W. Thomas, H. Verbeek and K. L. Wilson. “Data compendium for plasma-surface interactions.” *Nuclear Fusion*, vol. 24*,* no. S1, pp. S9, **1984.**

39 E. T. Cheng, K. R. Schultz and C. P. C. Wong. “Activation evaluation of fusion solid breeder materials.” In *IEEE Thirteenth Symposium on Fusion Engineering,* pp. 1116-1119, **1989.**

40 ITER Concept Definition, Vol. 1, ITER Documentation Series, No. 3, IAEA, Vienna, **1989.**

41 J. Roth, W. Eckstein, and M. Guseva. “Erosion of Be as plasma-facing material.” *Fusion Engineering and Design*, vol. 37, no. 4, pp. 465-480, **1997.**

42 I. Langmuir. “The vapor pressure of metallic tungsten.” *Physics Review*, vol. 2, no. 5, pp. 329–342, **1913.**

43 R. W. Powell, C. Y. Ho and P. E. Liley. “Thermal conductivity of selected materials.” *Washington, DC: US Department of Commerce, National Bureau of Standards*, vol. 8, **1966**.

44 *“Tungsten - Thermal Expansion Coefficient*. Periodic Table.” https://www.periodic-table.org/tungsten-thermal-expansion/. [Retrieved 1 May 2020]

45 V. Philipps. “Tungsten as material for plasma-facing components in fusion devices.” *Journal of nuclear materials*, vol. 415, no. 1, pp. S2-S9. **2011.**

46 R. Frauenfelder. “Solution and diffusion of hydrogen in tungsten.” *Journal of Vacuum Science and Technology*, vol. 6, no. 3, pp. 388-397, **1969.**

47 A. A. Mazaev, R. G. Avarbe and Y. N. Vil'k. “Solubility of hydrogen in tungsten at high temperatures.” *Izvestiâ Akademii nauk SSSR. Metally,* vol. 6, pp. 223-6, **1968.**

48 R. Frauenfelder. “Permeation of hydrogen through tungsten and molybdenum.” *The Journal of Chemical Physics*, vol. 48, no. 9, pp. 3955-3965, **1968.**

49 C. Linsmeier, M. Rieth, J. Aktaa, T. Chikada, A. Hoffmann, J. Hoffmann, A. Houben, H. Kurishita, X. Jin, M. Li and A. Litnovsky. “Development of advanced high heat flux and plasma-facing materials.” *Nuclear Fusion*, vol. 57, no. 9, pp. 092007, **2017.**

50 H. Bolt, V. Barabash, W. Krauss, J. Linke, R. Neu, S. Suzuki, N. Yoshida and A. U. Team. “Materials for the plasma-facing components of fusion reactors.” *Journal of nuclear materials*, vol. 329, pp. 66-73, **2004.**

51 M. Faleschini, H. Kreuzer, D. Kiener and R. Pippan. “Fracture toughness investigations of tungsten alloys and SPD tungsten alloys.” *Journal of Nuclear Materials*, vol. 367, pp. 800-805, **2007.**

52 S. Wurster and R. Pippan. “Nanostructured metals under irradiation.” *Scripta Materialia*, vol. 60, no. 12, pp.1083-1087, **2009.**

53 H. Kurishita, Y. Kitsunai, T. Shibayama, H. Kayano and Y. Hiraoka. “Development of Mo alloys with improved resistance to embrittlement by recrystallization and irradiation.” *Journal of nuclear materials*, vol. 233, pp. 557-564, **1996.**

54 M. Rose, A. G. Balogh and H. Hahn. “Instability of irradiation induced defects in nanostructured materials.” *Nuclear Instruments and Methods in Physics Research Section B: Beam Interactions with Materials and Atoms*, vol. 127, pp. 119-122, **1997.**

55 M. Yajima, Y. Hatano, S. Kajita, J. Shi, M. Hará and N. Ohno. “Tritium retention in nanostructured tungsten with large effective surface area.” *Journal of Nuclear Materials*, vol. 438, pp. S1142-S1145, **2013.**

56 O. El-Atwani, C. N. Taylor, J. Frishkoff, W. Harlow, E. Esquivel E, S. A. Maloy, M. L. Taheri. “Thermal desorption spectroscopy of high fluence irradiated ultrafine and

nanocrystalline tungsten: helium trapping and desorption correlated with morphology". *Nuclear Fusion*, vol. 58, no. 1, pp. 016020, **2017.**

57 W. Han, E. G. Fu, M. J. Demkowicz, Y. Wang and A. Misra. "Irradiation damage of single crystal, coarse-grained, and nanograined copper under helium bombardment at 450 C." *Journal of Materials Research*, vol. 28 no. 20 , pp. 2763-2770, **2013.**

58 S. Takamura, N. Ohno, D. Nishijima and S. Kajita. "Formation of nanostructured tungsten with arborescent shape due to helium plasma irradiation." *Plasma and fusion research 1*, pp.051-051, **2006.**

59 M. J. Baldwin and R. P. Doerner. "Helium induced nanoscopic morphology on tungsten under fusion relevant plasma conditions." *Nuclear Fusion*, vol. 48, no. 3, pp. 035001, **2008.**

60 S. Nagata, B. Tsuchiya, T. Sugawara, N. Ohtsu and T. Shikama. "Helium and hydrogen trapping in W and Mo single-crystals irradiated by He ions." *Journal of nuclear materials*, vol. 307, pp. 1513-1516, **2002.**

61 D. Nishijima, M. Y. Ye, N. Ohno and S. Takamura. "Formation mechanism of bubbles and holes on tungsten surface with low-energy and high-flux helium plasma irradiation in NAGDIS-II." *Journal of nuclear materials*, vol. 329, pp. 1029-1033, **2004.**

62 M. Y. Ye, H. Kanehara, S. Fukuta, N. Ohno and S. Takamura. "Blister formation on tungsten surface under low energy and high flux hydrogen plasma irradiation in NAGDIS-I." *Journal of nuclear materials*, vol. 313, pp. 72-76, **2003.**

63 W. Sakaguchi, S. Kajita, N. Ohno and M. Takagi. "In situ reflectivity of tungsten mirrors under helium plasma exposure." *Journal of nuclear materials*, vol. 390, pp. 1149-1152, **2009.**

64 N. Yoshida, H. Iwakiri, K. Tokunaga and T. Baba, T. "Impact of low energy helium irradiation on plasma facing metals." *Journal of nuclear materials*, vol. 337, pp. 946-950, **2005.**

65 K. D. Hammond. "Helium, hydrogen, and fuzz in plasma-facing materials." *Materials Research Express*, vol. 4, no. 10, pp. 104002, **2017.**

66 S. Gonderman, Tripathi, J.K., Sizyuk, T. and Hassanein, A., 2017. "Suppression of surface microstructure evolution in W and W–Ta alloys during simultaneous and sequential He and D ion irradiation in fusion relevant conditions." *Nuclear Fusion*, *57*(8), p.086001.

67 M. J. Baldwin and R. P. Doerner. “Formation of helium induced nanostructure ‘fuzz’ on various tungsten grades.” *Journal of Nuclear Materials*, vol. 404, no. 3, pp. 165-173, **2010.**

68 H. Iwakiri, K. Morishita and N. Yoshida. “Effects of helium bombardment on the deuterium behavior in tungsten.” *Journal of nuclear materials*, vol. 307, pp. 135-138, **2002.**

69 B. Tyburska, V. K. Alimov, O. V. Ogorodnikova, K. Schmid and K. Ertl, K. “Deuterium retention in self-damaged tungsten.” *Journal of nuclear materials*, vol. 395, no. 1-3, pp. 150-155, **2009.**

70 H. Iwakiri, K. Yasunaga, K. Morishita and N. Yoshida. “Microstructure evolution in tungsten during low-energy helium ion irradiation.” *Journal of nuclear materials*, vol. 283, pp. 1134-1138, **2000.**

71 Z. Zhang, E. Hasenhuetl, K. Yabuuchi and A. Kimura. “Evaluation of helium effect on ion-irradiation hardening in pure tungsten by nano-indentation method.” *Nuclear Materials and Energy*, vol. 9, pp. 539-546, **2016.**

72 D. E. J. Armstrong, P. D. Edmondson and S. G. Roberts. “Effects of sequential tungsten and helium ion implantation on nano-indentation hardness of tungsten.” *Applied Physics Letters*, vol. 102, no. 25, pp. 251901, **2013.**

73 H. Iwakiri, H. Wakimoto, H. Watanabe and N. Yoshida. “Hardening behavior of molybdenum by low energy He and D ion irradiation.” *Journal of nuclear materials*, vol. 258, pp. 873-878, **1998.**

74 F. Kong, M. Qu, S. Yan, A. Zhang, S. Peng, J. Xue and Y. Wang. “Helium-induced hardening effect in polycrystalline tungsten.” *Nuclear Instruments and Methods in Physics Research Section B: Beam Interactions with Materials and Atoms*, vol. 406, pp. 643-647, **2017.**

75 D. Nishijima, M. Y. Ye, N. Ohno and S. Takamura. “Incident ion energy dependence of bubble formation on tungsten surface with low energy and high flux helium plasma irradiation.” *Journal of nuclear materials*, vol. 313, pp. 97-101, **2003.**

76 J. Cui, Z. Wu and Q. Hou. “Estimation of the lifetime of small helium bubbles near tungsten surfaces–A methodological study.” *Nuclear Instruments and Methods in Physics Research Section B: Beam Interactions with Materials and Atoms*, vol. 383, pp. 136-142, **2016.**

77 F. Sefta, K. D. Hammond, N. Juslin and B. D. Wirth. “Tungsten surface evolution by helium bubble nucleation, growth and rupture.” *Nuclear Fusion*, vol. 53, no. 7, pp. 073015, **2013.**

78 F. Maury, M. Biget, P. Vajda, A. Lucasson and P. Lucasson. “Frenkel pair creation and stage I recovery in W crystals irradiated near threshold,” *Radiation Effect*, vol. 38, no. 1–2, pp. 53–65, **1978**.

79 S. Sharafat, A. Takahashi, K. Nagasawa and N. Ghoniem. “A description of stress driven bubble growth of helium implanted tungsten.” *Journal Nuclear Materials*, vol. 389, no. 2, pp. 203–212, **2009**.

80 S. Kajita, N. Yoshida, R. Yoshihara, N. Ohno, M. Yamagiwa. “TEM observation of the growth process of helium nanobubbles on tungsten: Nanostructure formation mechanism.” *Journal Nuclear Materials*, vol. 418, no. 1-5, pp. 152-158, **2011.**

81 G. Nogay, E. Özkol, S. Ilday and R.A.Ş.İ.T. Turan. “Structural peculiarities and aging effect in hydrogenated a-Si prepared by inductively coupled plasma assisted chemical vapor deposition technique.” *Vacuum*, vol. 110, pp. 114-120, **2014.**

82 J. Zhu, Z. Wang, H. Yu, N. Li, J. Zhang, J. Meng, M. Liao, J. Zhao, X. Lu, L. Du and R. Yang. “Argon plasma induced phase transition in monolayer MoS2.” *Journal of the American Chemical Society*, vol. 139, no. 30, pp. 10216-10219, **2017.**

83 J. W. Lim and S. J. Yun. “Method for forming nitrogen-containing oxide thin film using plasma enhanced atomic layer deposition.” U.S. Patent 6,723,642. **2004.**

84 M. Lang, R. Henne, S. Schaper and G. Schiller. “Development and characterization of vacuum plasma sprayed thin film solid oxide fuel cells.” *Journal of thermal spray technology*, vol. 10, no. 4, pp. 618-625, **2001.**

85 M. Meyyappan. “Plasma nanotechnology: Past, present and future,” *Journal of Physics D: Applied Physics,* vol. 44, no. 17, pp. 174002, **2011**.

86 Committee High Energy Density Plasma Phys., Plasma Sci. Committee, Nat. Res. Council, Frontiers in High Energy Density Physics: The X-Games of Contemporary Science, Washington, DC: Nat. Acad. Press, **2003**.

87 B. A. Remington, R. P. Drake and D. D. Ryutov. “Experimental astrophysics with high power lasers and Z pinches.” *Reviews of Modern Physics*, vol. *78, no.* 3, pp. 755, **2006.**

88 F. Sun, A. Qiu, Z. Zeng, J. Zeng, B. Kuai and H. Yang. “Development of pulsed high current drivers for fast Z-pinch.” *High Power Laser and Particle Beams*, vol. 18, no. 3, pp. 513-520, **2006.**

89 L. Soto. “New trends and future perspectives on plasma focus research.” *Plasma Physics Control Fusion*, vol. 47, no. 5A, pp. A361–A381, **2005.**

90 P. Cloth and H. Conrads. “Neutronics of a dense-plasma focus—An investigation fusion plasma,” *Nuclear Science Engineering*, vol. 62, no. 4, pp. 591– 600, **1977.**

91 M. V. Roshan, S. V. Springham, R. S. Rawat, and P. Lee. “Short lived PET radioisotope production in a small plasma focus device.” *IEEE Transactions on Plasma Science*, vol. 38, no. 12, pp. 3393–3397, **2010.**

92 E. H. Beckner. “Production and diagnostic measurements of kilovolt high-density deuterium, helium, and neon plasmas,” *Journal of Applied Physics*, vol. 37, no. 13, pp. 4944-4952, **1966.**

93 R. Verma, R. S. Rawat, P. Lee, M. Krishnan, S. V. Springham, and T. L. Tan. “Miniature plasma focus device as a compact hard X-ray source for fast radiography applications.” *IEEE Transactions on Plasma Science*, vol. 38, no. 4, pp. 652–657, **2010.**

94 J. N. Feugeas, E. C. Llonch, C. O. De Gonzalez and G. Galambos. “Nitrogen implantation of AISI 304 stainless steel with a coaxial plasma gun.” *Journal of applied physics*, vol. 64, no. 5, pp. 2648-2651, **1988.**

95 R. S. Rawat, M. P. Srivastava, S. Tandon and A. Mansingh. “Crystallization of an amorphous lead zirconate titanate thin film with a dense-plasma-focus device.” *Physical Review B*, vol. 47, no. 9 pp. 4858, **1993.**

96 C. R. Kant, M. P. Srivastava and R. S. Rawat. “Thin carbon film deposition using energetic ions of a dense plasma focus.” *Physics letters A*, vol. 226, no. 3-4, pp. 212-216, **1997.**

97 R. S. Rawat, P. Lee, T. White, L. Ying and S. Lee. “Room temperature deposition of titanium carbide thin films using dense plasma focus device.” *Surface and Coatings Technology*, vol. 138, no. 2-3, pp. 159-165, **2001.**

98 M. Shiotani, K. Takao, T. Honda, I. Kitamura, T. Takahashi and K. Masugata, K. “CHARACTERISTICS OF ENERGTIC IONS PRODUCED IN PLASMA FOCUS. *RESEARCH REPORT NIFS-PROC Series*, pp. 120, **2001.**

99 M. Sadiq, S. Ahmad, M. Shafiq and M. Zakaullah. “Nitrogen ion implantation of silicon in dense plasma focus.” *Nuclear Instruments and Methods in Physics Research Section B: Beam Interactions with Materials and Atoms*, vol. 252, no. 2, pp. 219-224, **2006.**

100 M. T. Hosseinnejad, M. Shirazi, Z. Ghorannevis, M. Ghoranneviss and F. Shahgoli. "Using Mather-type plasma focus device for fabrication of tungsten thin films." *Journal of fusion energy*, vol. *31*, no. 5, pp. 426-431, **2012.**

101 R. Gupta and M. P. Srivastava. "Carbon ion implantation on titanium for TiC formation using a dense plasma focus device." *Plasma Sources Science and Technology*, vol. *13, no.* 3, pp. 371, **2004.**

102 M. Hassan, A. Qayyum, R. Ahmad, R. S. Rawat, P. Lee, S. M. Hassan, G. Murtaza and M. Zakaullah. "Dense plasma focus ion-based titanium nitride coating on titanium." *Nuclear Instruments and Methods in Physics Research Section B: Beam Interactions with Materials and Atoms*, vol. 267, no. 11, pp. 1911-1917, **2009.**

103 R. S. Rawat, V. Aggarwal, M. Hassan, P. Lee, S. V. Springham, T. L. Tan and S. Lee, S. "Nano-phase titanium dioxide thin film deposited by repetitive plasma focus: Ion irradiation and annealing based phase transformation and agglomeration." *Applied Surface Science*, vol. 255, no. 5, pp. 2932-2941, **2008.**

104 L. Rico, B. J. Gomez, J. Feugeas and O. de Sanctis. "Crystallization of amorphous zirconium thin film using ion implantation by a plasma focus of 1 kJ." *Applied surface science*, vol. *254, no.* 1, pp. 193-196, **2007.**

105 I. A. Khan, M. Hassan, R. Ahmad, A. Qayyum, G. Murtaza, M. Zakaullah and R. S. Rawat. "Nitridation of zirconium using energetic ions from plasma focus device." *Thin Solid Films*, vol. 516, no. 23, pp. 8255-8263, **2008.**

106 M. Sadiq, S. Ahmad, A. Waheed and M. Zakaullah. "The nitriding of aluminium by dense plasma focus." *Plasma Sources Science and Technology*, vol. *15, no.* 3, pp. 295, **2006.**

107 M. V. Roshan, R. S. Rawat, A. R. Babazadeh, M. Emami, S. S. Kiai, R. Verma, J. J. Lin, A. R. Talebitaher, P. Lee and S. V. Springham. "High energy ions and energetic plasma irradiation effects on aluminum in a Filippov-type plasma focus." *Applied Surface Science*, vol. *255,* no. 5, pp. 2461-2465, **2008.**

108 R. Ahmad, M. Hassan, G. Murtaza, J. I. Akhter, A. Qayyum, A. Waheed and M. Zakaullah. "Co-deposition of titanium and iron nitrides on SS-321 by using plasma focus." *Radiation Effects and Defects in Solids*, vol. *161, no.* 2, pp. 121-129, **2006.**

109 INTERNATIONAL ATOMIC ENERGY AGENCY. "Integrated Approach to Dense Magnetized Plasmas Applications in Nuclear Fusion Technology" *IAEA-TECDOC-1708, IAEA, Vienna* **2013.**

110 R. Kamendje. "Investigations of materials under high repetition and intense fusion-relevant pulses." *In Summary of the 1st Research Coordination Meeting of the IAEA-CRP*, pp. 6-9, **2011.**

111 S. H. Saw, V. Damideh, J. Ali, R. S. Rawat, P. Lee and S. Lee. "Damage Study of Irradiated Tungsten using fast focus mode of a 2.2 kJ plasma focus." *Vacuum*, vol. 144, pp. 14-20, **2017.**

112 N. J. Dutta, N. Buzarbaruah and S. R. Mohanty. "Damage studies on tungsten due to helium ion irradiation." *Journal of Nuclear Materials*, vol. 452, no. 1-3, pp. 51-56, **2014.**

113 M. J. Inestrosa-Izurieta, E. Ramos-Moore, and L. Soto. "Morphological and structural effects on tungsten targets produced by fusion plasma pulses from a table top plasma focus." *Nuclear Fusion*, vol. 55, no. 9, pp. 093011, **2015.**

114 M. Bhuyan, S. R. Mohanty, C. V. S. Rao, P. A. Rayjada and P. M. Raole. "Plasma focus assisted damage studies on tungsten." *Applied surface science*, vol. 264, pp. 674-680, **2013.**

115 R. Niranjan, R. K. Rout, R. Srivastava, Y. Chakravarthy, P. Mishra, T. C. Kaushik and S. C. Gupta. "Surface modifications of fusion reactor relevant materials on exposure to fusion grade plasma in plasma focus device." *Applied Surface Science*, vol. 355, pp. 989-998, **2015.**

116 M. Chernyshova, V. A. Gribkov, E. Kowalska-Strzeciwilk, M. Kubkowska, R. Miklaszewski, M. Paduch, T. Pisarczyk, E. Zielinska, E. V. Demina, V. N. Pimenov and S. A. Maslyaev. "Interaction of powerful hot plasma and fast ion streams with materials in dense plasma focus devices." *Fusion Engineering and Design*, vol. *113*, pp. 109-118, **2016.**

117 A. Hussnain, R. S. Rawat, R. Ahmad, T. Hussain, Z. A. Umar, U. Ikhlaq, Z. Chen and L. Shen. "A study of structural and mechanical properties of nano-crystalline tungsten nitride film synthesis by plasma focus." *Radiation Effects and Defects in Solids*, vol. 170, no. 2, pp. 73-83, **2015.**

118 M. Mohammadreza Seyedhabashi, M. A. Tafreshi, S. Shafiei and A. Abdisaray. "Damage study of irradiated tungsten and copper using proton and argon ions of a plasma focus device." *Applied Radiation and Isotopes*, vol. *154*, pp. 108875, **2019.**

119 J. A. Bittencourt. "Fundamentals of plasma physics." Springer-Verlag NY Inc., **2004.**

120 S. Lee. “Plasma focus radiative model: Review of the Lee model code.” *Journal of Fusion Energy*, vol. 33, no. 4, pp. 319-335, **2014.**

121 P. Gautam and R. Khanal. “Introduction to numerical experiment on plasma focus using lee model code.” *Himalayan Physics*, vol. 5, pp. 137-141, **2014.**

122 J. W. Mather. “Formation of a High-Density Deuterium Plasma Focus.” *The Physics of Fluids*, vol. 8, no. 2, pp. 366-377, **1965.**

123 K. T. A. L. Burm. “Calculation of the townsend discharge coefficients and the paschen curve coefficients.” *Contributions to Plasma Physics*, vol. 47, no. 3, pp.177-182, **2007.**

124 J. W. Mather, P. J. Bottoms, J. P. Carpenter, A. H. Williams and K. D. Ware. “Stability of the dense plasma focus.” *The Physics of Fluids*, vol. 12, no. 11, pp. 2343-2347, **1969.**

125 J. P. Boeuf, L. C. Pitchford and K. H. Schoenbach. “Predicted properties of microhollow cathode discharges in xenon.” *Applied Physics Letters*, vol. 86, no. 7, pp. 071501, **2005.**

126 A. Bernard, A. Coudeville, A. Jolas, J. Launspach and J. De Mascureau. “Experimental studies of the plasma focus and evidence for nonthermal processes.” *The Physics of Fluids*, vol. 18, no. 2, pp. 180-194, **1975.**

127 R. A. Behbahani, A. Hirose and C. Xiao. “Plasma heating and emission of runaway charged particles in a plasma focus device”, *Europhysics Letters*, vol. 113, no. 5, pp. 1-5, **2016.**

128 W. Harries, J. Lee and D. McFarland, “Trajectories of high energy electrons in a plasma focus.” *Plasma Physics*, vol. 20, no. 2, pp. 95-106, **1978**.

129 R. Alibazi Behbahani. “Enhancement of charge particle emission from a plasma focus device.” Doctoral dissertation, *University of Saskatchewan, SK*, **2017**.

130 D. Horsley. “Process Plant Commissioning: a user guide.” *Institution of Chemical Engineers, Rugby, UK, 2nd edition*, **1998**.

131 Carey, W.J., Wiebe, A.J., Nord, R.D. and Altgilbers, L.L., 2011, June. Characterization of Paschen curve anomolies at high P* D values. In *2011 IEEE Pulsed Power Conference* (pp. 741-744). IEEE.

132 R. Verma. “Construction and optimization of low energy miniature repetitive plasma focus neutron source.” Doctoral Dissertation, *National Institute of Education- Nanyang Technical University, Singapore*, **2010.**

133 I. H. Hutchinson. “Principles of plasma diagnostics", *Cambridge University Press*, **1987**

134 S. R. Muhammad. "Compression dynamics and radiation emission from a deuterium plasma focus." Doctoral Dissertation, *National Institute of Education- Nanyang Technical University, Singapore*, **2000**

135 H. Bhuyan, S. R. Mohanty, T. K. Borthakur and R. S. Rawat. "Analysis of nitrogen ion beam produced in dense plasma focus device using Faraday Cup." *Indian Journal of Pure & Applied Physics*, vol. 39, pp. 698, **2001**.

136 S. R. Mohanty, H. Bhuyan, N. K. Neog, R. K. Rout and E. Hotta. "Development of multi Faraday cup assembly for ion beam measurements from a low energy plasma focus device." *Japanese Journal of Applied Physics*, vol. 44, pp. 5199, **2005.**

137 H. A. Tariq, I. A. Khan, U. Ikhlaq and A. Hussnain. "Variation of ion energy flux with increasing working gas pressures using Faraday cup in plasma focus device." *Journal of Natural Sciences and Mathematics*, vol. 48, no. 1, pp. 65-72, **2008.**

138 M. J. Rhee. "Heavy-ion beams produced by high-voltage pulse-powered plasma focus." *Applied Physics Letters,* vol. 37, no. 10, pp. 906-8, **1980.**

139 S. Lee and S. H. Saw. "Plasma focus ion beam fluence and flux—Scaling with stored energy." *Physics of Plasmas,* vol. 19, no. 11, pp. 112703, **2012.**

140 S. Lee and S. H. Saw. "Plasma focus ion beam fluence and flux—For various gases." *Physics of Plasmas,* vol. 20, no. 6, pp. 062702, **2013.**

141 S. Javadi, M. Ghoranneviss, R. S. Rawat and A. S. Elahi. "Topographical, structural and hardness changes in surface layer of stainless steel-AISI 304 irradiated by fusion-relevant high energy deuterium ions and neutrons in a low energy plasma focus device." *Surface and Coatings Technology*, vol. 313, pp. 73-81, **2017.**

142 S. Javadi, B. Ouyang, Z. Zhang, M. Ghoranneviss, A. S. Elahi and R. S. Rawat. "Effects of fusion relevant transient energetic radiation, plasma and thermal load on PLANSEE double forged tungsten samples in a low-energy plasma focus device." *Applied Surface Science,* vol. 443, pp. 311-320, **2018.**

143 W. M. Shu, E. Wakai and T. Yamanishi. "Blister bursting and deuterium bursting release from tungsten exposed to high fluences of high flux and low energy deuterium plasma." *Nuclear Fusion*, vol. 47, no. 3, pp. 201, **2007.**

144 F. W. Meyer, H. Hijazi, M. E. Bannister, P. S. Krstic, J. Dadras, H. M Meyer III and C. M. Parish. "He-ion and self-atom induced damage and surface-morphology changes of a hot W target." *Physica Scripta,* vol. 2014, no. T159, pp. 014029, **2014.**

145 C. S. Becquart and C. Domain. "Migration energy of He in W revisited by ab initio calculations." *Physical review letters*, vol. 97, no. 19, pp. 196402, **2006.**

146 K. O. Henriksson, K. Nordlund and J. Keinonen . "Molecular dynamics simulations of helium cluster formation in tungsten." *Nuclear Instruments and Methods in Physics Research Section B: Beam Interactions with Materials and Atoms*, vol. 244, no. 2, pp. 377-91, **2006.**

147 B. B. Cipiti and G. L. Kulcinski. "Helium and deuterium implantation in tungsten at elevated temperatures." *Journal of nuclear materials,* vol. 347, no. 3, pp. 298-306, 2**005.**

148 S. Gonderman, J. K. Tripathi, T. J. Novakowski, T. Sizyuk and A. Hassanein. "Effect of dual ion beam irradiation (helium and deuterium) on tungsten–tantalum alloys under fusion relevant conditions." *Nuclear Materials and Energy*, vol. 12, pp. 346-352, **2017.**

149 Z. Y. Pan, R. S. Rawat, J. J. Lin, T. Zhang, P. Lee, T. L. Tan and S. V. Springham. "Nanostructuring of FePt thin films by plasma focus device: pulsed ion irradiation dependent phase transition and magnetic properties." *Applied Physics A,* vol. 96 no. 4, pp. 1027-1033, **2009.**

150 R. S. Rawat. "High energy density pulsed plasmas in plasma focus: novel plasma processing tool for nanophase hard magnetic material synthesis." *Nanoscience and Nanotechnology Letters,* vol. 4, no. 3, pp. 251-274, **2012.**

151 V. Damideh, O. H. Chin, S. H. Saw, P. C. Lee, R. S. Rawat and S. Lee. "Characteristics of Fast ion beam in Neon and Argon filled plasma focus correlated with Lee Model Code." *Vacuum*, vol. 169, pp. 108916, **2019.**

152 Z. Y. Pan, R. S. Rawat, J. J. Lin, T. Zhang, P. Lee, T. L. Tan and S. V. Springham. "Nanostructuring of FePt thin films by plasma focus device: pulsed ion irradiation dependent phase transition and magnetic properties." *Applied Physics A.* vol. 96 no. 4, pp. 1027-1033, **2009.**

153 S. Lee, T. Y. Tou, S. P. Moo, M. A. Eissa, A.V. Gholap, K. H. Kwek, S. Mulyodrono, A. J. Smith, Suryadi, W. Usada and M. Zakaullah. "A simple facility for the teaching of plasma dynamics and plasma nuclear fusion." *American Journal of Physics,* vol. 56, no. 1, pp. 62-8, **1988.**

154 H. Hallberg, Y. Zhu. “Stability of grain boundary texture during isothermal grain growth in UO2 considering anisotropic grain boundary properties.” *Journal of Nuclear Materials,* vol. 465, pp. 664-73, **2015.**

155 T. K. Seng. “High growth rate synthesis of Zinc Oxide and Carbon based nanostructured materials using dense plasma focus device.” Doctoral dissertation, *National Institute of Education- Nanyang Technical University, Singapore*, **2017.**

156 Z. Shahbazi rad, M. Shahriari and F. A. Davani. “Investigation of Spatial Distribution of Hydrogen and Argon Ions and Effects of them on Aluminum Samples in a 2.5 kJ Mater Type Plasma Focus Device.” *Journal of Fusion Energy*, vol. 30, no. 5. pp. 358-66, **2011.**

157 C. S. Becquart and C. Domain. “Migration energy of He in W revisited by ab initio calculations.” *Physical review letters*, vol. 97, no. 19, pp. 196402, **2006.**

158 X. Ou, W. Anwand, R. Kögler, H. B. Zhou and A. Richter. “The role of helium implantation induced vacancy defect on hardening of tungsten.” *Journal of Applied Physics*, vol. 115, no. 12, pp. 123521, **2014.**

159 M. Cui, T. Shen, L. Pang, Y. Zhu, P. Jin, C. Liu, X. Fang and Z. Wang. “He ion implantation induced He bubbles and hardness in tungsten.” *Nuclear Materials and Energy,* vol. 15, pp. 232-236, **2018.**

160 F. Kong, M. Qu, S. Yan, A. Zhang, S. Peng, J. Xue and Y. Wang. “Helium-induced hardening effect in polycrystalline tungsten.” *Nuclear Instruments and Methods in Physics Research Section B: Beam Interactions with Materials and Atoms*, vol. 406, pp. 643-647, **2017.**

161 I. V. Mazul, M. Akiba and I. Arkhipov. “Status of R and D of the plasma facing components for the ITER divertor.” **2001**.(No. IAEA-CSP8/C)